A Review and Stochastic Simulations of the Nonlinear Properties of Ocean Waves: Applications for Remote Sensing

by

Azed Jean-Pierre

A dissertation submitted to the Graduate Faculty in
Engineering in partial fulfillment of the requirements
for the degree of Doctor of Philosophy

The City University of New York

2003

UMI Number: 3074657

ProQuest Information and Learning Company
300 North Zeeb Road
P.O. Box 1346
Ann Arbor, MI 48106-1346

This manuscript has been read and accepted for the Graduate Faculty in Engineering in satisfaction of the dissertation requirement for the degree of Doctor of Philosophy.

12/10/02 (S. AHMED)

Date Chair of examining committee

12/10/2002 Mumtaz K. Kassir

Date Executive Officer

Dr. Willard J. Pierson,

Dr. Fred Moshary

Dr. Barry Gross

Dr. Robert Carter

Supervisory Committee

THE CITY UNIVERSITY OF NEW YORK

Abstract

A Review and Stochastic Simulations of the Nonlinear Properties of Ocean Waves: Applications for Remote Sensing

by

Azed Jean-Pierre

Advisors: Professors Willard J. Pierson and Samir Ahmed

A method for simulating nonlinear ocean surface wave records and their effects on microwave scattering at low grazing angle is described. The nonlinear simulation is based on the work by M.A. *Srokosz (1998)* who showed that the family of Probability Density Functions (PDF) developed by Karl Pearson fits reasonably well with experimental data. First, the *Pierson-Moskowitz (1964)* frequency spectrum for a given wind speed is used to simulate a linear time record. The result is a function of time with equally spaced points that are normally distributed that conserves the estimated standard deviation. It is then transformed to a nonlinear record for a given value of skewness using the Pearson distribution. The result is a simulated wave record that reproduces the chosen value for the skewness and the standard deviation within the sampling variability. Statistical comparisons are made between simulated nonlinear wave records and actual wave records. The need for a nonlinear model of ocean surface wave for remote sensing is shown. Deficiencies in the Longuet-Higgins distribution, used in radar altimetry, to represent ocean surface waves are shown. An analogous procedure in conjunction with a wavenumber spectrum is used to simulate a surface wave profile as a function of distance along a line. Just as the specular(reflection) direction is defined for a plane surface, the distribution of a rough surface can be used to define the probability of the specular deviation angle. Thus, two dimensional probability (wave elevation and slope) is studied both numerically and analytically and its application to radar detection of low flying object is discussed.

Acknowledgements

I would like to acknowledge God for His love and for allow me the strength through the learning processes of life; the support of my wife Cynthia Jean-Pierre for understanding and keeping me strong when the road seemed so dark; Dr. Willard Pierson and Dr. Winfield Sylvester of the Remote Sensing Laboratory, CCNY, for their many years of educational, financial and emotional support; Dr. Samir Ahmed of the Electrical Engineering dept., CCNY, for keeping his doors open while I learn the intricate procedures for completing this dissertation; Dr. Gordon Groves of the Naval Surface Warfare Center for making me realize my real potential as an Engineer; The Center for Analysis of Structures and Interfaces (CASI) for the many years of financial support through NSF scholarships; Mr. Al Lewando and Dr. Mike Wild of the Naval Oceanographic Office(NAVOCEANO) for allowing me the time to complete this dissertation; Dr. Robert Carter of NAVOCEANO for his many useful insights; and finally, Dr. Anne Karin Magnusson of the Norwegian Meteorological Institute and professors Mark Donelan and George Ross for helping to get the Ekofisk and Draupner data. Many thanks are due to my friends and family who have supported and encouraged me through the good and bad times.

Table of Contents

List of Tables

List of Illustrations

Chapter 1

1.0 Introduction

Oversimplified descriptions of water waves used in physics books to illustrate wave motions are misleading. Waves on the actual ocean are an extraordinarily complex phenomena. The apparent wave lengths, wave periods, and wave speeds defined in analogy to water waves are obviously wrong. Water waves in nature are not periodic. If the wave period was known, its height at distances away from the observation points could be predicted "exactly". What can be said is that the waves have a predominant (most probable) "wave period", "wave length" and "wave speed" dependent on the prevailing wind speed and fetch. The state of the sea would be partially described by a Probability Distribution Function (PDF). The predominant values would have the highest probability. Ocean waves as a function of x, y and t as in $\eta(x,y,t)$ have never been completely described mathematically. The problem is in solving the hydrodynamic equation with nonlinear and nonstationary boundary conditions. Approximations exist such as a representation by a linear and Gaussian stationary stochastic process. This approximation does not describe the essential nonlinear properties of the waves such as the skewness. The skewness property is revealed in the sharper crests and flatter troughs of actual nonlinear ocean waves.

The need for models of nonlinear waves has been documented for naval architecture by *Hutchison (1990)* and for many design problems by *Borgman (1990)*. Remote sensing also depends on a better understanding of the nonlinear properties of the waves. Radar scatterometry (NASA NSCAT and QuickScat missions), radar altimetry (NASA Topex/Poseidon, Jason-1 missions), and marine radar surveillance systems depend on accurate knowledge of ocean surface waves for efficient operation. *Donelan and Pierson (1987)* used a linear model for the wave slope in a two scale model to describe the scattering properties of the waves. *Hayne et al. (1994)* and *Zieger et al. (1991)* describe the operation of radar altimetry (Topex/Poseidon) using a defined PDF of the ocean surface waves. The scattering of Electromagnetic waves causes background noise in algorithms for tracking objects close to the ocean surface, *Broschat (1993), Groves and Chow (1998), Trizna (1991)*. Many references in the *"Special issue on low grazing angle backscatter from rough surfaces" (IEEE 1998)* show the limiting factor of marine radar operation. A better understanding of the nonlinear properties of ocean waves would help to improve reflection and scattering properties and hence improve detection algorithms.

There follows an extension of the work by *Pierson and Jean-Pierre (1999)* and *Jean-Pierre et al. (1999)*. The nonlinear features of ocean waves as measured by wave staffs and lasers are described. Then a method to simulate nonlinear ocean wave records by means of the Monte Carlo method is derived. This procedure is based on the paper by *Srokosz (1998)* who showed that the family of probability density functions derived by *Pearson (1895)* had properties that were very similar to the distribution of equally spaced values in an ocean wave record. This method is not a perturbation expansion nor can it tell whether an individual wave will break. It uses the superposition of linear solutions to the hydrodynamic equation and the nonlinear effects are introduced by using the Pearson distribution. To better understand the sampling variability of the method, one thousand 30-minute records are simulated and the statistical results are described. Some quotes and figures are taken from ***Pierson and Jean-Pierre (1999)*** and ***Jean-Pierre et al. (1999)*** in order to show continuity of previous work.

A change of variable is used in conjunction with the wave number spectrum to convert the time series into a surface wave profile as a function of distance along a line. So as to be able to define the reflection properties, an effort is made to describe the two-dimensional probability density function of ocean wave height and slope. From these PDFs a method is developed to define the conditional probability of the portion of the waves involved in scattering electromagnetic radiation at various grazing angles. The derived PDFs can be used to improve radar surveillance algorithms. To illustrate potential application of the nonlinear method for radar altimetry, the procedure for measuring ocean surface wave height from an orbiting spacecraft (Topex/Poseidon) is reviewed. An alternate method is suggested to correct for flaws in the present altimeter algorithm.

Chapter 2

2.0 Mathematical Review and Motivation

A brief description of the mathematical equations that govern the analysis of ocean waves is described so as to appreciate the method presented in this dissertation. The wave phenomena are so complex that a lot of assumptions are made before a realistic approximation can be found. The basic modelling tool of Physical Oceanography is the partial differential equation. We know that if only we could find the right set of equations, with the right set of initial and boundary conditions then we could solve the mysteries of ocean dynamics once and for all. To avoid these seemingly overwhelming obstacles, approximations are often made involving simpler equations that neglect, for example micro scale processes, and model our lack of knowledge as a random noise of some kind. In some sense, this last sentence describes what is meant by "Stochastic models" in Physical Oceanography. Thus the basic definition of a stochastic model is a model whose characteristics are defined by an infinite sequence of jointly distributed random variables.

Neumann and Pierson (1966), among many others, described a procedure to solve the wave equations by means of a perturbation expansion. The starting point in the derivation is the equations for incompressible inviscid flow in a cartesian coordinate on a non-rotating earth. These equations can simply be written as

$$\begin{aligned} u_t + uu_x + wu_z &= -\frac{P_x}{\rho} \\ w_t + ww_x + ww_z &= -\frac{P_z}{\rho} - g \\ u_x + w_z &= 0 \end{aligned} \tag{2.1}$$

where x and z are the horizontal and vertical space dimensions, and u and w are the the horizontal and vertical components of the velocity field. The subscripts indicate partial derivatives with respect to the spatial dimensions and time.

Now suppose that the waves are irrotational. This assumption is the same as the assumption that a velocity potential exists. Then it can be assumed that the fluid velocities are given by

$$u = -\phi_x \qquad \text{and} \qquad w = -\phi_z \tag{2.2}$$

The hydrodynamic equations for irrotational invisid flow in a Cartesian coordinate system can be transformed to the potential function (2.3), the Bernoulli equation (2.4) and the kinematic boundary condition (2.5) with the further restriction that there is no input from the wind. The requirement that a fluid parcel on the free surface remains on the free surface is the kinematic boundary condition.

$$\phi_{xx} + \phi_{zz} = 0 \tag{2.3}$$

$$gz - \phi_t + \frac{1}{2}(\phi_x^2 + \phi_z^2) + \frac{p}{\rho} = constant \tag{2.4}$$

$$\phi_z + \eta_t = \phi_x \eta_x \tag{2.5}$$

The Bernoulli equation and the kinematic boundary condition are both nonlinear. They are cross-coupled because a solution would require that both the potential function, $\phi(x,y,t)$, and the free surface, $\eta(x,y,t)$, be found. The solution would be defined for $\eta(x, y, t)$ over the entire x, y plane, and the potential function for deep water would be defined over depth from the surface to minus infinity.

The above requirements are already quite complicated, but the next one is the most difficult. The Bernoulli equation and the kinematic boundary condition are to be satisfied on the free surface given by $\eta(x, y, t)$ which is not known a priori. Part of the problem is to find the location of the free surface. These equations define a free boundary problem for a wavy ocean surface that is assumed to be present and that will last forever. In this form, there do not appear to be any solutions available that would completely represent actual waves in a storm sea.

The linear solution to this system of equations is found by dropping the nonlinear terms and satisfying the free surface boundary condition at z = 0.

$$\eta(x, t) = a \ \cos\ (kx - wt) \tag{2.6}$$

$$\phi = -aC_D e^{kz} \ \sin(kx - wt) \tag{2.7}$$

$$w^2 = gk \tag{2.8}$$

Equation (2.6) and (2.7) are the solutions for the free surface and potential function, respectively. Equation (2.8) is the linear dispersion relationship.

The difficulties for the nonlinear description of waves can be illustrated in a simple way, as described in *Pierson (1993)*, by considering the third order solution for a Stokes wave as in

$$\eta(x, t) = a\cos(\theta) + (\frac{a^2k}{2})\cos(2\theta) + (\frac{3a^3k^2}{8})\cos(3\theta) \tag{2.10}$$

$$\phi(x, z, t) = [-aC_D + \frac{a^3k^2}{8}C_D] \ e^{(kz)}\sin(\theta) \tag{2.11}$$

where $\theta = k(x - Ct)$. The derivatives for the potential function (2.11) yield the fluid motions, and the value of C could be approximated by equation (2.13) to the same order

$$C^2 = (\frac{g}{k})(1 + a^2k^2) \qquad (2.12)$$

$$C = (\frac{g}{k})^{1/2}[1 + \frac{a^2k^2}{2}] \qquad (2.13)$$

For the same wavenumber, if a is doubled, the amplitude of the second order term is four times larger and the amplitude of the third order term is eight times larger. Moreover, in this form the phase speed increases so that the frequency of the wave is higher, and the period is shorter.

Drennan (1988) and *Drennan, et al. (1992)* have used a reformulated boundary value problem and obtained solutions to very high order for a Stokes wave. *Drennan (1988)* showed that the phase speed of the highest possible Stokes wave was about 5 percent greater than for a linear model. For the same wave period, the wave would have to be about 5 percent longer. Something similar would also happen for actual waves. *Pierson (1993, 1994)* has investigated the subject of finding third order solution for sums of long crested Stokes waves, and *Pierson, et al. (1998)* have done laboratory experiments to try to discover something about the interactions of sums of sinusoidal waves when they are used to drive a wave generator. Even if a solution to these equations could be found, it would fail to represent an actual seaway because of breaking waves.

The method that will be presented in Chapter 3 avoids all the complications involved in solving the hydrodynamic equations. It simply uses a known variance spectrum, which is limited in defining the nonlinear properties of the waves, and the linear solution, equation (2.6), to the hydrodynamic equations. The nonlinear properties, as observed in laboratory and field measurements, are then introduced using the Pearson distribution.

2.1 Wave Spectral Estimation

Wave data are presently analyzed as if they were a sample from a stationary stochastic process. The spectral estimates are usually assumed to be representative of a large area around the particular point where the waves were measured. It is consequently necessary to consider the sampling variability of the spectral estimates. The spectral estimates that are obtained resolve the variance of the wave record into frequency bands. The spectrum does not provide a complete description of the waves because it tells nothing about the nonlinear properties of the original record. The Monte Carlo simulations in this dissertation will show this result in section 3.3.

There may be a dilemma about the interpretation of these variance spectra. There are some methods for obtaining wave data such as measurements by moored buoys that do not respond to the nonlinear wave properties as shown by *Anctil, et al. (1993)* and as explained by *James (1986)*. However, Wave staffs and lasers do record the nonlinear wave properties, but the spectral estimates of the variance cannot separate nonlinear effects from what might be considered to be the linear effects. For typical record lengths there is always a trade-off between spectral resolution and the confidence intervals for the estimate as first shown by *Tukey (1950)*. *Neumann and Pierson (1966)* treat this subject in terms of the methods for spectral estimation that were used at that time. *Donelan and Pierson (1983)* show a more modern method in terms of the discrete Fourier Transforms of sample wave records from a laboratory wind wave flume that were known to be invariant as to the wave conditions. The squares of the amplitudes divided by two of the Fourier spectra that were obtained were shown to have a chi-square distribution with two degrees of freedom and were highly variable at the same frequency from one record to the next.

Chapter 3

3.0 Monte Carlo Simulation in Time Domain

3.1 Linear Wave Simulation

The Monte Carlo technique is used to simulate an ocean wave record using the Pierson-Moskowitz(PM) wave spectrum. The Monte Carlo method is a "technique for obtaining an approximate solution to certain mathematical and physical problems, characteristically involving the replacement of a probability distribution by sample values and usually done on a computer" (*Webster's New World Dictionary, 1972*).

Moskowitz (1964) analysed a series of ocean wave data as measured in the field. The results were used by *Pierson and Moskowitz (1964)* to propose the form of the ocean spectra for a fully developed sea. This is one of many available frequency representations of the waves. Any one of them, for example the JONSWAP spectra, could have been used. The PM spectra are represented by

$$S(w) = (\alpha g^2/w^5)\ e^{-\beta(w_0/w)^4} \tag{3.1}$$

where $\alpha = 8.1 * 10^{-3}$, $\beta = 0.74$, $g = 9.81 m/s^2$ and $w_0 = g/U$ where the wind speed, U, in m/s is measured at 19.5 m above the sea surface. A wind speed of 15 m/s measured at 19.5 meters above the mean sea surface was chosen so that the significant wave height(SWH) for a linear model would be 4.77 meters. The SWH is the average of the crest to trough "height" of the one-third highest waves in the wave record. A graph of this spectrum for a wind speed of 15 m/s is shown in figure 3.1.

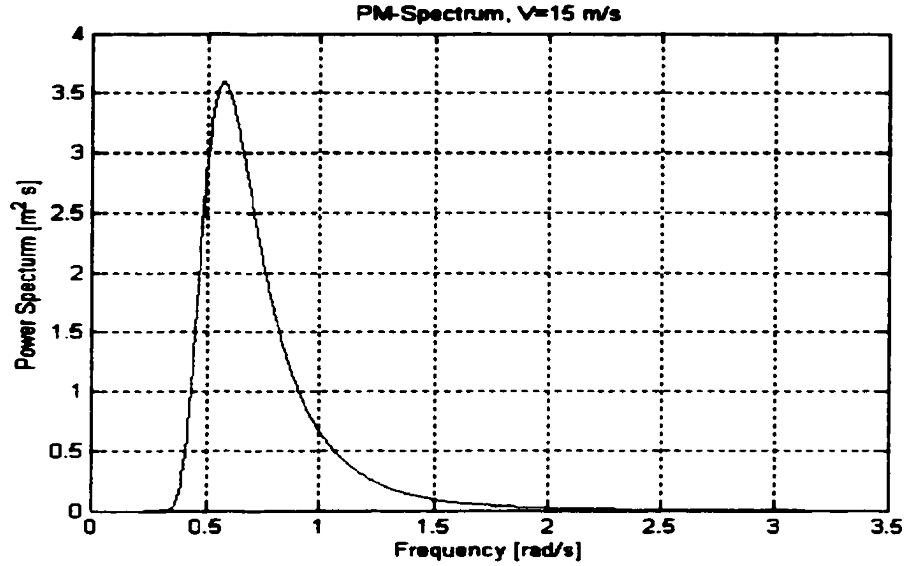

Figure 3.1 The Pierson-Moskowitz spectrum for a wind speed of 15 m/s

For a significant wave height ($H_{1/3}$) of 4.77 m, the corresponding standard deviation σ_η would be 1.193 m. This is from the well known definition $H_{1/3} = 4\sigma_\eta$, where σ_η is the standard deviation measured from a wave time history. *Forristall (1978)* discussed that $H_{1/3}$ could be defined from a direct counting of the wave heights as the average of one-third of the largest waves. It is expected that any wave time history simulated using the spectrum of figure 3.1 would have a standard deviation of 1.193 m. Consequently, the Fourier Transform(FT) of the simulated wave record is also expected to have a peak value of 3.6 $m^2 s$ at 0.56 rad./s.

Figure 3.2 shows characteristic properties of the Pierson-Moskowitz (PM) Spectrum for wind speeds of 10, 12, 15 and 17 m/s. Note that for higher wind speeds, the amplitude of the spectrum increases and the peak amplitude shifts towards lower frequencies.

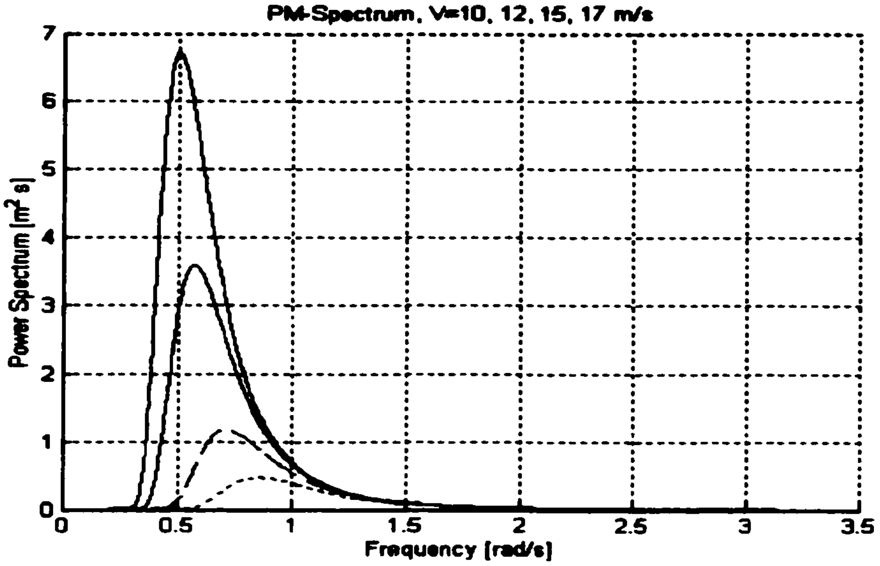

Figure 3.2 The Pierson-Moskowitz spectra for wind speeds of 10, 12, 15, and 17 m/s

The wave records that were used by *Moskowitz (1964)* were obtained by the Shipborne Wave Recorder described by *Tucker (1956)*. Accelerometers mounted near the bow of a weather ship were doubly integrated and pressure measurements from sensors on the side of the ship's hull were used to add a correction to the resulting record to produce a graph of the waves passing the ship. In retrospect, whether these records yielded a nonlinear wave form similar to a wave staff or laser or, more likely, one that more nearly corresponded to a data buoy measurement is open to question.

Teng, et al. (1994) used extreme value theory to calculate the 100 year return significant wave heights at 10 of the deep ocean National Data Buoys. They also found that equation (3.1) seemed to fit the data quite well at many of the buoy locations. See also the comments by *Pierson (1994)* in that paper.

For any given point, for example $x = 0$, equation (2.6) becomes a function that varies only in time. Simulation of the wave time history can then be performed at a single point. The discrete form of equation (2.6) is shown in equation (3.2). The spectrum of equation (3.1) is quantized so as to obtain the coefficients a_p as in equation (3.3). The Monte Carlo simulations were done for 30 minute records as if the

data were recorded every second for 1800 points, but the time history was evaluated at 0.1 second intervals. The frequencies in this sum varied from $\pi/1800$ to π so that the shortest period in the simulated linear record was 2 seconds. In other words, the highest frequency in the simulated record would be 0.5 Hz. Therefore, sampling every 0.1 second, or 10 Hz, is well above the nyquist rate. Aliasing will not be a factor in this representation.

$$\eta(q\Delta t) = \sum_{p} a_p \cos\left(w_p t + \epsilon_p\right) = \sum_{p=0}^{900} a_p \cos\left[\left(\frac{2\pi p}{1800}\right)\left(\frac{q}{10}\right) + \epsilon_p\right] \tag{3.2}$$

The ϵ_p are a set of 900 phases values chosen at random between 0 and 2π. This function is periodic and repeats exactly every 30 minutes. The values of $a_p^2/2$ are given by equation (3.3)

$$a_p^2/2 = S(w_p)\Delta w = S\left(\frac{2\pi p}{1800}\right) * \left(\frac{2\pi}{1800}\right) \tag{3.3}$$

From equation (3.2), as p varies from 1 to 900, 900 coefficients (a_p) are needed to compute the values for the wave record. This essentially quantize the PM-spectrum into 900 frequency components. Thus

$$a_p = \left[2S\left(\frac{2\pi p}{1800}\right) * \left(\frac{2\pi}{1800}\right)\right]^{1/2} \tag{3.4}$$

Figure 3.3 shows a plot of equation (3.2) for a wind speed of 15 m/s. Figure 3.4 is a subset of figure 3.3 that shows the variations of the wave time history in more detail. A histogram of figure 3.3 will indeed result in normally distributed values. Another way to look at this plot is to note that turning it upside down would result in a similar plot. That is, the distribution of the wave heights above the mean equals the wave troughs below the mean level. All of the records that could be calculated using equation (3.2) for different sets of the random phases would have the same variance, essentially zero skewness and a kurtosis nearly equal to three. They will be useful in the next step so as to be able to understand subsequent results. These parameters are the properties of a Gaussian distribution (ie. 0 skewness and kurtosis of 3).

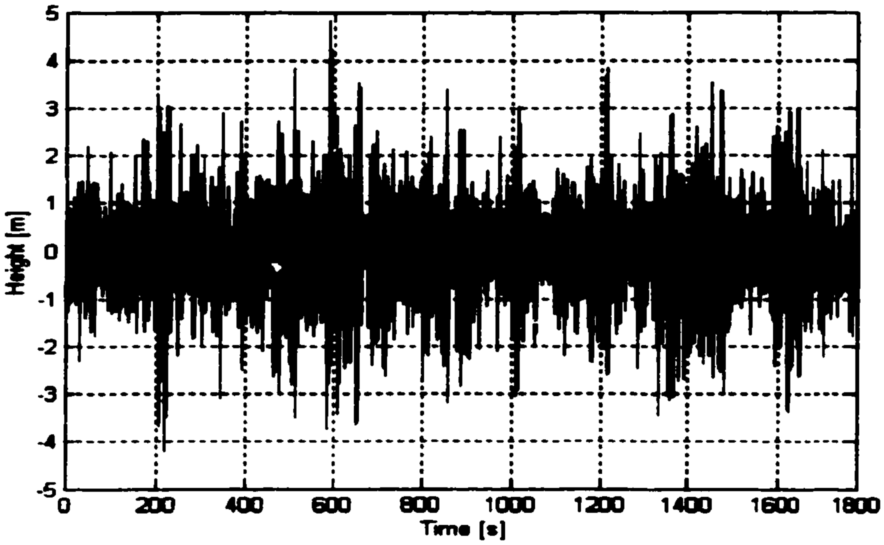

Figure 3.3 Linear Monte Carlo simulation of ocean surface waves using the PM spectrum of figure 3.1.

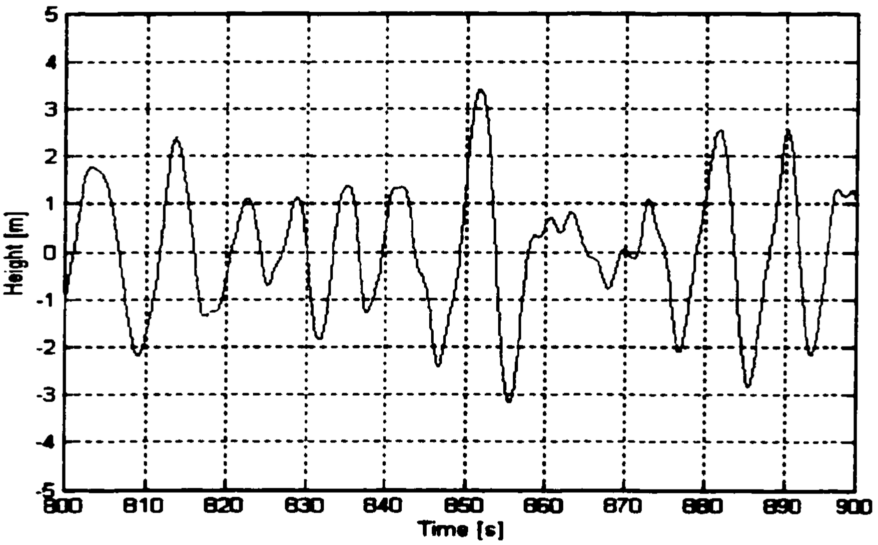

Figure 3.4 Portion of figure 3.3.

Figure 3.5 shows the scatter diagram of such statistics for 1000 independent Monte Carlo simulations of equation (3.2). The scatter plot shows a mean of zero with variations of $\pm 10^{-15}$ m, a standard deviation (σ_η) of 1.197 m, a skewness of zero with

variations of ±0.1, and a kurtosis of 3 with variations of ±0.5. These variations are within acceptable limits as the higher order statistics require more data to be more accurate.

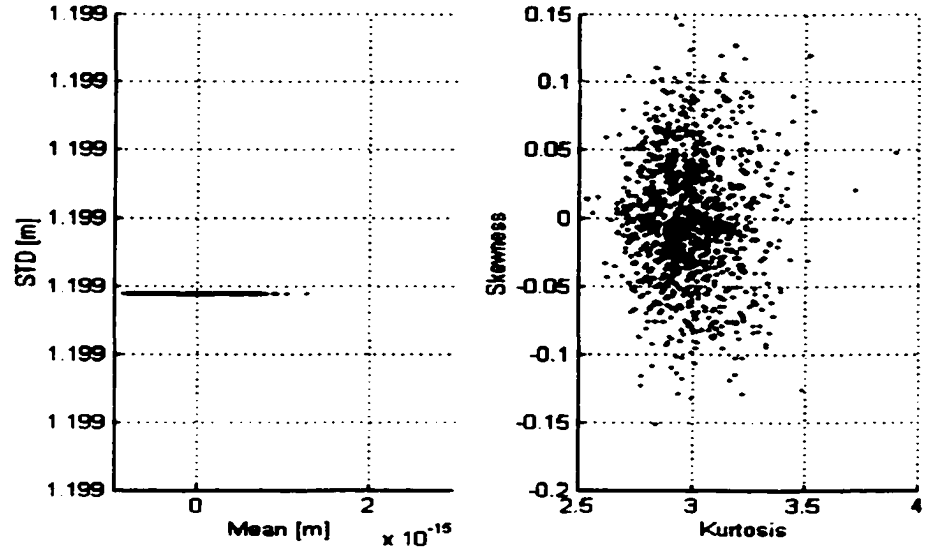

Figure 3.5 Scatter diagram of the statistics for 1000 independent Monte Carlo simulations for a wind speed v=15 m/s.

An essential element of a random seaway can be modeled by using the result of *Donelan and Pierson (1983)*. Donelan and Pierson showed that the values of the $a_p^2/2$ have a Chi-Square distribution with a parameter and with two degree of freedom which is given by equation (3.5).

$$y = P_{\chi^2}(R) = e^{-R} \tag{3.5}$$

As y varies from zero to one, R varies from infinity to zero. If a value of y is picked at random from a uniform distribution over zero to one, the value of R is

$$R = -ln(y) \tag{3.6}$$

The values for the amplitudes in equation (3.3) then become equation (3.7).

$$a_p = \left[2R\, S\left(\frac{2\pi p}{1800}\right)\left(\frac{2\pi}{1800}\right)\right]^{1/2} \tag{3.7}$$

There are other ways to do this. For example, if equations (3.2) and (3.3) had been calculated for ten times as many frequencies between zero and π, the result would be indistinguishable from this second result if the data were obtained at one second intervals.

If equation (3.7) is substituted into (3.2) and evaluated for different randomly chosen phases and amplitudes, the spectra of the simulated time series will vary in the same way as those described by *Donelan and Pierson (1983).* Moreover in this set of realizations there will be sample spectra that have the properties of the JONSWAP spectra as described by *Donelan and Pierson (1983)* and discussed by *Pierson (1977).*

Tucker, et al. (1984) randomized the amplitudes of the sine and cosine terms in a simulation of a wave record for a Pierson-Moskowitz spectrum. Spectra obtained in this way from the simulated data showed the same variations as those shown by *Donelan and Pierson (1983)* for actual data. This method is equivalent to the use of equation (3.2) when the random amplitudes of equation (3.7) is applied. The statistics for this modified simulation, as shown in figure 3.6, is slightly different than that of figure 3.5 in the computed standard deviations. Randomizing the amplitude results in the standard deviation varying within ±0.1 m of the original 1.197 m. The simulated waves also show some occasional higher wave crests. There were no significant differences in the distribution of the mean, skewness and kurtosis values. The difference in the spectrum obtained in this way is shown in figure 3.29. The details are deferred until the nonlinear transformation is applied. The frequency representation is discussed in details in section 3.3.

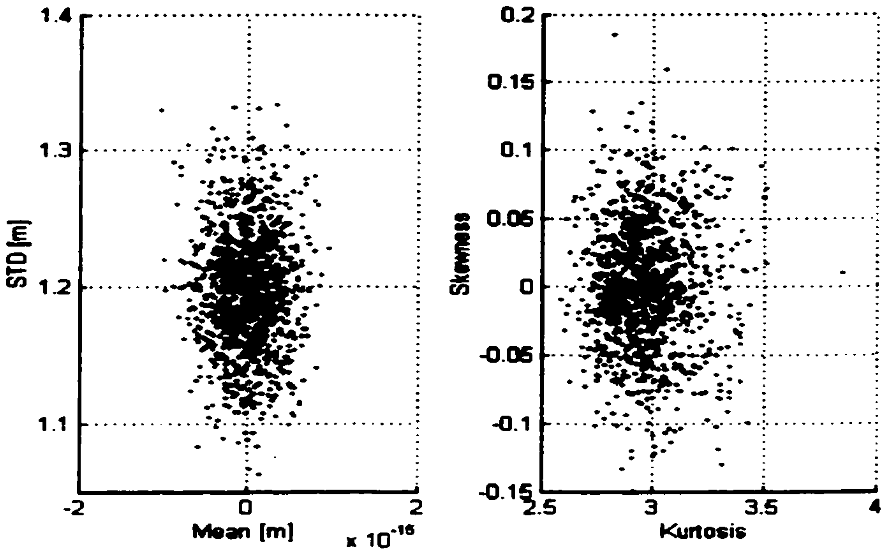

Figure 3.6 Scatter diagram of the statistics for 1000 independent Monte Carlo simulations using random amplitude and phase for a wind speed v=15 m/s.

3.1.1 Discussion of Linear Models

The Chapter on Waves and Tides in *The Oceans* by *Sverdrup, et al. (1942)* described the early results of the wave forecasting method developed by H. U. Sverdrup and W. H. Munk. The use of this method is described by *Bates (1949)*. *Sverdrup (1943)* repeated much of the material in *The Oceans* and gave the linear equations for the phase speed, wavelength and period of a sinusoidal wave. He cautioned that "These formulas apply only to a wave whose amplitude is small relative to its length and therefore cannot be expected to be valid to all cases." The concept of waves as a Stochastic process was not known when these two books were published.

Ogilvie (1964) wrote that "From these stochastic models, one can derive all kinds of interesting conclusions about the sea, some of which will be true". *Dalzell (1974)* wrote that "Of the two St Denis/Pierson hypotheses, *St Denis and Pierson (1953)*, that of the stationary, Gaussian seaway was considered to be the Oceanographer's province and was mostly taken for granted - at least by the ship research field. The other hypothesis, linearity, was considered to be the heart of the matter".

The linear and Gaussian stochastic model (i.e. an infinite sequence of jointly distributed random variables) for ocean surface waves has been described in many references such as *Longuet-Higgins (1952)* and *Kinsman (1965)*. These linear models for the waves are, of course, the subject of the above quotations. This model has proven to be a useful description of the waves on the ocean. The literature, with special reference to the many papers by M. S. Longuet-Higgins, contains many references on the probabilistic properties of a linear model and of the statistical analysis of recorded wave data. Examples are the PDF of the crest to trough wave heights, the joint PDF of the apparent wave "periods" and crest to trough wave heights, and the PDF for the highest waves in a sequence of N waves. The significant wave height($H_{1/3}$), with the further restriction of a narrow band spectrum, is obtained from the probability density function of the crest to trough wave heights. Comparisons of the actual crest to trough wave heights from a wave record with the value computed from four times the standard deviation of the wave record usually show fairly good agreement ($H_{1/3} = 4\sigma$). This equation is used in application to satellite remote sensing of the ocean surface topography. σ is one of the essential parameters used in (Topex/Poseidon) Altimeter measurements to derive the wave height. The significance of σ is further discussed in Chapter 6.

The difficulty lies in the use of the crest to trough wave height because the height of a high wave crest above the mean is not equal to the depth of the wave trough below the mean. An actual wave staff record has Stokes-like wave forms when the waves are high that cannot be represented by a linear model.

Of course, Sverdrup was correct. The linear approximation "cannot be expected to be correct in all cases".

The quotation from Ogilvie needs to be modified as follows: "From these linear stochastic models, one can derive all kinds of interesting conclusions about the sea, some of which will be approximately true".

For the quotation from Dalzell, as stated by *Hutchison (1990)*, the nonlinear motions of a ship in nonlinear waves have yet to be completely described by a mathematical model.

In the paper "Ship stability in heavy weather: The real situation and models thereof" in which Pierson describe a court case of a storm on February 23-27, 1987, Pierson wrote: "The conditions encountered by a ship may possibly be predictable only in a probability sense for design purposes in terms of stochastic processes. A realistic theory to describe nonlinear random waves as a stochastic process does not presently exist. ... Real waves are dangerous and destructive. ... One of the needs for the development of a mathematical model of ship capsizing in extreme waves is the need for an adequate model of extreme waves. Extreme waves are nonlinear and random so that a stochastic model of nonlinear extreme waves is needed as a part of the eventual solution to this problem." Pierson further stated: " It will never be possible to describe ship motions in high seas by means of a linear model."

3.2 Nonlinear Transformation

In the next sections to follow, many years of study and research of ocean waves is used to obtain a better approximate representation of the waves. The derived method does not try to reinvent the wheels. It uses a well known method of simulating a "gaussian" ocean wave time history as in equation (2.6). Then a PDF that proves to have similar properties to ocean surface waves is used to introduce the nonlinear characteristics to the already available solution. The main advantage of this method is that the hydrodynamic equations do not have to be solved.

3.2.1 Wave Measurements

Properties of ocean waves as measured in the field are studied so as to compare with analysis of the simulated records. Data on waves have been obtained primarily in two different ways. One way is to record the waves as they pass either a wave staff mounted on a platform or a wave wire held in place by a support. The other is to record the heave acceleration, and perhaps the pitch and roll, of a moored buoy. The time histories that result from wave staff and wave wire measurements can then be used to estimate the wave spectrum. The buoy data such as data obtained by the

National Data Buoy Center *(Steele, et al. 1992)* are processed in such a way as to obtain estimates of the wave spectra, but usually there is no record of the waves as a function of time.

Statistics from the wave record can be obtained by computing the mean (put equal to zero) variance, m_2 (and hence the standard deviation), the third moment, m_3, and the fourth moment, m_4. These can be put into normalized form by computing the skewness, $\mu_3 = m_3/m_2^{3/2}$ and the kurtosis, $\mu_4 = m_4/m_2^2$. If the waves were close to being represented by a linear model, μ_3 should be nearly zero and μ_4 should be about equal to 3. This is consistent with analysis of data obtained from the simulation of equation (3.2).

"*Srokosz (1998)* showed that the family of probability density functions obtained by *Pearson (1895)* had properties that agreed very well with wave wire data obtained in a reservoir. The standard deviations for the data ranged from 2.06 cm to 7.19 cm. For the 15 wave records analyzed by Srokosz, two values of the skewness were less than 0.10, two were between 0.10 and 0.20, five were between 0.20 and 0.30 and the four highest were 0.325, 0.433, 0.453 and 0.504. Nine values for the kurtosis were less than 3.00. The highest value for the kurtosis was 3.306 and the lowest was 2.492. A linear and Gaussian model for these waves would need to be rejected" *Pierson and Jean-Pierre (1999))*. These skewness values contradict the assumed 0.1 skewness used in analysing Topex/Poseidon altimeter signals. This is further described in Chapter 6.

Buoy time histories were compared to wave staff time histories by *Anctil, et al (1993)*. The nonlinear properties of the wave staff data were clearly shown by the values of the skewness whereas the buoy records had little or no skewness. These data consisted of measurements by a data buoy and a wave staff where the two systems were close-by. Successive pairs of measurements were compared in their Figure 5 (not shown). The significant wave height varied from 1 to 3 meters. The scatter about the 45° line of perfect agreement when buoy and wave staff values were compared was 2 to 3 tenths of a meter. The sample values of the skewness had a range from about -0.03 to perhaps as high as 0.41 with only one negative value for the wave staff data whereas the values for the skewness for the buoy data scattered above and below zero with a range of approximately ±0.1. The plotted values for the kurtosis scattered in a circular region about a point at about 3.1 for the wave staff and 2.9 for the buoy with a radius of 0.3. Most of the values for the wave staff were greater than 3 and most of the values for the buoy were less than 3. The statistics of the buoy data is similar to the linear wave simulation shown in figure 3.5 and figure 3.6.

A well studied data set that also shows the nonlinear properties of waves is the data measured for Hurricane Camille which were obtained on August 17, 1969 at an offshore platform called South Pass 62a. The program for obtaining these data was described by *Ward (1974)*. These data have also been studied by *Earle (1975)*, *Cardone, et al. (1976)*, *Forristall (1978)* and *Buckley (1983)* among others. Table 3.1, and figure 3.7 show some of the properties of these measurements.

The raw data was measured in feet every second (1Hz). Since all other wave time histories are presented in meters, the unit is changed to meters. The wave height measurements ranged from about 0.5 meters to 25.1 meters. The one hour data was broken to 30-minutes records for analysis. Table 3.1 shows the statistics for 31 30-minutes records. It is customary to analyse wave data with zero mean. Thus the mean is computed and the minimum and maximum values are given relative to the mean. The minimum and maximum values for each record corresponds to the deepest trough and highest crest in different parts of the record, respectively. The maximum value of 14.152 m (25.12 - 10.97) occurred in record with starting time 1600 and the minimum value of -10.402 m (0.488-10.89) occurred in record 1530. It is important to note that the wave staff broke after record 1600. The last 4 columns in table 3.1 are the standard deviation (σ), skewness (μ_3), kurtosis (μ_4), and the significant wave height ($H_{1/3}$). $H_{1/3}$ is a measure of the standard deviation and it is given by 4σ.

Table 3.1 Statistics for wave data measured at south pass 62a during Hurricane Camille on August 17, 1969. The time is the start of the 30 minutes record in Central Daylight Time (CDT). The Min and Max values are relative to zero Mean.

Time	Min(m)	Max(m)	Mean(m)	STD(m)	Skew	Kurtosis	$H_{1/3}$ (m)
0100	-2.466	2.443	10.514	0.822	0.055	2.972	3.290
0130	-2.833	2.716	10.546	0.828	0.015	2.871	3.312
0200	-2.910	3.035	10.563	0.814	0.005	3.011	3.256
0230	-2.608	3.002	10.565	0.855	0.100	2.943	3.420
0300	-2.481	3.007	10.560	0.898	0.074	2.826	3.591
0330	-3.161	2.876	10.569	0.934	0.023	2.818	3.735
0400	-2.913	2.727	10.566	0.933	0.078	2.953	3.733
0430	-3.239	3.590	10.587	0.983	-0.029	2.878	3.931
0500	-3.054	4.690	10.584	1.022	0.081	3.145	4.087
0530	-3.782	4.205	10.581	0.987	0.092	3.117	3.950
0600	-3.000	3.555	10.561	1.065	0.152	2.806	4.261
0630	-3.988	4.396	10.573	1.158	0.032	3.146	4.632
0700	-4.356	5.004	10.637	1.188	0.132	3.338	4.752
0730	-4.466	3.643	10.655	1.237	-0.023	2.958	4.950
0800	-5.070	5.357	10.710	1.323	0.054	3.134	5.290
0830	-4.182	3.928	10.706	1.345	0.095	2.751	5.382
0900	-5.095	5.484	10.705	1.546	-0.022	2.833	6.182
0930	-5.949	5.575	10.736	1.642	0.079	3.105	6.566
1000	-5.392	6.681	10.758	1.773	0.099	2.916	7.093
1030	-5.981	5.605	10.798	1.892	0.052	3.013	7.568
1100	-6.380	6.760	10.832	2.118	0.091	3.074	8.472
1130	-7.099	8.053	10.849	2.357	0.001	2.965	9.429
1200	-10.349	11.693	10.837	2.473	0.095	3.729	9.890
1230	-6.806	9.870	10.800	2.510	0.217	3.140	10.040
1300	-9.545	10.394	10.795	2.575	0.025	3.084	10.299
1330	-9.365	9.720	10.798	2.798	0.190	3.262	11.194
1400	-7.598	10.298	10.799	2.680	0.242	2.996	10.718
1430	-7.215	10.620	10.782	2.765	0.282	3.051	11.059
1500	-8.070	12.723	10.783	3.031	0.269	3.077	12.126
1530	-10.402	13.744	10.890	3.289	0.297	3.225	13.156
1600	-10.024	14.152	10.970	3.350	0.159	3.203	13.401

The values in table 3.1 are better viewed in figure 3.7. The mean value range from 10.5 to 11 m. The STD range from 0.7 to 3.5 m. Skewness range from -0.05 to 0.3 and kurtosis range from 2.7 to 3.8. The skewness value is a measure of nonlinearity of the waves. Records 0100 through 1200, have skewness values within ±0.1 and the difference in magnitude between the minimum and the maximum are less than 1 meter. These records have some linear properties. However, Records 1330 through 1600 have skewness values from 0.16 to 0.3. The difference between maxima and minima range from 2.5 to 4 meters. These correspond to properties of nonlinear waves. In general, the records with the higher crests have higher skewness values.

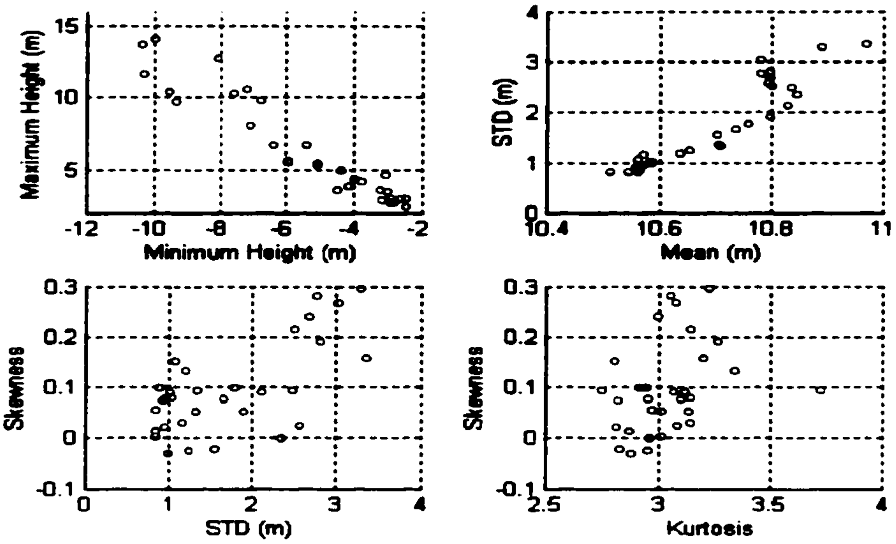

Figure 3.7 Scatter plot for the data collected during Hurricane Camille. August 17, 1969

Figure 3.8 show a section of the 30-minute wave record starting at 1530 CDT. This 1 second sampled record has been fitted with a 0.2 second spline for a smoother display. The top curve shows a wave crest of 14 meters at 226 seconds. The preceding and following troughs are -5 and -7.5 meters, respectively. The troughs are about one third and one half of the crest. The bottom curve show 2 wave crests of 11 and 12 meters. The trough in between is about -6.5 meters. These features are typical of nonlinear wave staff data and determine the skewness and to a lesser degree the kurtosis.

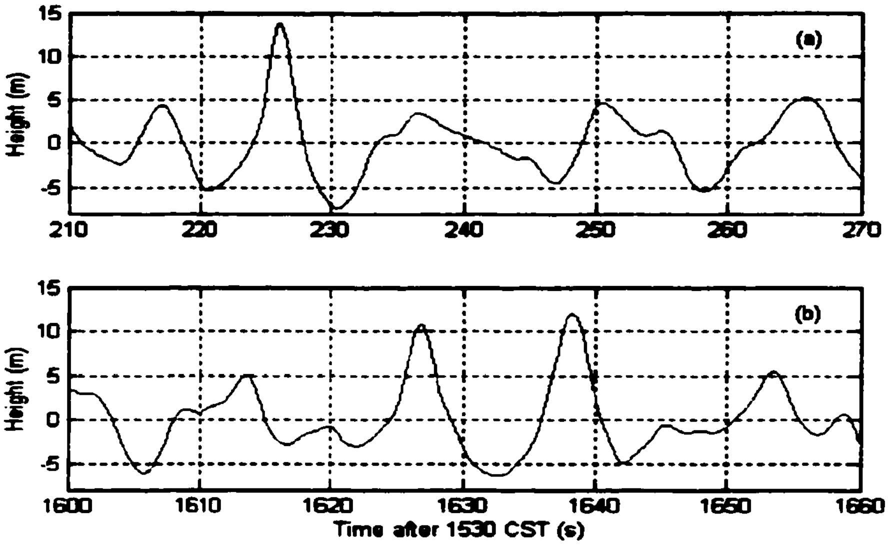

Figure 3.8 Segments of record 1530 data collected during Hurricane Camille. August 17, 1969

The wave spectrum resolves the variance of the record into frequency components. The shape, magnitude and location of the peak spectrum tells information about the standard deviation and therefore the significant wave height ($H_{1/3}$). Figure 3.9 shows the frequency spectrum for records 1330 to 1600. The Standard deviation is a function of the area under the spectrum. Note that the spectrum with the higher peak amplitude corresponds to the larger standard deviation.

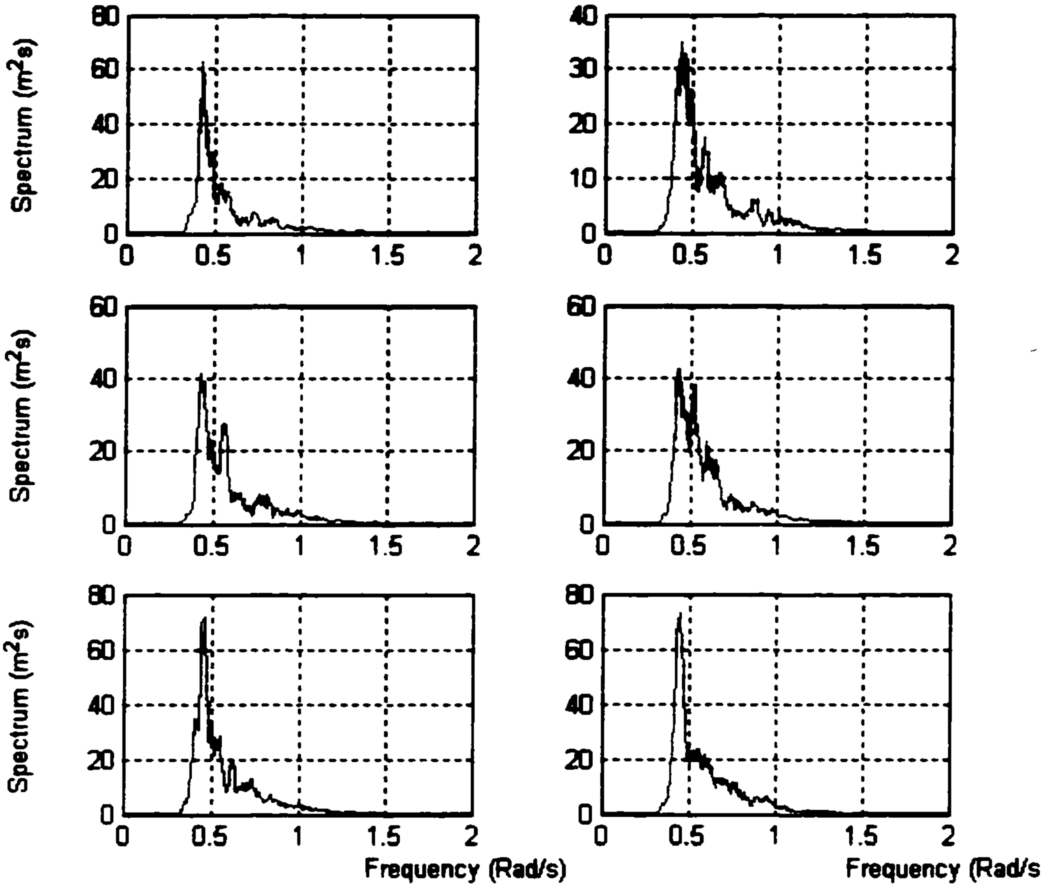

Figure 3.9 The Frequency spectra for records 1330, 1400 (top), 1430, 1500 (middle), and 1530, 1600 (bottom).

Comparisons of Buoy and Laser Data

There follows a description of two collocated data sets that were collected using a data buoy, or waverider buoy and a laser. The laser was mounted on the Ekofisk platform at about 21 meters above the ocean surface. Ekofisk is located in the north sea at latitude 56.5N and longitude 3.2E. The buoy was located approximately 1 km from the platform.

The laser was manufactured by the Canadian company Optec Lasers, and the

90 cm in diameter waverider buoy was manufactured by Datawell. Both instruments sampled the ocean surface wave heights at approximately 2Hz. The equally spaced wave time history were broken into 20-minute records starting at 0000z on October 25, 1998.

Table 3.2 and table 3.3 show the analysis of 68 20-minute records for the buoy and laser data, respectively. Note that records 61, 62 and 63 for time 20:40 are duplicates and times 02:00, 06:00, 21:00, 21:20, 21:40, 23:00 are missing. The reason is unknown at this time. All the measurements are in meters. In both cases the original mean values are shown to reflect instrument offsets. For the laser measurements, the mean value reflects the tide and mean distance above a calm surface. The mean values were subtracted from the data so that the lowest troughs(min) and highest crests(max) are relative to zero mean. In table 3.2, the highest crests for the buoy data are approximately equal to the magnitude of the lowest troughs. Except for five samples, all the skewness values are less that 0.1 in magnitude. These values correspond to statistics that could have been obtained from the linear simulation of the waves. Table 3.3 shows a greater disparity between the lowest troughs and highest crests. Contrary to the buoy data, the laser data has skewness values as high as 0.32. These values reveal the nonlinear properties of the waves and can not be reproduced using the linear simulations of section 3.1. Detailed comparison of the two data sets are shown in figure 3.10 through figure 3.14. In the following figures, the data falling on the straight line corresponds to values that are in perfect agreement between the two instruments. The angle between the straight line and the x-axis (Buoy-axis) should be 45°. All the comparisons are made between data collected for the same time at nearby points.

Table 3.2 Statistics of buoy data measured near the Ekofisk platform in the north sea on October 25, 1998. (*Courtesy Statoil Co.*)

File	Time	Min(m)	Max(m)	Mean(m)	STD(m)	Skew	Kurt
1	0:00	−3.672	3.789	0.228	1.204	−0.024	2.821
2	0:20	−3.457	3.574	0.229	1.076	−0.055	3.101
3	0:40	−2.891	3.359	0.226	0.961	−0.010	2.834
4	1:00	−2.871	3.262	0.230	0.881	−0.075	2.959
5	1:20	−3.008	3.672	0.230	1.033	−0.092	2.965
6	1:40	−2.676	3.184	0.226	0.956	0.003	2.832
7	2:20	−2.715	2.969	0.231	0.931	−0.020	2.661
8	2:40	−2.246	3.008	0.229	0.851	0.089	2.858
9	3:00	−2.773	2.754	0.230	0.800	−0.088	2.996
10	3:20	−2.637	2.793	0.229	0.822	−0.091	3.102
11	3:40	−2.578	2.891	0.230	0.857	0.047	2.978
12	4:00	−2.441	2.734	0.226	0.770	−0.026	2.963
13	4:20	−2.285	2.715	0.232	0.795	−0.042	2.937
14	4:40	−1.992	2.480	0.234	0.738	−0.034	2.782
15	5:00	−2.207	3.242	0.231	0.733	0.049	3.118
16	5:20	−2.168	2.441	0.231	0.724	−0.058	2.848
17	5:40	−1.895	2.480	0.231	0.732	−0.009	2.866
18	6:20	−2.324	2.754	0.232	0.729	−0.076	3.208
19	6:40	−2.422	2.813	0.233	0.769	0.011	3.016
20	7:00	−2.109	2.598	0.229	0.800	−0.064	2.803
21	7:20	−1.914	2.656	0.230	0.813	0.107	2.841
22	7:40	−2.715	3.105	0.232	0.810	−0.048	3.125
23	8:00	−2.754	3.418	0.230	0.843	−0.014	3.207
24	8:20	−2.734	3.340	0.232	0.986	−0.017	2.892
25	8:40	−2.461	3.887	0.230	0.909	0.145	2.872
26	9:00	−2.871	3.164	0.228	0.971	0.017	2.840
27	9:20	−3.477	4.727	0.234	1.163	−0.022	3.033
28	9:40	−3.398	4.473	0.234	1.125	−0.059	3.025
29	10:00	−3.398	3.809	0.234	1.294	0.031	2.689
30	10:20	−3.691	4.121	0.234	1.270	−0.001	2.994
31	10:40	−4.687	4.180	0.219	1.339	−0.117	3.015
32	11:00	−4.297	4.297	0.223	1.326	0.000	3.103
33	11:20	−4.687	4.883	0.224	1.370	−0.027	3.193
34	11:40	−3.965	4.238	0.230	1.357	−0.067	2.863
35	12:00	−5.020	5.410	0.225	1.517	0.058	3.086
36	12:20	−4.199	4.844	0.229	1.433	−0.028	2.826
37	12:40	−5.156	5.879	0.238	1.565	−0.003	3.222
38	13:00	−5.195	6.602	0.237	1.778	0.064	2.964
39	13:20	−5.391	5.313	0.235	1.825	−0.038	2.754
40	13:40	−6.348	5.684	0.241	1.922	−0.080	2.926
41	14:00	−5.977	5.840	0.234	1.961	−0.065	2.802
42	14:20	−6.758	6.230	0.239	1.966	−0.006	2.917
43	14:40	−9.395	8.535	0.253	2.465	−0.002	3.192
44	15:00	−7.520	8.418	0.238	2.144	−0.095	3.150
45	15:20	−7.031	7.090	0.241	2.237	−0.010	3.134
46	15:40	−7.051	6.074	0.244	1.963	−0.149	3.072
47	16:00	−6.973	7.207	0.240	2.344	−0.047	2.805
48	16:20	−7.402	6.719	0.236	2.053	−0.039	3.068
49	16:40	−5.918	6.680	0.238	2.033	−0.091	2.965
50	17:00	−7.324	7.031	0.242	1.965	0.010	3.160
51	17:20	−5.801	6.270	0.248	2.090	0.024	2.691
52	17:40	−6.641	6.133	0.238	1.962	−0.080	2.872
53	18:00	−7.578	6.895	0.265	2.253	−0.151	2.921
54	18:20	−7.012	8.438	0.239	1.932	−0.106	4.251
55	18:40	−6.504	5.781	0.245	1.713	−0.054	3.102
56	19:00	−5.508	6.836	0.240	1.834	−0.044	3.163
57	19:20	−4.766	4.902	0.246	1.750	0.018	2.611
58	19:40	−4.707	4.902	0.242	1.667	−0.017	2.686
59	20:00	−5.352	5.117	0.237	1.586	−0.058	3.026
60	20:20	−4.746	6.289	0.247	1.608	−0.048	2.911
61	20:40	−4.258	4.258	0.239	1.441	−0.060	2.968
62	20:40	−4.258	4.258	0.239	1.441	−0.060	2.968
63	20:40	−4.258	4.258	0.239	1.441	−0.060	2.968
64	22:20	−3.926	4.063	0.230	1.278	−0.050	2.844
65	22:40	−4.805	5.293	0.230	1.364	0.029	3.245
66	23:00	−3.711	4.375	0.229	1.307	−0.031	2.877
67	23:20	−4.668	4.355	0.232	1.291	−0.045	2.866
68	23:40	−3.965	4.512	0.229	1.354	0.008	2.862

Table 3.3 Statistics of laser data measured from the Ekofisk platform in the north sea on October 25, 1998. (*Courtesy Statoil Co.*)

File	Time	Min(m)	Max(m)	Mean(m)	STD(m)	Skew	Kurt
1	00:00	-2.642	2.924	21.552	0.938	0.052	2.738
2	00:20	-3.439	4.251	21.512	1.127	0.168	2.801
3	00:40	-2.842	2.870	21.474	0.874	0.086	3.050
4	01:00	-2.754	2.397	21.416	0.792	0.038	2.914
5	01:20	-2.593	2.827	21.357	0.850	0.002	2.811
6	01:40	-2.571	2.801	21.282	0.774	0.048	3.052
7	02:20	-2.372	2.462	21.188	0.770	-0.007	2.993
8	02:40	-2.782	2.613	21.168	0.775	0.061	3.011
9	03:00	-2.159	2.479	21.156	0.706	0.152	3.016
10	03:20	-2.304	2.676	21.109	0.649	0.096	3.318
11	03:40	-1.852	2.103	21.073	0.665	0.038	2.813
12	04:00	-1.919	2.134	21.030	0.668	0.054	2.921
13	04:20	-2.282	2.137	20.960	0.711	-0.035	2.865
14	04:40	-2.040	2.379	20.934	0.664	0.108	3.002
15	05:00	-2.322	2.439	20.920	0.673	0.006	3.183
16	05:20	-2.368	2.027	20.923	0.612	-0.067	3.176
17	05:40	-2.177	2.535	20.919	0.632	0.086	3.166
18	06:00	-2.293	2.687	20.949	0.651	0.073	3.298
19	06:20	-2.592	3.121	20.968	0.666	0.042	3.560
20	06:40	-2.046	2.617	21.001	0.644	0.085	2.870
21	07:00	-2.631	2.667	21.026	0.683	0.080	3.125
22	07:20	-2.141	2.619	21.052	0.722	0.065	2.831
23	07:40	-2.715	3.144	21.064	0.754	0.116	3.463
24	08:00	-2.445	2.487	21.115	0.806	0.096	2.826
25	08:20	-2.820	3.162	21.155	0.818	0.132	3.181
26	08:40	-2.628	3.159	21.225	0.912	0.091	2.776
27	09:00	-3.319	4.030	21.266	1.034	0.152	3.071
28	09:20	-3.032	3.633	21.309	1.067	0.191	2.874
29	09:40	-3.836	5.124	21.335	1.148	0.179	3.591
30	10:00	-3.497	5.170	21.381	1.116	0.172	3.326
31	10:20	-4.541	4.956	21.411	1.341	0.074	3.155
32	10:40	-4.356	4.799	21.425	1.329	0.021	2.907
33	11:00	-3.893	4.603	21.424	1.298	0.149	3.010
34	11:40	-4.323	4.540	21.361	1.361	0.117	3.030
35	12:00	-4.437	5.036	21.320	1.444	0.123	3.101
36	12:20	-4.449	5.634	21.283	1.532	0.113	2.850
37	12:40	-5.170	5.133	21.246	1.720	0.092	2.713
38	13:00	-5.094	7.308	21.200	1.881	0.202	3.144
39	13:20	-5.014	6.510	21.158	1.869	0.134	2.952
40	13:40	-5.815	6.416	21.089	1.883	0.072	2.799
41	14:00	-6.196	6.572	21.050	1.933	0.219	3.010
42	14:20	-7.082	7.567	21.019	2.486	0.121	2.845
43	14:40	-6.287	8.484	20.984	2.508	0.202	2.866
44	15:00	-7.484	11.217	20.934	2.637	0.322	3.210
45	15:20	-6.300	8.348	20.897	2.265	0.199	2.855
46	15:40	-6.041	10.414	20.863	2.348	0.200	3.255
47	16:00	-7.452	9.198	20.819	2.291	0.209	3.322
48	16:20	-6.457	11.658	20.789	2.242	0.234	3.442
49	16:40	-6.838	8.372	20.750	2.368	0.140	2.873
50	17:00	-5.705	6.770	20.735	2.176	0.113	2.690
51	17:20	-5.573	6.390	20.697	2.216	0.127	2.561
52	17:40	-6.060	6.367	20.698	2.013	0.111	2.825
53	18:00	-6.232	7.098	20.697	2.183	0.168	2.724
54	18:20	-5.660	6.938	20.683	2.095	0.227	2.823
55	18:40	-4.907	7.983	20.703	1.804	0.182	3.107
56	19:00	-7.341	8.113	20.686	2.002	0.175	3.035
57	19:20	-5.178	6.126	20.701	1.753	0.184	2.931
58	19:40	-5.264	7.651	20.688	1.937	0.147	2.976
59	20:00	-4.944	5.505	20.691	1.703	0.171	2.918
60	20:20	-5.874	5.967	20.689	1.812	0.192	3.089
61	20:40	-5.378	5.193	20.696	1.683	0.084	3.056
62	20:40	-5.378	5.193	20.696	1.683	0.084	3.056
63	20:40	-5.378	5.193	20.696	1.683	0.084	3.056
64	22:20	-4.983	5.637	20.798	1.560	0.121	2.833
65	22:40	-5.140	5.114	20.812	1.390	0.131	3.341
66	23:00	-3.952	5.765	20.828	1.389	0.155	3.086
67	23:20	-4.144	5.280	20.856	1.479	0.183	2.882
68	23:40	-3.975	4.619	20.854	1.307	0.138	3.239

In general, the deepest troughs for the laser data are shallower than those for the buoy data (See figure 3.10). The laser troughs are 0.5 to 1 meters shallower in the range from -5 to -2 meters and 1 to 2 meters from -8 to -5 meters. Out of the 68 records only 14 had troughs that were deeper for the laser measurements.

Comparison of the highest crest values is displayed in figure 3.11. For low values(2-3 m), some of the buoy crests were higher than the laser by less than 1 meter. However, for larger values (3-12 m), a majority of the laser crests were larger by 2 to 4 meters. These disparities are normally seen in nonlinear waves. A similar relationship is observed for the standard deviations in figure 3.12. For standard deviation less than 1.3 the buoy data were greater and for standard deviation more than 1.3 the buoy values were smaller than the laser data.

Figure 3.13 compares the skewness of the two sets of data. Except for 6 records, the skewness of the laser data were larger than for the buoy data. The buoy values range from -0.15 to 0.15 with a majority of the skewness values below zero. The laser skewnesses range from -0.08 to 0.33 with only 3 values below zero. The skewness is a measure of nonlinearity of the waves. Therefore, the laser data were more nonlinear than the buoy data.

No definite conclusion can be made about the kurtosis values as they vary at will near about 3. This is usually the case for the higher other statistics. The kurtosis values for the laser vary from 2.5 to 3.5 compared to 2.5 to 3.3 for the buoy. The buoy data had one extraneous kurtosis value of 4.25 for record 54 which is not understood. There are no noticeable abnormalities in that wave record.

In summary, a majority of the troughs were shallower and a majority of the crests were larger for the laser data. The Buoy data has properties of a linear Gaussian sea surface and the laser data has nonlinear properties.

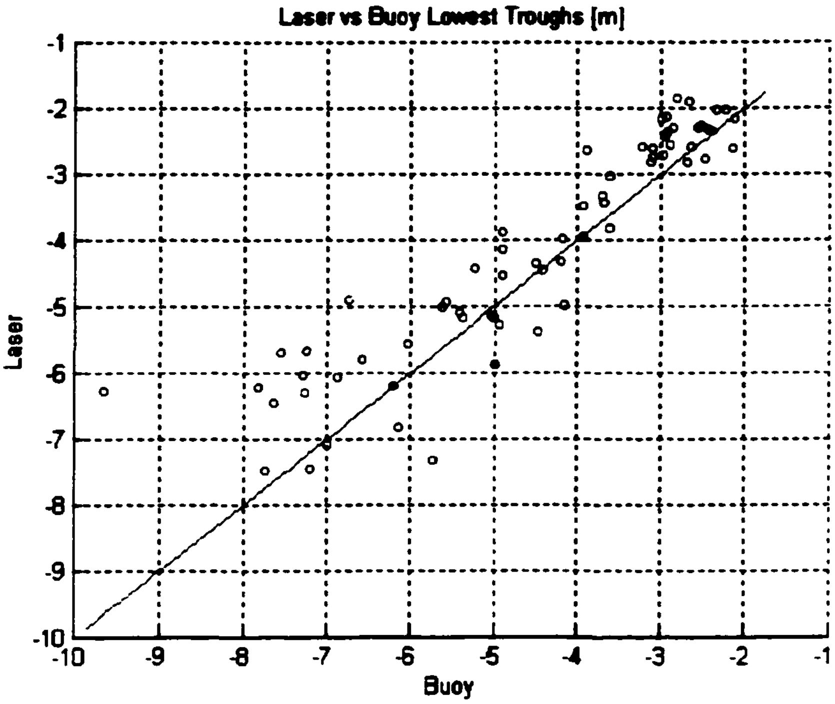

Figure 3.10 Comparison of laser and buoy deepest trough measurements. October 25, 1998. (*Courtesy Statoil Co.*)

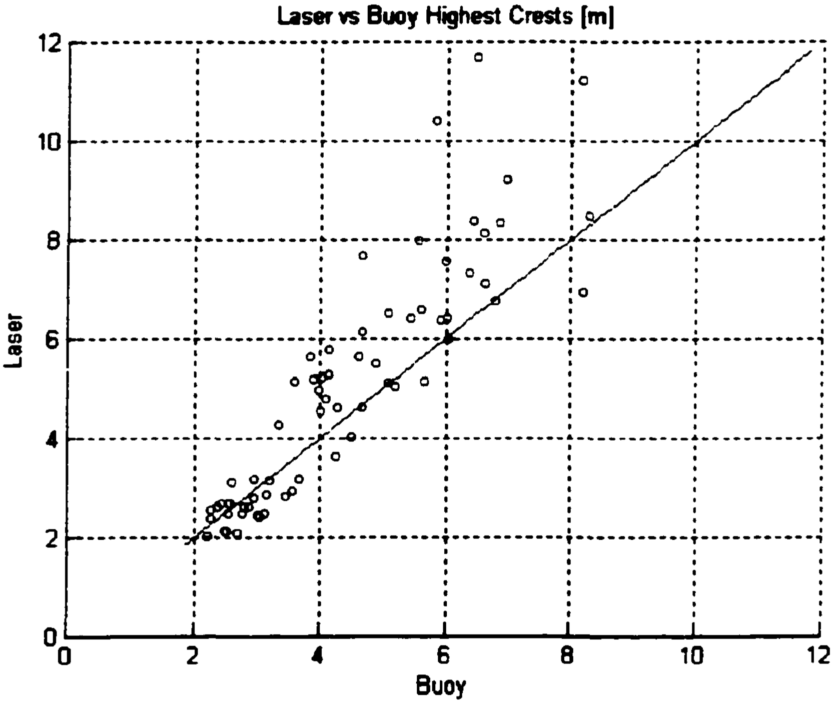

Figure 3.11 Comparison of laser and buoy highest crest measurements. October 25, 1998. (*Courtesy Statoil Co.*)

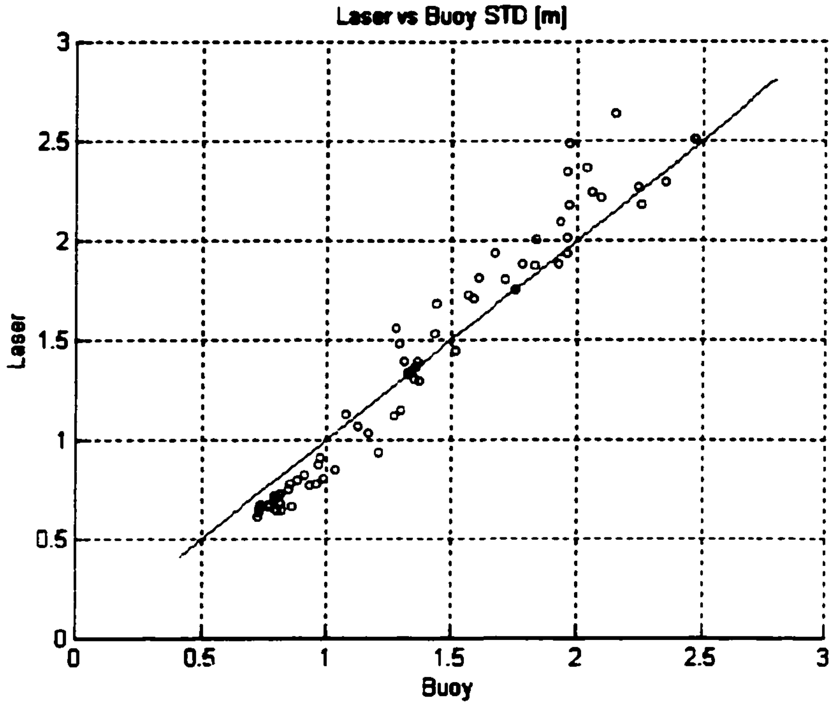

Figure 3.12 Comparison of laser and buoy standard deviation measurements. October 25, 1998. (*Courtesy Statoil Co.*)

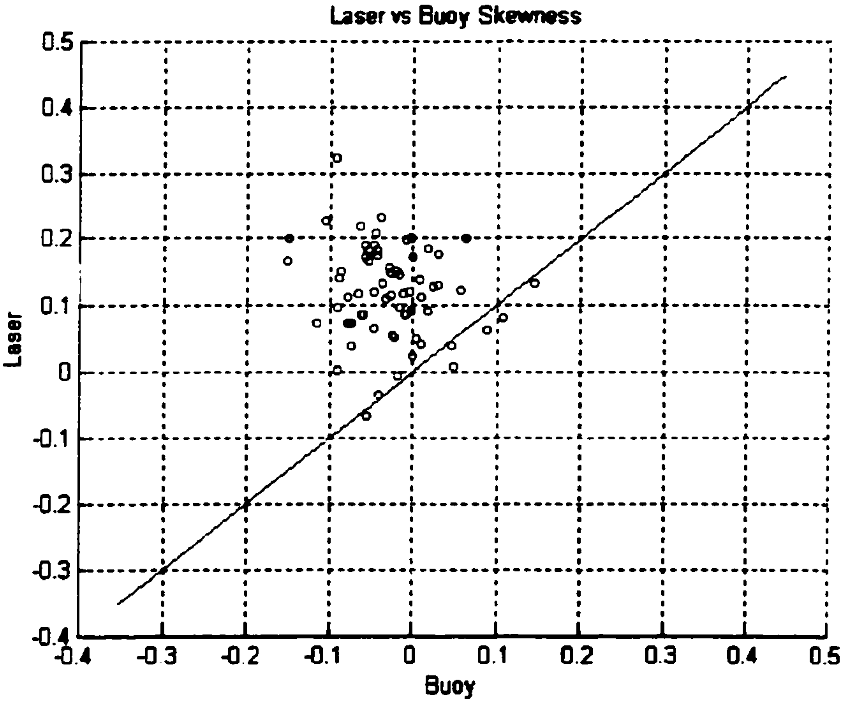

Figure 3.13 Comparison of laser and buoy skewness measurements. October 25, 1998. (*Courtesy Statoil Co.*)

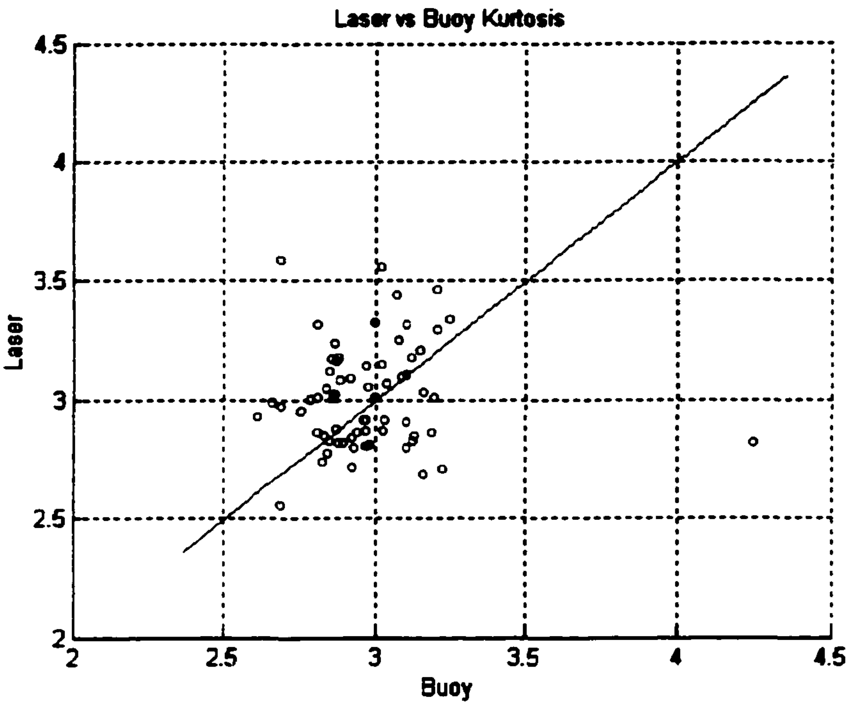

Figure 3.14 Comparison of laser and buoy kurtosis measurements. October 25, 1998 (*Courtesy Statoil Co.*)

Analysis of the Camille data shows that ocean wave records have both linear and nonlinear properties. The linear properties can be modelled by the well known Gaussian stochastic process. However, a method to model the nonlinear properties of the waves has not been developed. Given the available models, the method given in this dissertation may be a giant step in the right direction to model the nonlinear properties of ocean surface waves.

3.2.2 The Pearson System of PDFs

M. A. *Srokosz (1998)* showed results from a reservoir experiment that shows the waves fit a version of the Karl *Pearson (1895)* distribution. In this section, the properties suitable for the analysis of ocean surface waves will be defined. The family of Pearson probability density functions can be put into a standardized form by means of equation (3.8). Equations (3.8) to (3.17) were obtained from an article by *Aroian (1947)*

$$x = \frac{(\eta - \bar{\eta})}{\sigma_\eta} \tag{3.8}$$

where $\bar{\eta}$, the average of the wave record removes any offset and σ_η is the standard deviation. The probability density functions are then determined by the normalized variables, which are the skewness μ_3, and the kurtosis μ_4. The Pearson family of distributions ares based on a differential equation. The family consists of three main types, nine transitional types and the Normal curve. The types are determined by the values of the criterion equation (3.9) and the roots of the polynomial in the differential equation.

$$\delta = \frac{2\mu_4 - 3\mu_3^2 - 6}{\mu_4 + 3} \tag{3.9}$$

For instance, if the skewness is zero and the kurtosis is 3, the Normal (Gaussian) curve occurs. In practice, the types occurring most frequently are I, III, IV and VII.

If the criterion equation, $\delta < 0$, the type I PDF is the result. Srokosz suggested that the type 1 distribution have properties that are very similar to ocean surface wave heights measured in a wave tank (*Srokosz (1998)*). For some values of the kurtosis, the criterion δ can yield a positive value. If $\mu_2 \neq 0$, or small, and $\mu_3^2 < 4\delta(\delta + 2)$, the result is a type IV PDF which is defined over the range from $-\infty$ to ∞. Hurricane Camille data at 1530 and 1600 fits this criterion. Therefore, a type IV PDF would have to be used to represent these records. If $\mu_4 = 3$, the criterion equation (3.9) reduces to equation (3.10). For all skewness values, equation (3.10) would yield a type I PDF.

$$\delta = -\mu_3^2/2 \tag{3.10}$$

The Type I PDF and all its associated parameters are given by equation (3.11) and (3.12) through (3.17), respectively.

$$f_p(x) = \begin{cases} C_p(x - r_1)^{m_1}(r_2 - x)^{m_2} & \text{for} \quad r_1 < x < r_2 \\ 0 & \text{Otherwise} \end{cases} \tag{3.11}$$

$$r_1 = \frac{-\mu_3 + \sqrt{D}}{2\delta} \tag{3.12}$$

$$m_1 = \frac{1+\delta}{\delta}\frac{\mu_3}{\sqrt{D}} - \frac{1+2\delta}{\delta} \tag{3.13}$$

$$r_2 = \frac{-\mu_3 - \sqrt{D}}{2\delta} \tag{3.14}$$

$$m_2 = -\frac{1+\delta}{\delta}\frac{\mu_3}{\sqrt{D}} - \frac{1+2\delta}{\delta} \tag{3.15}$$

$$D = \mu_3^2 - 4\delta(\delta + 2) \tag{3.16}$$

$$C_p = \frac{\Gamma(m_1 + m_2 + 2)}{\Gamma(m_1 + 1)\ \Gamma(m_2 + 1)\ (r_2 - r_1)^{m_1 + m_2 + 1}} \tag{3.17}$$

$$\Gamma(y) = \int_0^{\infty} t^{(y-1)} e^{-t} dt \tag{3.18}$$

The function $\Gamma(y)$ in equation (3.18) need not be for an integer. Interested readers are referred to *Andrews (1998)* for properties of the Gamma functions.

Figure 3.15 shows the range from r_1 to r_2 in terms of the normalized variable, x, as a function of the skewness and kurtosis. The pairs of curves are labeled for different values of the kurtosis, and the value of 3 corresponds to the kurtosis of a normal distribution.

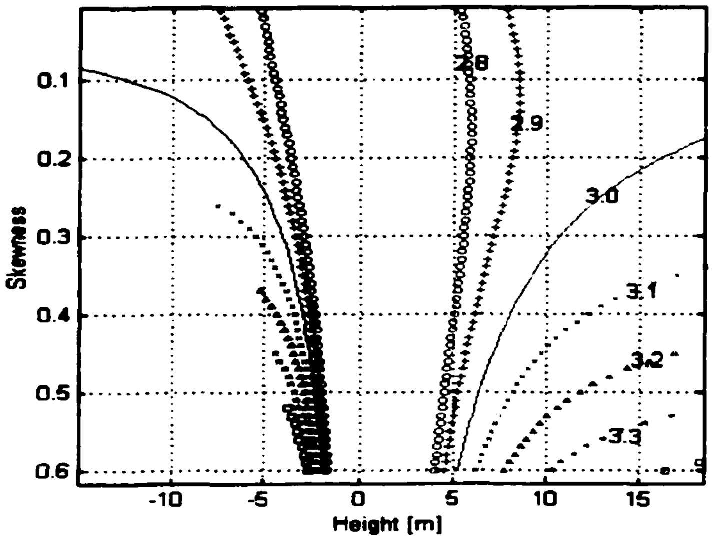

Figure 3.15 Range r_1 (lower bound) and r_2 (upper bound) of possible wave height values as a function of normalized variable, X, and the skewness. Contours are the marked kurtosis values.

For low values of the skewness the values of r_1 and r_2 are less than -10 and greater than +15, respectively. But for a skewness of 0.5, the value of r_1 is approximately -2.5 and r_2 ranges from about 5 to greater values depending on the kurtosis. The missing values for r_1 in the lower left corner for kurtosis of 3.1, 3.2 and 3.3 extends to $-\infty$. These ranges corresponds to values for a type IV Pearson PDF.

These ranges are quite deceptive as shown by *Srokosz (1998)*. The important part of the function for low values of the skewness is always confined to a range that is much smaller than the values that r_1 and r_2 suggest. Therefore, r_1 and r_2 would be the absolute lower and upper limits, respectively.

Table 3.4 gives the values for the parameters that define the Pearson Type I probability density function with a kurtosis of 3 for some rather high values of the skewness. One needs to be careful when computing C_P. If m_1 and m_2 are large (>50), the Gamma function produces very large numbers. The result is a division of two very large numbers. Some computers may not be able to perform the computation because some programs (e.g Matlab) may produce an infinite number for the denominator.

Table 3.4 Parameters for a type I Pearson PDF with a Kurtosis of 3 and for skewness values as shown.

Skewness	r_1	r_2	m_1	m_2	C_P
0.1	-12.34	32.34	108.92	287.09	-
0.2	-6.14	16.14	26	70	3.69e-106
0.4	-3	8	5.27	15.73	7.32e-18
0.5	-2.36	6.36	2.79	9.21	1.37e-9
0.55	-2.12	5.76	2.02	7.20	2.71e-7
0.6	-1.92	5.26	1.44	5.67	1.16e-5

Figure 3.16 shows graphs of the Type I probability density functions for a kurtosis of 3 and for values of the skewness equal to zero (the Gaussian curve) 0.2, 0.4, 0.5 and 0.6. The values for the probability density functions are so small outside the range from -4 to +4 that they plot as essentially zero. Figure 3.17 and figure 3.18 show expanded portions of figure 3.16 so as to illustrate the behavior for low and high values of the normalized variable. The Pearson PDFs have no negative values and their cumulative distributions add up to 1. As will be shown in Chapter 6, there is a PDF used in radar altimeter analysis that do not meet those fundamental conditions.

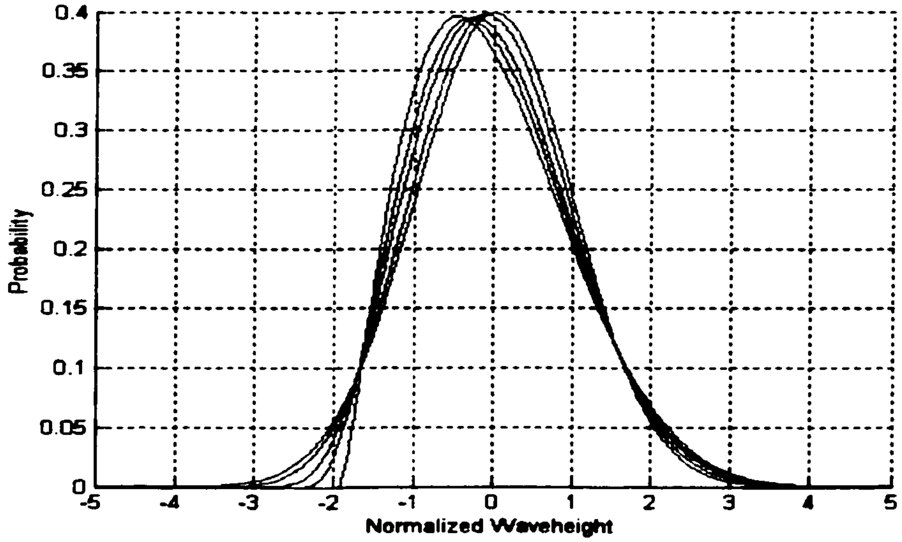

Figure 3.16 Pearson Type I probability density functions for skewness values of 0, 0.2, 0.4, 0.5, 0.6 and kurtosis of 3. (*Pierson and Jean-Pierre (1999)*)

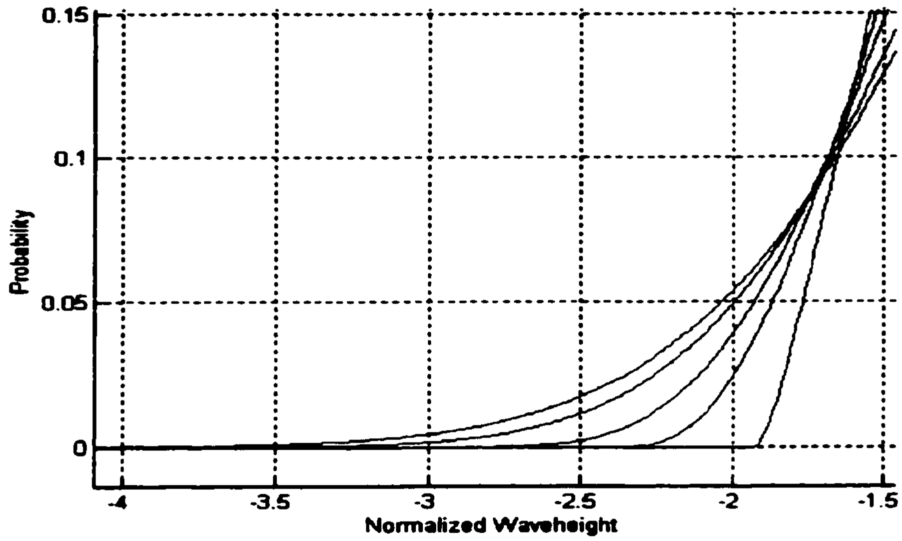

Figure 3.17 Expanded portion of figure 3.16. (Negative tail) (*Pierson and Jean-Pierre (1999)*)

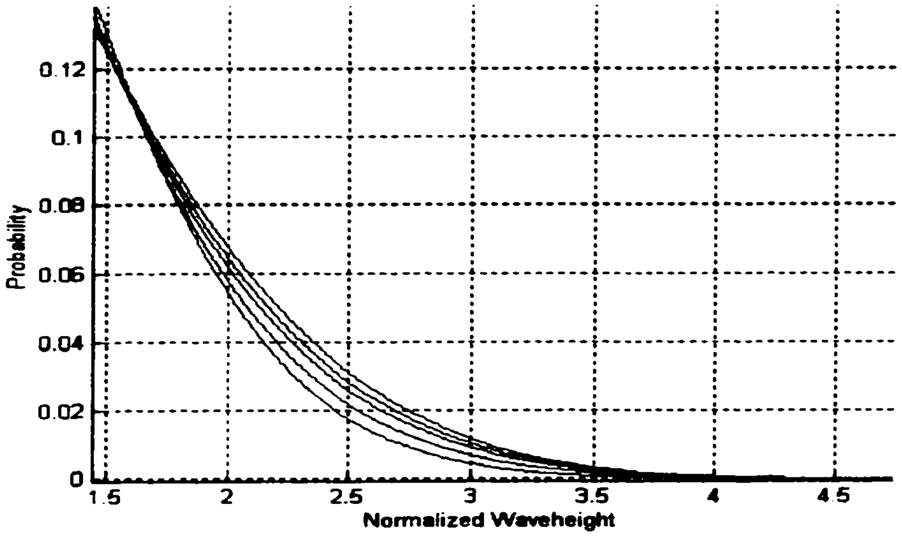

Figure 3.18 Expanded portion of figure 3.16. (Positive tail) (*Pierson and Jean-Pierre (1999)*)

3.2.3 Nonlinear Monte Carlo Simulations

The next step is to transform the linear wave record into a nonlinear wave record. A zero mean, unit normal cumulative distribution function(CDF) and a candidate Pearson type I CDF with a zero mean, unit standard deviation and a selected value for the skewness (and perhaps a kurtosis other than 3) are needed. The CDFs are the integral of the PDFs over the range of definition. The following definitions are from *Pierson and Jean-Pierre (1999)*. They are repeated here as there are minor corrections. The lower limit of equations (3.19) and (3.20) aught to be $-\infty$ and r_1 instead of $-r_1$ and $-r_1$, respectively.

$$F(Y_n) = \frac{1}{\sqrt{2\pi}} \int_{-\infty}^{y_n} e^{-\frac{x^2}{2}} dx \tag{3.19}$$

and

$$F(Y_p) = \int_{r_1}^{Y_p} f_p(x : 1, \mu_3, \mu_4) dx \tag{3.20}$$

The subscript n, is for normal and the subscript, p, is for Pearson. The cumulative distribution functions yield the probability that the random variable, X, is less than or equal to the value at the upper range of integration. The notation, $f_p(x : 1, \mu_3, \mu_4)$, shows that the normalized value for the wave elevation is to be used and that μ_3 and μ_4 are to be chosen. The result is two functions such that the horizontal axis varies as the normalized value of each probability density function and the vertical axis varies from 0 to 1. The Type-I Pearson probability density function can be transformed by a change of variable into the Beta distribution given by equation (3.21)

$$f_B(x) = \frac{1}{B(a,b)} x^{a-1}(1-x)^{b-1} \tag{3.21}$$

over the interval from $0 < x < 1$ where $a > 1$ and $b > 0$ and where $B(a,b)$ is the beta function. The cumulative distribution function given by equation (3.22) is needed.

$$F_B(y) = \int_0^y f_B(x)dx \tag{3.22}$$

The change of variable is accomplished by means of equation(3.23)

$$x* = \frac{x - r_1}{r_2 - r_1} \tag{3.23}$$

since as x varies from r_1 to r_2, $x*$ varies from zero to one. The Beta function is related to the constant C_P in equation (3.24) by

$$B(a, b) = C_P(r_2 - r_1)^{m_1+m_2+1} \tag{3.24}$$

and $a-1 = m_1$ and $b-1 = m_2$. Equations (3.21), (3.23) and (3.24) can be used to return to the CDF for a Type I Pearson distribution. This transformation is described in Appendix A.

The procedure is then to use the values from the linear model, $\eta_n(t_q)$, divide each value by the standard deviation of the data, σ_n. This is the normalized value of the linear model. It is denoted by Y_n on the curve. Find the cumulative distribution of Y_n, $F(Y_n)$. Find Y_p such that the normal distribution, $F(Y_n)$, equals the Pearson distribution, $F(Y_p)$ (ie. $F(Y_n) = F(Y_p)$). Y_p is now the normalized nonlinear representation of Y_n. Note that while Y_n is normally distributed, Y_p is "Pearson distributed". Multiply Y_p by the standard deviation of the data to obtain $\eta_p(t_q)$. The result is a Monte Carlo simulation of a nonlinear ocean wave record.

This transformation is illustrated by figure 3.19 for a skewness of 0.55 and a kurtosis of 3. The cumulative distribution for the normal curve, which is asymptotic to zero at minus infinity, appears in the graph at about -3 normalized units. It has the value of 0.5, as it should, at a normalized value of 0. The cumulative distribution for the Type I Pearson probability density function starts at about $y = -2$ and is identically zero below that. It is above the normal cumulative distribution function between about $y = -1.1$ and $y = +0.8$. For $y > 0.8$ to, at least, the value of + 3.0 the

Type I cumulative distribution function is below the normal cumulative distribution function. For higher values of y, the Type I cumulative distribution function will be equal to one at some value whereas the normal cumulative distribution function is asymptotic to one at infinity. This results in exceptionally high wave crests in the linear model to be reduced in height for the nonlinear representation.

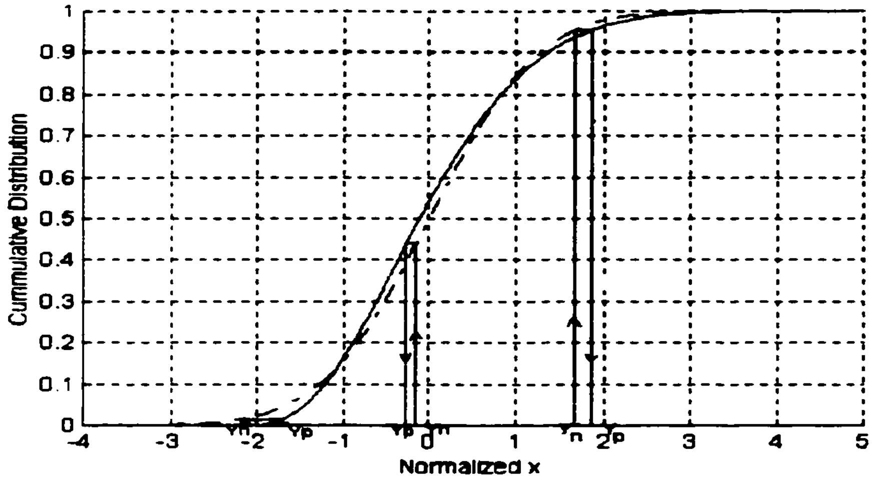

Figure 3.19 Cumulative distribution functions for a normal PDF and for a Type I Pearson PDF with a skewness of 0.55 and a kurtosis of 3. Examples of the required changes from a linear to nonlinear waveform in the three different regions are shown. *Pierson and Jean-Pierre (1999)*

Three of the transformations that happen are shown on the figure. On the left, entering with the value y_n (for normal), finding the normal cumulative probability, going to the corresponding cumulative value for the Pearson curve and finding the resulting value of y_p yields the change from the linear to the nonlinear wave form. Similarly for the middle illustration, entering with the linear value results in a reduction of the value for the nonlinear simulation. For the illustration on the right, the linear value is increased for the nonlinear value.

Values from the linear wave record with normalized values less than about -1.1 will all be increased. Values from the linear wave record between about -1.1 and 0.8 will all be decreased. Values above about 0.8 and less than about 6 will be increased each by an appropriate amount according to the horizontal distance between the two curves. Exceptionally high values from the linear model will be decreased. These values are statistically improbable. The probability of a wave height at 7σ from a normal distribution is essentially zero. Even if these values were to occur in the linear simulation, the properties of the Pearson distribution would restrain these values to r_2.

The result of this transformation is shown in figure 3.20. The transformation was performed on the linear simulation of figure 3.3. The line coded curves for a 30 minute simulated wave record show the original linear model(solid line), the transformation to the nonlinear model(dotted line) and the difference between the nonlinear and linear model(dash). The linear record has a mean of zero ($5.7e^{-17}$ m, a standard deviation of 1.1990 m, a skewness of 0.0265 and a kurtosis of 3.213. The nonlinear record has a mean of zero (-0.0011), a standard deviation of 1.1986 m, a skewness of 0.5936 and a kurtosis of 3.204. See table 3.5 for a direct comparison. As would be expected, the Monte Carlo simulation did not reproduce exactly the values of 0.55 for the skewness and 3.00 for the kurtosis. However, the Standard deviation was fairly close in this particular simulation. Being able to reproduce the standard deviation in the nonlinear simulation is manifested in the closely matched frequency representation of the two signals for the random phase case. The waveform for the nonlinear record has the properties illustrated by the selected segments of the data obtained for Camille.

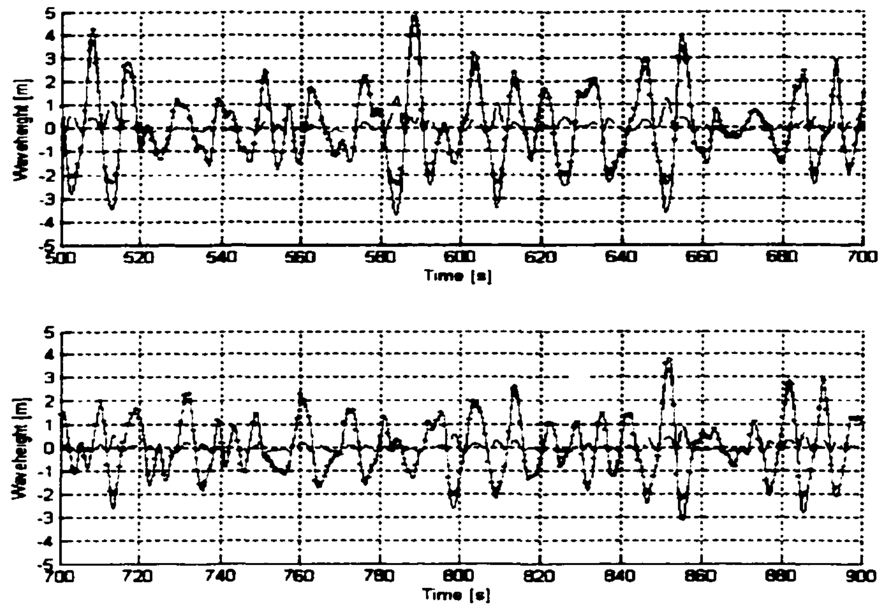

Figure 3.20 Selected portion of a simulated 30-minutes wave record for linear (solid - from figure 3.3), nonlinear (dotted) and the difference (dash) between them. Only random phase is used.

Table 3.5 Statistics for a Monte Carlo simulated 30 Minutes record with a wind speed of 15 m/s and nonlinear skewness of 0.55

-	Min(m)	Max(m)	Mean(m)	STD(m)	Skewness	Kurtosis
Linear	-4.206	4.8330	5.65e-17	1.1990	0.0265	3.213
Nonlinear	-2.434	5.0118	-0.0011	1.1986	0.5936	3.204

The graph for the difference, (Nonlinear record) - (Linear record) is positive both for the higher linear wave crests and for the deeper linear wave troughs. The nonlinear wave crests are higher and the nonlinear wave trough are shallower, or less deep. For the nonlinear record the vertical distance from a wave crest to the preceding, or following, trough is not that much different from the corresponding differences for the linear record. This explains why the significant wave height verifies as well as it does as four times the standard deviation computed from the area under the variance spectrum. The standard deviation changed by only 0.004 m. As a result, the variance spectrum did not change significantly. These comparisons are made in section 3.3.

The expanded segments from these simulated wave records in figure 3.21 were selected to show the more Stokes-like appearance of the waves in the nonlinear simulation. When the simulated waves of figure 3.21 are compared with those of figure 3.8,it is noted that the crests are much higher than the troughs. The original linear simulation in figure 3.3 does not have that property.

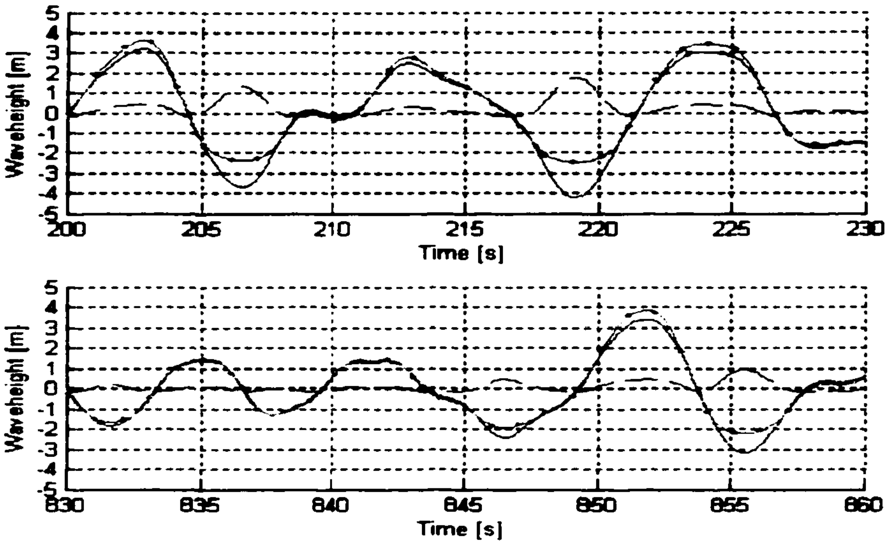

Figure 3.21 Expanded segments of figure 3.20 that shows transformation more clearly.

This result is not a perturbation expansion. It is based solely on a procedure that maps a linear representation of the wave record into a form that has the probability structure and statistical properties of a wave record that could have been obtained by a wave staff or laser for a variety of nonlinear records. This result is very different from the various second order perturbation methods that are described in the literature. If the plots of figure 3.4, figure 3.8, and figure 3.21 are compared, it is noted that the dotted lines of figure 3.21 try to make figure 3.4 resemble more like figure 3.8. This is one of the main focus of this dissertation: to stochastically simulate more realistic wave records.

From figure 3.19, for a standard deviation of $\sigma = 1.199$ m and the chosen value for the skewness $\lambda_3 = 0.55$, there can be no values for the nonlinear simulation outside the interval $r_1 * \sigma < x < r_2 * \sigma$. This corresponds to the absolute minimum value of -2.543 m and absolute maximum value of 6.906 m. Table 3.5 shows the appropriate values for the above simulations. It is noted that the minimum value of -4.206 m obtained for the linear simulations would not be possible.

The nonlinear transformation was performed on the 1000 linear simulations with statistics shown in figure 3.5 and figure 3.6. The resulting statistics are shown in scatter diagrams in figure 3.22, figure 3.23, and figure 3.24. Figure 3.22 shows minimum and maximum obtainable values for 1000 independent nonlinear simulations with only random phase on left, and random amplitude and phase on the right. The values for the random phase are within the absolute minimum and maximum computed above. However, there are a few values that are slightly outside of the absolute minimum for the random amplitude and phase simulation. This is due to the sampling variability as explained by *Donelan and Pierson (1983)*. The absolute interval is a function of the standard deviation and skewness. The variation in these parameters, as shown in figure 3.24, are wider for the random amplitude case. The standard deviation values are between 1.07 and 1.34 meters compared to 1.18 and 1.22 m in figure 3.23.

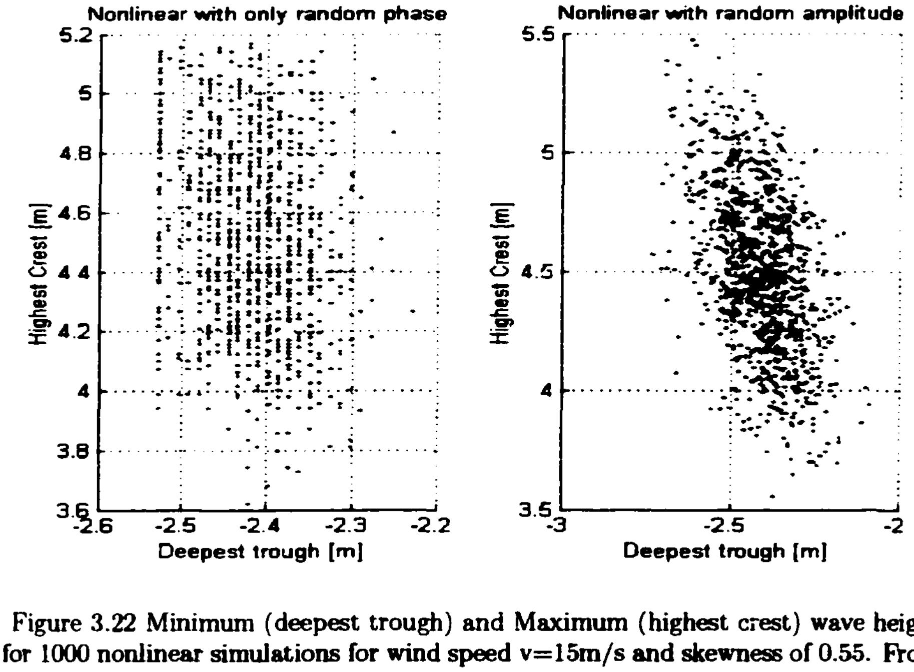

Figure 3.22 Minimum (deepest trough) and Maximum (highest crest) wave height for 1000 nonlinear simulations for wind speed v=15m/s and skewness of 0.55. From left to right are the scatter plot for random phase only, and random amplitude and phase.

Figure 3.23 is a scatter diagram for the statistics of the nonlinear transformation with only random phase. The expected values for the standard deviation of 1.199 m, skewness of 0.55 and kurtosis of 3.0 are recoverable within accepted limits.

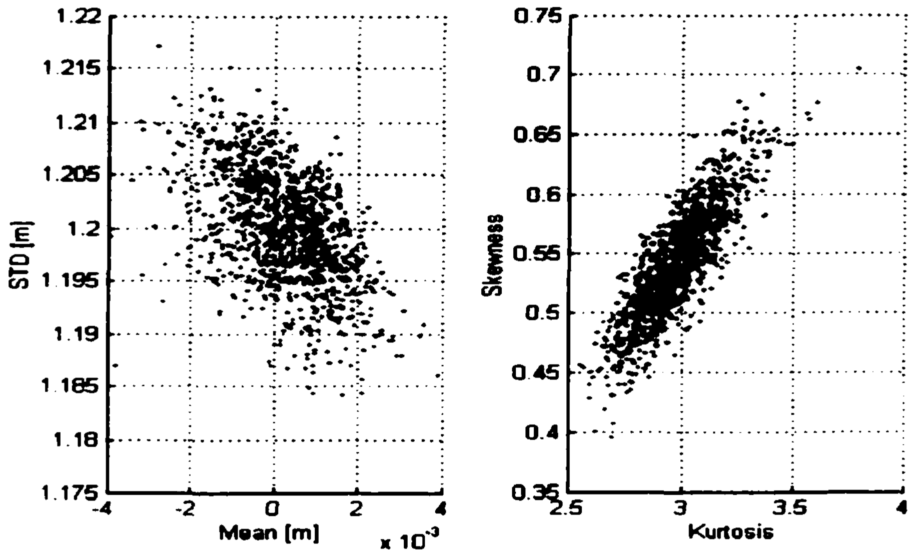

Figure 3.23 Mean, Standard deviation, Skewness and kurtosis distributions for 1000 nonlinear simulations using random phase only for a wind speed of 15m/s and skewness of 0.55.

Figure 3.24 is a scatter diagram for the statistics of the nonlinear transformation with random amplitude and phase.

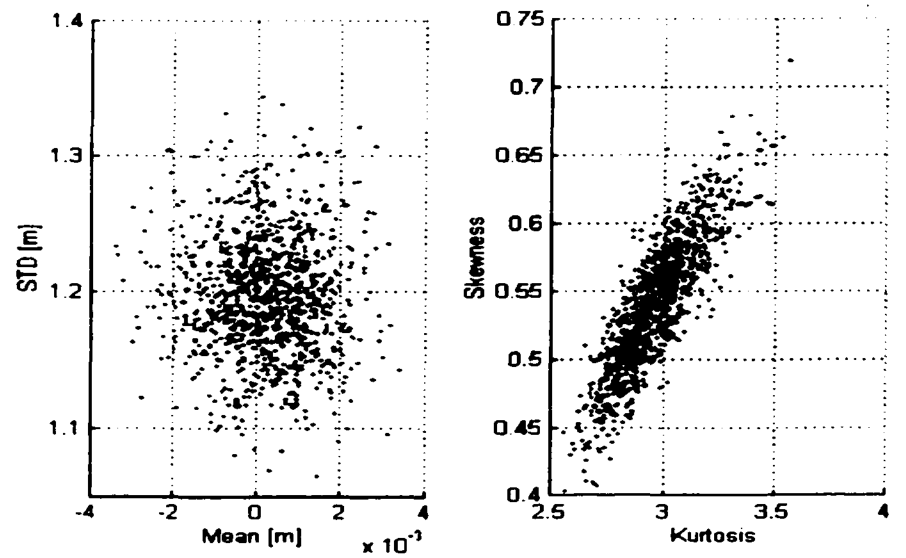

Figure 3.24 Mean, Standard deviation, Skewness and kurtosis distributions for 1000 nonlinear simulations using random phase and amplitude for a wind speed of 15m/s and skewness of 0.55.

The relationship between the input and output skewness values through the transformation is viewed in figure 3.25. The scatter diagram shows that as the input skewness vary from -0.15 to 0.15, the output skewness vary from 0.4 to 0.7. This is a nearly one-to-one relationship. The expected values of 0 and 0.55 is in the middle of the range for the input and output skewness, respectively. In fact, if μ_l is the simulated linear skewness, and μ_{nl} is the nonlinear skewness, μ_{nl} car be approximated by $\mu_{nl} = \mu_l + 0.55$ within ±0.05 with very high accuracy.

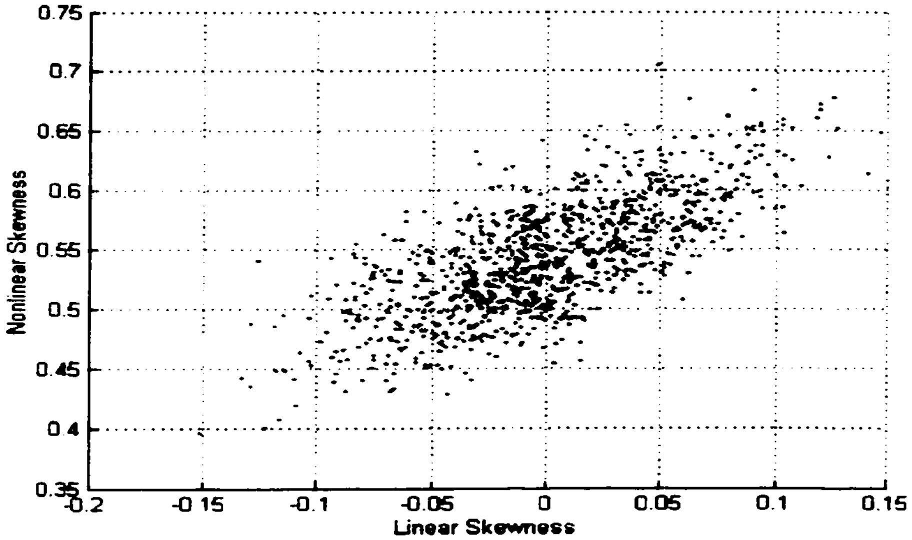

Figure 3.25 Scatter plot of linear versus nonlinear skewness for the random phase case. The wind speed and skewness used were 15 m/s and 0.55, respectively.

3.3 Frequency Representation

Fast Fourier transforms were performed on the wave records of figure 3.20. The result is shown in figure 3.26. Note that the spectra nearly overlap each other. This explain why the standard deviation for the nonlinear simulation did not change by an appreciable amount. The variance is a function of the area under the frequency spectrum. The simulated spectra of figure 3.26 has been smoothed using a 9-point average algorithm. The slight shift of the simulated spectra from the PM spectrum is an artifact of the smoothing algorithm.

When graphed on a linear scale, the simulated linear and nonlinear spectrum can not be distinguished over the range from about 0.4 radians/sec to π radians/sec. There are very small values for the spectrum of the nonlinear values for frequencies less than about 0.4 radians/sec. Plots of the spectra on logarithmic scale in figure 3.27 and figure 3.28 show a better illustration of the differences. Figure 3.28 is a subset of figure 3.27 so as to show the small variations in more details. The spectrum for the linear record is smooth so that the spectrum for the nonlinear record is distinguished by the fluctuations about the smooth linear spectrum, which are hardly discernable in the linear scale.

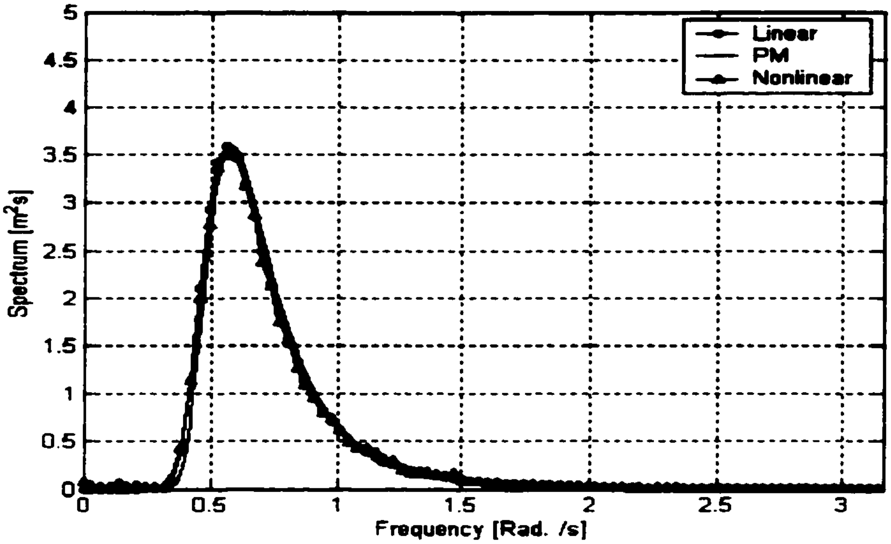

Figure 3.26 The Pierson-Moskowitz spectrum for a wind speed of 15 m/s (solid). Simulated linear (circle) and nonlinear (triangle) spectra with only random phase are shown to overlap. A nine point average has been used to smooth the spectra.

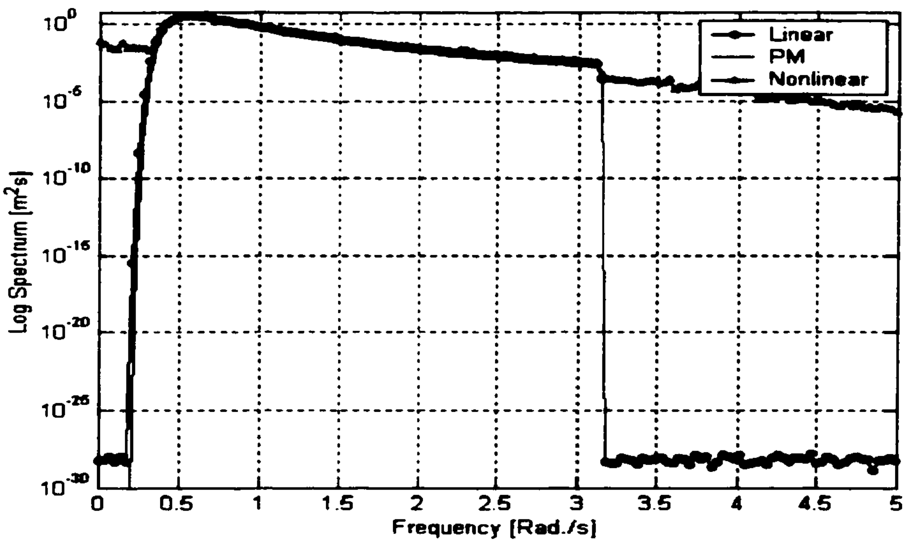

Figure 3.27 The Pierson-Moskowitz spectrum on a logarithmic scale for a wind speed of 15 m/s(solid). Differences in the simulated linear(circle) and nonlinear(triangle) spectra with only random phase are shown. A nine point average has been used to smooth the spectra.

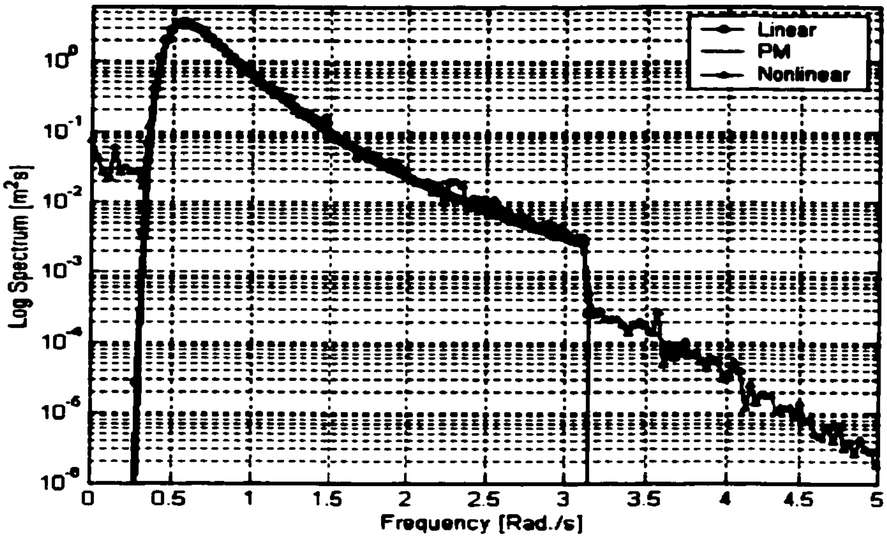

Figure 3.28 Subset of figure 3.27 to show small variations.

In figure 3.28, the sharp drop-offs at the low frequencies of the spectrum for the linear record and at π radians/sec are properties of the linear record, which had no contributions for low frequencies and those above the deliberately chosen Nyquist frequency. The simulations were performed over the frequency ranges from 0 to π.

Since the records were evaluated every tenth of a second, values for the spectrum of the nonlinear simulation could have been evaluated for frequencies as high as 10π radians/sec. As shown by the figure, the variance spectrum of the nonlinear simulation has components that are about two orders of magnitude lower than the spectral peak at low frequencies and there are contributions that begin an order of magnitude lower beyond the Nyquist frequency of the linear model.

The simulated wave records have been done in a way that corresponds to the way that wave spectra are presently estimated. The nonlinear details of the original wave records are lost by these methods. Actually the Fast Fourier Transform *(Cooley 1987, 1992 and Cooley and Tukey 1965)* is a one to one transformation from the time domain to the frequency domain. If say, 18,000 data points as in $\eta(0)$, $\eta(1)$, $\eta(2)$, ... $\eta(P)$,...$\eta(17999)$ are available, then the FFT in complex notation will yield 9000 Fourier coefficients for the cosine terms and 9000 Fourier coefficients for the sine terms. Assuming the Nyquist criterion is observed, the original series for the waves can be recovered exactly by inverting the values in the frequency domain.

Figure 3.29 is a graph of a spectrum that results from randomizing both the phase and amplitude of the Fourier frequencies. Although very rough, the simulated nonlinear spectrum overlaps the simulated linear spectrum. Again, the variance was conserved through the transformation. For this particular simulation the peak in the spectrum occurred at a frequency near that for the PM spectrum. Repeated simulations, however, which would be much more realistic, would shift the peak in the spectrum over a wide range of values for the frequency as shown by *Donelan and Pierson (1983)*.

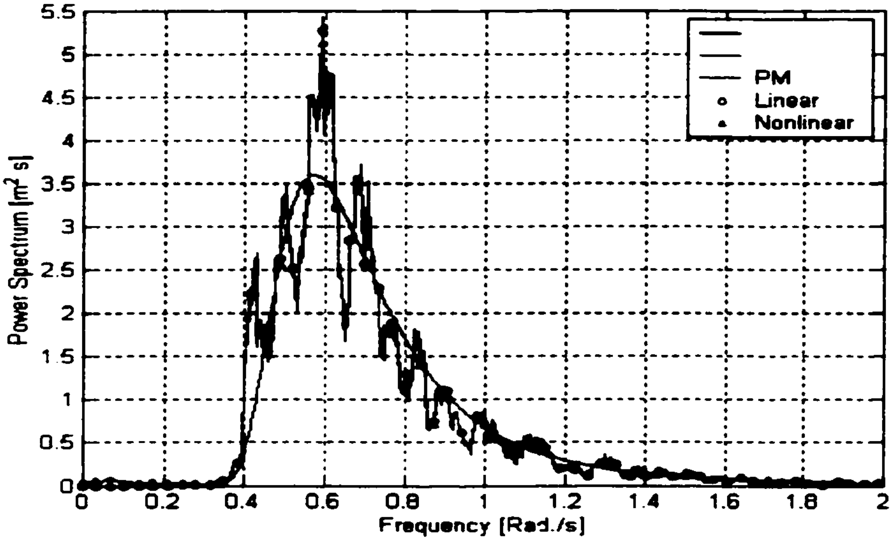

Figure 3.29 The Pierson-Moskowitz spectrum for a wind speed of 15 m/s (solid). Simulated linear (circle) and nonlinear (triangle) spectra with random amplitude and phase are shown to overlap. A nine point average has been used to smooth the spectra.

Comparison of the spectrum for the Camille record 0700 with the PM spectrum for a wind speed equal to 15 m/s in figure 3.30 show some similarity with figure 3.29. Camille record 0700, in table 3.1, has a standard deviation of 1.188 m and a skewness of 0.132. These values are within the range of values one would obtain for a Monte Carlo simulation of ocean waves using the equation for random amplitude and phase and the PM spectrum for a wind speed of 15 m/s. Figure 3.6 shows the comparative values. These simulations seems to be more realistic in the frequency domain representation than the simulations obtained using only random phase.

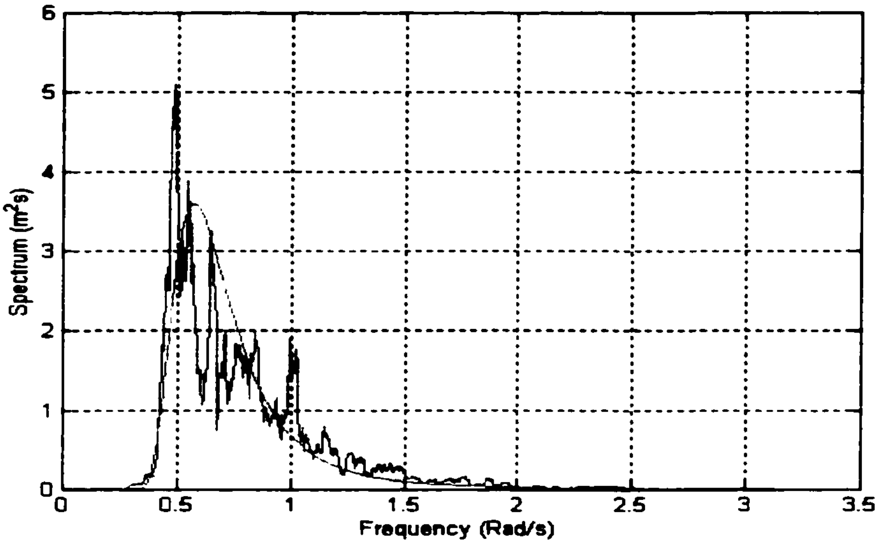

Figure 3.30 Spectrum of the Camille record 0700 (table 3.1) compared to the Pierson-Moskowitz Spectrum using a wind speed of 15 m/s.

The statistical properties of the linear and nonlinear simulations with random phase, and random amplitude and phase was shown in the previous sections. Figure 3.31 and figure 3.32 show the scatter plot of the spectral peak amplitudes versus frequency for the random phase, and random amplitude and phase cases, respectively. The peak value of 3.594 m^2s occur at 0.5725 rad./s for the PM spectrum for a wind speed of 15 m/s. For the random phase case, the spectral peak vary from 3.35 to 3.8 m^2s with high concentration near 3.6 m^2s, and the frequency vary from 0.52 to 0.60 rad./s. For the random amplitude and phase case, the spectral peak vary from 3 to 9 m^2s with high concentration near 5 m^2s, and the frequency vary from 0.45 to 0.8 radians/s. Figure 3.32 does not appear to plot for the chosen discrete frequency components, compared to figure 3.31, because it is plotted for a wider range of frequencies.

Despite these variations in the frequency domain, the recovered statistics through the transformation are within acceptable values. This proves the point that the frequency spectrum does not contain the nonlinear information for actual nonlinear ocean waves.

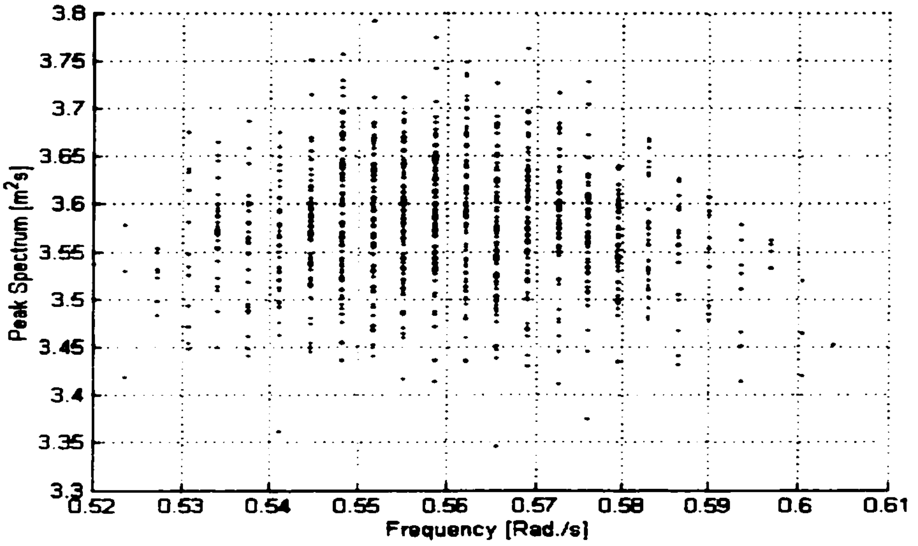

Figure 3.31 Scatter plot of the spectral peak for 1000 30-minute simulated nonlinear records using only random phase. (v=15 m/s, $\mu_3 = 0.55$)

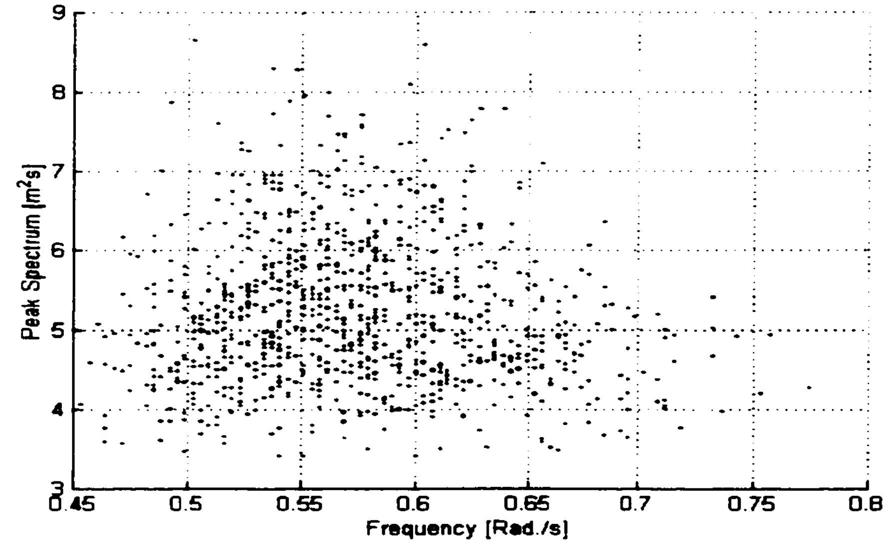

Figure 3.32 Scatter plot of the spectral peak for 1000 30-minute simulated nonlinear records using random amplitude and phase. (v=15 m/s, $\mu_3 = 0.55$)

Donelan and Pierson (1983) studied 16 17-minute sample of laboratory generated wave records under controlled conditions and 8 17-minute wave records in the field where the winds were fairly stable. There follow a summary of their findings.

1. The frequency of the spectral peak and the value of the spectral peak vary randomly for the laboratory and field experiments.
2. The spectra had multiple maxima.
3. If a spectral peak is chosen at random, there is a 50% chance that the value is greater or less than the true value.
4. The average of spectral peaks of the same stationary random process is higher than the estimate of the true spectral peak. Thus scaling the Spectrum by f/f_m, f_m being the peak frequency, biases the spectra towards values that are too high.
5. As also shown in *Pierson (1977)*, The spectral peak is an overestimate of the true spectral shape near the peak and the frequency of the spectral peak varies randomly about a value estimated by combining the entire data sample.
6. The computed variance of an ocean wave record are not independent. The areas under the individual sample spectra are random variables. The distribution of the estimates of the variance of a time history is not known but can be approximated. Assuming that the spectrum is a slowly varying function of frequency, an approximation can be found using the Total Degree of Freedom (TDF).
7. A lot of data is needed to have enough independent samples to get reasonable estimates for the variance.
8. Smoothing the spectrum compounds the effects of sampling variability.

In conclusion, they stated that the significant wave height, $(H_{1/3})$, is not known to within $\pm 10-15\%$ of an estimated value. The spectral peak is typically an overestimate of a value that would be obtained from a larger sample; and the frequency of the peak is not known to within a range of ±5% of its true value.

All these random variations are verified in the statistics of the simulations presented in this dissertation. In general, much larger independent samples are needed to obtain more accurate estimates for the higher order statistics such as skewness and kurtosis.

Chapter 4

4.0 Other Methods and Reality Check

4.1 Perturbation Expansions

As the previously derived method does not depend on perturbation theory, it is discussed here to show difficulties in methods using the theory. Perturbation expansions to represent waves have been described by *Tick (1954)*, *Longuet-Higgins (1963)*, and *Dalzell (1982, 1989)*. Each one of these authors used a different method. Dalzell (1982) used a third degree functional polynomial and described some third order equations. *Longuet- Higgins (1963)* used a perturbation expansion of the hydrodynamic equations and obtained results for short crested waves. *Tick (1959)* also obtained a representation for the second order spectrum.

An extension to third order for any of the above methods has two major difficulties. The first is that the linear dispersion relationship no longer applies so that either the wavenumbers change in the sum if the frequencies are kept constant or the frequencies change if the wavenumbers are kept constant. The second difficulty is that of satisfying the kinematic and Bernoulli boundary conditions on the free surface. The potential function is usually fairly complex (see equation 2.11). A way to satisfy the kinematic and boundary condition on the free surface is to expand the exponential term in the potential function in a Maclaurin series as a function of the free surface.

The usual representation for a wave record by means of these methods is to Monte Carlo a representation of a second order perturbation. These simulated records have somewhat higher crests and less deep troughs along with some of the desirable properties of nonlinear waves. They are also Monte Carlo simulations as in the above derivation.

4.2 Breaking and Freak Waves

To date, the laser data from the "Draupner" platform have not been analysed for breaking activities. A wave staff record as a function of time does not provide information on whether the wave is breaking. Neither do the Monte Carlo simulations of waves in a probability model. The much higher wave crests that can result from this present model may, at times, not actually be possible.

Visual observations of waves, as from an aircraft, show that spilling breakers are typical of a wind generated sea. The waves form patterns as groups. As an individual wave crest progresses from the rear of the group to the middle of the group it will often break and form a patch of foam that remains behind and gradually disappears as the wave re-forms and continues on its way. These breaking events limit the crest heights of the waves and force the seaway to be, in some sense, more nearly linear. There is the interesting possibility that the results presented here could be used to model breaking events in a more realistic way. The restriction provided by r_2 from the Pearson distribution might reduce extremely high wave crests from the linear simulations.

Buchner (1996) defines "green water" as "the solid water which comes on the deck of a ship in large waves". The equations that are used to describe the effects of green water on structures designed to protect the ship's bridge from damage and the forces on these structures are quite different from those that could possibly define the nonlinear properties of the waves in the absence of breaking. The equations that describe the water motion in that part of a wave that has broken are no longer those that describe unbroken waves. *Buchner (1996)* and *Grochowalski, et al (1999)* describe some of the features of green water on the deck of a ship.

Grochowalski, et al (1999) have treated the effects of green water on the deck of a small ship after a wave has broken over the deck. It was necessary to derive two new systems of equations to describe the motions involved and to determine the transformations necessary to go from one set of equation to another.

"Green water" that is found on the bridge of a ship can be considered to have come from a "freak wave". Freak waves are unexpectedly large or abnormal waves that are beyond the extreme waves typically experienced by marine structures. They are often referred to as "the one from nowhere" (*Haver and Anderson (2000)*). A wave has the potential to be considered as a freak wave, if "the wave crest height is 20% larger than the significant wave height (SWH)" (*Haver and Anderson (2000)*). This measure is based on a 20-minutes wave record.

These giant waves have caused a lot of casualties at sea. Over the years, there has been a number of ships disappearing without trace in heavy weather. *Sand et al. (1990)* report a case in the Ekofisk field, where local structural damage was reported more than 20 meters above still water level. *Kjeldsen (1996)* reports the cause for the capsizing of the semi-submersible, Ocean ranger, as due to flooding in the control room. There is a possibility that these events could have been the effect of freak waves.

There follow an example of a freak wave as measured from the "Draupner" platform on January 1, 1995. The 20-minute wave time history in figure 4.1 was measured by a down-looking laser. The laser sampled the ocean surface at approximately 2.133 Hz so the time steps are 0.469 s. The statistics for this record are: lowest trough, -7.13 m; highest crest, 18.50 m; mean, 0 m; standard deviation, 2.98 m; skewness 0.41; kurtosis, 4.06. By the measure of the skewness value, this is a highly nonlinear wave record.

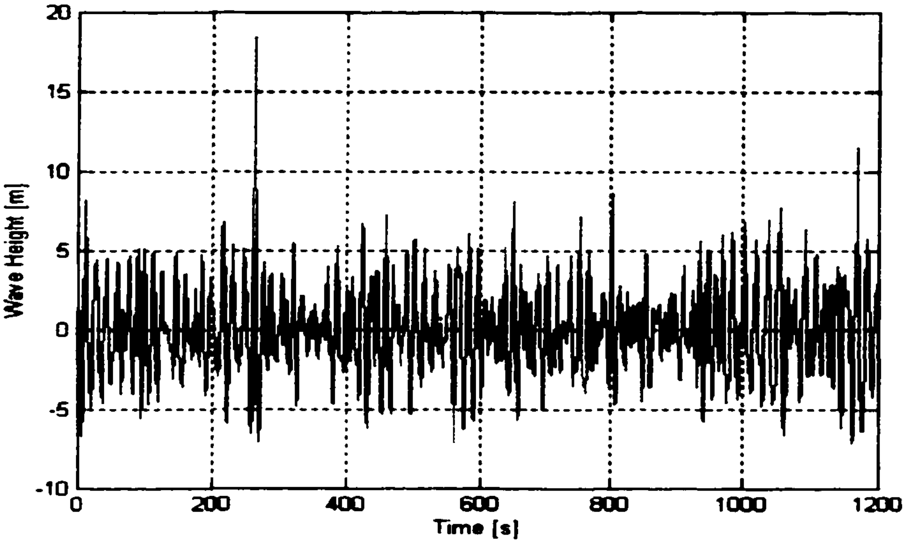

Figure 4.1 20-minute laser data recorded at "Draupner", January 1, 1995. (*Courtesy Statoil Co.*)

The significant wave height as computed from four times the standard deviation is 11.92 m. When the highest wave from that record (figure 4.2) is extracted, the height is measured at 25.26 m. The wave height is measured from trough to crest. This wave height is more than two times the SWH. According to the "greater than 20%" criteria established by *Haver and Anderson (2000)*, this more than satisfies the freak wave criteria. The minimum wave height to satisfy Haver and Anderson's criteria for the measured SWH is 14.41 m.

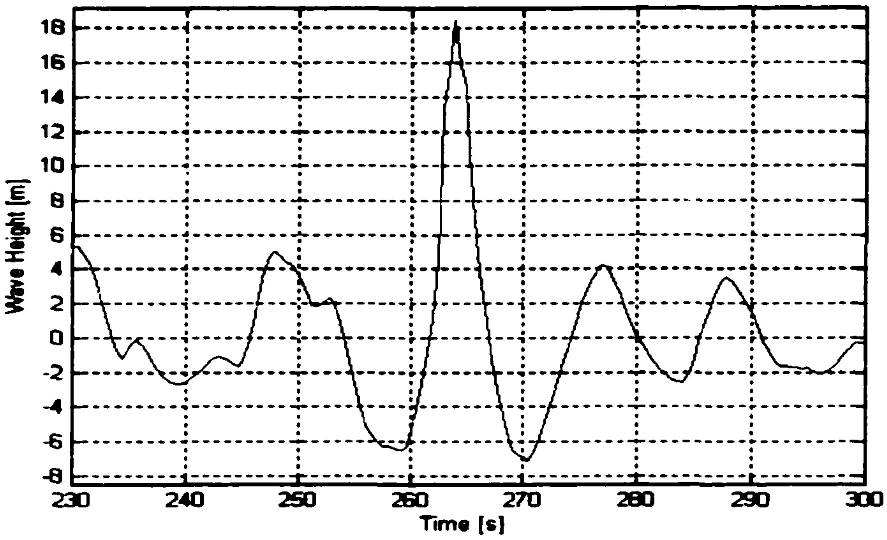

Figure 4.2 Freak wave - subset of figure 4.1. (*Courtesy Statoil Co.*)

If a small boat encounter such a freak wave, there is no doubt that it will experience severe damages. It can even sink and claim many lives.

The phenomena needed for even explaining freak waves are no yet resolved. It is not a surprise that the probabilistic method to simulate nonlinear ocean waves, as presented in Chapter 3, can not model these events.

4.3 Discussion

Nonlinearity is a matter of degree. For the subtropical highs such as the horse latitudes, the passing swell from a distant cyclone could be very nearly linear. Storm generated waves, conversely, could be very nonlinear. Although the mathematical formulation involves the kinematic boundary condition, it is clear that it is violated by spilling breakers or, so called, "whitehorses". The method of Monte Carlo simulation is nevertheless a way to obtain a more realistic representation for the waves. The proper choice for a particular application of the values for the skewness and kurtosis must await the analysis of more wave staff data as keyed to the wave spectral estimates and the wind and weather conditions. The high value of the skewness that was used is, in some sense, an upper bound on possible values. Further studies in this area should include calculations for skewness values of 0.4, 0.3, 0.2 and 0.1 and for kurtosis values of 2.95, 3.00 and 3.05 to form the envelope of possible nonlinear wave forms for this and other selected spectra.

To fully describe the properties of waves, η needs to be defined as a function of x, y, t as in equation (4.1).

$$\eta(x,y,t) = \sum_{i=1}^{I}\sum_{j=1}^{J} a_{ij} \cos\left[k_i\left(x\cos\theta_j + y\sin\theta_j\right) - w_i t + \varepsilon_{ij}\right] \tag{4.1}$$

$$S(w,\theta) = S(w)F(w,\theta) \tag{4.2}$$

$$a_{ij} = \sqrt{2S(w_i,\theta_j)\Delta w \Delta\theta} \tag{4.3}$$

Where a_{ij} (4.3) is obtained from a given directional spectrum $S(w,\theta)$ (4.2). ε_{ij} are random distributed phases from 0 to 2π. $S(w)$ is as defined in section (3.1), and $F(w,\theta)$ is the directional spreading function. Δw and $\Delta\theta$ are obtained by quantizing $S(w,\theta)$ into I and J subintervals, respectively. This much more complicated problem will not be solved in this dissertation.

In a paper entitled *Known and unknown properties of the two dimensional wave spectrum and attempts to forecast the two-dimensional wave spectrum for the north atlantic sea,* Pierson wrote: "For some applications of the power spectrum, it is desirable to be able to describe the sea surface as a function of distance instead of as a function of time at a point. This involves the transformation of ω,θ ...... A discussion in the Ocean Wave Spectra suggested that k did not seem to be given by ω^2/g, but since then Mr. Cartwright of the National Institute of Oceanography has informed me that subsequent analyses all verify this linear representation between wave number and frequency to within the present accuracy of the available data. This result does not eliminate the problem completely as nonlinear effects of a more subtle nature are present. It will be a long time before these nonlinear effect are completely understood." (*Lunde (1964)*)

This is the approach taken in the next chapter. Using the dispersion relationship, the frequency spectrum of equation (3.1) is reformulated to a wavenumber spectrum. Ocean wave profiles are then simulated as a function of distance. The statistics from these simulations are used to show how the nonlinear effects can be used to better understand radar returns at low grazing angle.

Chapter 5

Spatial Representation of Waves and Applications

5.1 Overview

One of the most important issues in ship self defense against incoming low-flying Anti-Ship Cruise Missiles (ASCMs) is the degradation of radar measurements by multipath. This is the scattering of microwaves at the sea surface that occurs both on the outgoing transmitted signal and the returning echo. The scattered energy mixes with the direct ray and confounds the received signal to introduce large errors in the determination of threat elevation.

The problem has proven difficult because of the complexity of the sea scatter. Recently *Groves and Chow (1998)* have proposed a simple formulation that may enhance the trackability of low flyers. Their method uses estimates or predictions of the ocean surface wave frequency-direction spectrum, which can be transformed to a wavenumber direction spectrum, for a linear simulation of the waves. The sea-surface information needed is the tri-variate Probability Density Function (PDF) of the surface elevation and 2 slope components. The question then arises of how well this PDF is determined by the frequency-direction spectrum and whether it can be transformed to represent a realistic nonlinear surface.

If the sea surface were governed by linear dynamics, it is generally accepted that the elevation-slope PDF would be Gaussian and completely determined by the wave spectrum. But it is also known that the linear assumption fails to give an adequate description of the sea surface in other contexts. A Gaussian sea surface would appear statistically the same if viewed from below as from above. However, the wave crests are obviously narrower than the troughs, and the small waves are different on the crest of a long wave than in the trough. These effects result from the nonlinear interaction between waves in different parts of the spectrum. These features were evident in the wave staff and laser data analysed in chapter 3. The equations that describe gravity waves are nonlinear. A linear model for the waves, as used by *Groves an Chow (1998)*, is simply an approximation.

This chapter attempts to get a higher-fidelity PDF from the wave spectrum without understanding the hydrodynamics. The elevation PDF has been found to closely match the *Pearson (1895)* Type I function by *Srokosz (1998)*. It was verified by *Pierson and Jean-Pierre (1999)* and is further described in chapter 3. Applying the transformation to the elevation at each point of a Gaussian sea surface makes the elevation PDF agree closely with the PDF obtained from actual wave measurements. How this transformation affects a simplified version of the elevation-slope PDF is the main focus of this chapter.

5.2 Nonlinearization of the Wave Profile and Numerical Distribution

In order to understand the scattering phenomena and its statistics, it is very important that one understands the statistics of the scattering medium. *Trizna (1991)* states: Radar sea scatter ".. statistics are required for the calculation of detection probabilities of targets in sea clutter, and the capabilities of the detection algorithms used depend upon appropriate characterization of the sea echo statistics." In this section, a method for estimating the elevation-slope PDF of the ocean surface is considered. For simplicity and visibility only slopes in the x-direction (i.e. wave profile) $f(\zeta, \zeta_x)$ is considered. The inclusion of the slope in the y-direction $f(\zeta, \zeta_x, \zeta_y)$ will eventually be needed.

First, an ocean wave profile is defined. From equation (3.1), the dispersion relationship ($k = \omega^2/g$) is used to obtain the wavenumber spectrum in equation (5.1). The characteristic shape of the Pierson-Moskowitz wavenumber spectrum for a wind speed of 15 m/s is shown in figure 5.1.

$$S(k) = \frac{\alpha}{2k^3}\exp\left[-\beta\left(\frac{w_0^4}{(gk)^2}\right)\right] \tag{5.1}$$

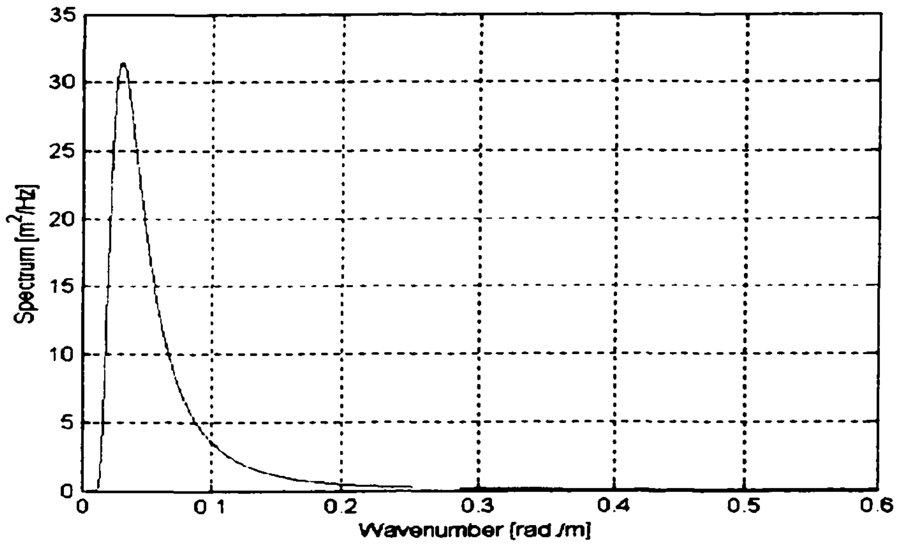

Figure 5.1 The Pierson-Moskowitz wavenumber spectrum for a wind speed of 15 m/s

$$\eta(x) = \sum_{i=1}^{N} a_i \cos(k_i x + \epsilon_i) \tag{5.2}$$

Second, an ocean wave record as a function of distance along a line (5.2) is generated in the same manner equation (3.2) was obtained. Similarly, the Fourier coefficients a_i at wavenumber k_i are obtained from $a_i^2/2 = S(k_i) * \Delta k$. Therefore $a_i = [2S(k) * \Delta k]^{1/2}$. This model is one of the most used models for generation of ocean wave profiles (see *Broschat (1993), Borgman (1990), Kinsman (1984)*) . To recap, this represents a normally distributed wave with zero mean and a standard deviation equal to the square root of the variance computed from the area under the spectrum S(k). As shown in section 3.2.1, analysis of actual ocean waves shows that the waves can be nonlinear. The nonlinearity is manifested by the fact that the wave crests are usually much higher and narrower than the troughs with respect to the mean. In similar fashion to the time series analysis, the Pearson distribution (5.3) is used to introduce the nonlinear effects to equation(5.2). The whole transformation is described in *Pierson and Jean-Pierre (1999)* and Section 3.2 in detail. Here only the effects of the Pearson distribution (5.3) on the resulting nonlinear transformation is shown in figure 5.2. Unlike the normally distributed wave record of (5.2) the Pearson distributed wave record is bounded from the bottom by r_1, and from the top by r_2, which are functions of the skewness values μ_3.

$$f_p(\zeta) = \frac{\Gamma(m_1 + m_2 + 2)}{\Gamma(m_1 + 1)\Gamma(m_2 + 1)(r_2 - r_1)^{(m_1+m_2+1)}}(\zeta - r_1)^{m_1}(r_2 - \zeta)^{m_2} \qquad for \quad r_1 < \zeta < r_2 \qquad (5.3)$$

m_1, m_2, r_1, r_2 are functions of μ_3 and μ_4 which are the skewness and kurtosis respectively. See section 3.2.2 for a complete description of the variables. The differences between these two curves are similar to those of figure 3.21. To be exact, the nonlinear crests are higher (distances 7.483 and 7.495 $* 10^4$ m) and nonlinear troughs are shallower (distances 7.489 and 7.505 $* 10^4$ m).

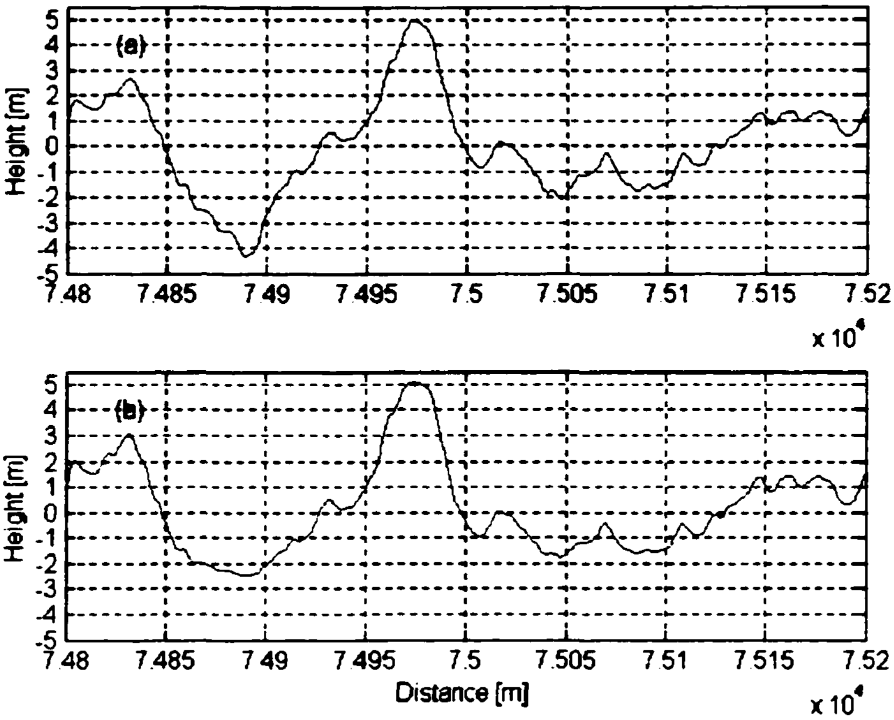

Figure 5.2 Section of a wave profie for a a) Linear Monte Carlo simulation using the PM spectrum for wind speed of 15 m/s and b) nonlinear transformation with a Pearson distribution for skewness $\mu_3 = 0.5$ and kurtosis $\mu_4 = 3$. (*Jean-Pierre et al. (1999)*)

The noisier(high frequency oscillation) spatial domain representation (figure 5.2) of the surface waves compared to the time domain representation(figure 3.21) can be explained by looking at their respective specta. The frequency spectrum(figure 3.1) varies as omega to the -5 whereas the wavenumber spectrum(figure 5.1) varies as k to the -3. The speed of a wave is inversely proportional to the wavenumber ($v = \sqrt{\frac{g}{k}}$). Conversely, the speed of the waves is directly proportional to the wavelength. The shorter waves travel more slowly and take longer to pass a point in the time record. There are more short waves in the space record compared to the time record.

From the wave profile data of figure 5.2, the slope vector can be computed.

Let

$$\eta(x) = \eta(x_1)\ \eta(x_2)\ \eta(x_3)\ \ldots\ \eta(x_I) = \eta(1)\eta(2)\eta(3)\ \ldots\ \eta(I) \qquad (5.4)$$

The slope or the derivative of η with respect to x is defined by

$$\eta_x = \frac{\partial \eta}{\partial x} = \eta_x(1)\ \eta_x(2)\ \ldots\ \eta_x(i)\ \ldots\ \eta_x(I) \tag{5.5}$$

where

$$\eta_x(i) = \begin{cases} \frac{\eta(i+1)-\eta(i-1)}{2\Delta x} & \text{for } i = 2 \ldots I-1 \\ \frac{\eta(2)-\eta(1)}{\Delta x} & \text{for } i = 1 \\ \frac{\eta(I)-\eta(I-1)}{\Delta x} & \text{for } i = I \end{cases} \qquad \text{and } \Delta x = x(i+1) - x(i) \tag{5.6}$$

Note the Δx is the sampling interval of the wave profile. It is a constant defined to obey the Nyquist theorem. The derivative is so defined to keep the number of values the same as the original profile.

5.2.1 Statistical Distribution of Wave Profiles

A wave elevation and slope grid can be created to compute the distribution function $f(\eta, \eta_x)$ from the two records of η and η_x as defined in equations (5.4) and (5.5), respectively. To minimize computation time, the grid is built around the values of elevation and slope of interest. Suppose the elevation-slope PDF for any given η, η_x profile of length I is represented by an M by N matrix(MxN): Let M be the number of elevation components, and N the number of slope components. All the possible elevations and slopes are grouped into M and N equal subsets, respectively.

$$Let \begin{cases} minM = min[\eta(i)], & maxM = max[\eta(i)] \\ minN = min[\eta_x(i)], & maxN = max[\eta_x(i)] \end{cases} \quad \forall\ i \in \{1, 2, 3, \ldots. I\} \tag{5.7}$$

Once the matrix size is given, the widths of the subsets are calculated using equation (5.8)

$$subwM = \frac{maxM - minM}{M} \qquad subwN = \frac{maxN - minN}{N} \tag{5.8}$$

Hence, the range of η and η_x are divided into M and N subsets of width $subwM$ and $subwN$, respectively. Each subset is called a "bin". The points that need to be evaluated are at the center of the bins. Let the first center value of the elevation component cM be $cM(1) = minM + subwM/2$, so that the second, $cM(2) = cM(1) + subwM$, and the third, $cM(3) = cM(2) + subwM$. In general,

$$cM(m) = cM(1) + (m-1) * subwM \qquad m = 2, 3 \ldots M \tag{5.9}$$

Similarly, the center slope components (cN) can be defined as

$$cN(n) = cN(1) + (n-1) * subwN \qquad n = 2, 3 \ldots N \tag{5.10}$$

Where $cN(1) = minN + subwN/2$ is the first center value of the slope component.

For all values of $\{\eta(i), \eta_x(i)\}$, a counter, $C(m,n)$, is built in the probability space so that

$$C(m,n) = C(m,n) + 1 \tag{5.11}$$

m and n are determined so that the distance between $\{\eta(i), \eta_x(i)\}$ and $\{cM(m), cN(n)\}$ is minimized. This happens when the point $\{\eta(i), \eta_x(i)\}$ is an element of the subset $\{m,n\}$. That is to say the $(\eta(i), \eta_x(i))$ pair falls in bin (m,n). The elevation-slope PDF, $f(\eta, \eta_x)$, is defined by the count divided by the total number of elements, I, in the sample space and binwidths $subwM$, and $subwN$

$$f(n,m) = f(\eta, \eta_x) = \frac{C(n,m)}{I * subwM * subwN} \tag{5.12}$$

The cumulative distribution function $F(n,m)$ is given by equation (5.13)

$$F(m,n) = \sum_{n=1}^{n \le N} \sum_{m=1}^{m \le M} f(m,n) * subwM * subwN \tag{5.13}$$

According to probability theory, the sum over all possible values of (m, n) should equal 1. Explicitly,

$$F(M,N) = \sum_{n=1}^{n=N} \sum_{m=1}^{m=M} f(m,n) * subwM * subwN = 1 \tag{5.14}$$

The density function for the nonlinear profile can be computed in the same manner by replacing $\{\eta(i), \eta_x(i)\}$ in equations (5.7 -5.14) by $\{\zeta(i), \zeta_x(i)\}$

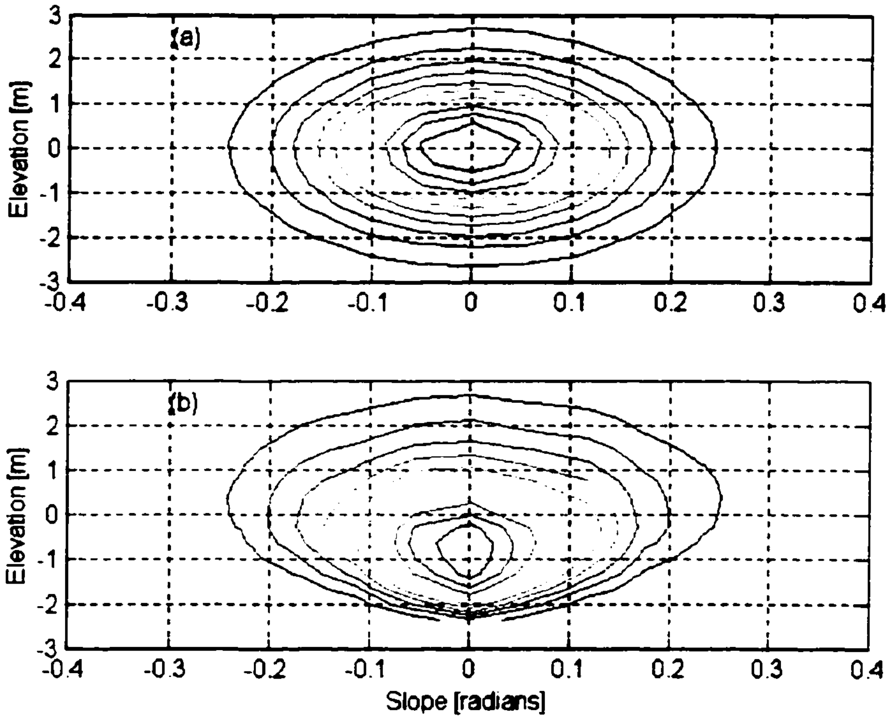

Figure 5.3 Contours of equal probability for the a) linear and b) nonlinear wave profile of figure 5.2. (*Jean-Pierre et al. (1999)*)

Equation (5.12) is simulated and the results are shown in figure 5.3. Since this is in 3 dimensional space, the PDFs are better viewed in a contour plot. Note that the distribution of elevation and slope for the linear simulation is symmetric about the $(\eta_x, \eta) = (0, 0)$. It forms a concentric ring which shows that: 1) the probability of negative elevation equals that of positive elevation with the same magnitude. And 2) the probability of negative slope equals that of positive slope with the same magnitude. However, the distribution for the nonlinear record has a deformed ellipsoidal shape. It shows that the slopes, ζ_x, are evenly distributed about zero with a high concentration around zero. The elevations, ζ, have an asymmetric distribution. One can argue that the elevation is Pearson distributed with the parameters equal to those used to generate the sequence. In this case, a skewness of 0.55 and a kurtosis of 3 were used. The mean value of both the elevation and slope should be zero. The standard deviation should agree with the value calculated from the power spectrum. This simulation was performed for a 10 km profile. A longer wave record and smaller binwidth for the PDF would result in a smoother distribution function. However, computation time would be longer. There is a trade-off between smoothness of the distribution and the length of time required to complete the computation. An analytical derivation of the elevation-slope PDF is sought and presented in section 5.4.

5.3 Wave Shadowing

Understanding the physics of microwave scattering from the ocean surface in the low grazing angle (LGA) regime is very important for shipboard radar tracking and surveillance. Optimal target detection requires knowledge of the statistics of the background clutter (noise). At moderate incidence angles, microwave scattering is reasonably well defined by composite surface theory (CST) where bragg-resonant capillary waves ride atop gently undulating long waves (see *Liu (1998), Wright (1968), Plant (1990)*). The general theory of electromagnetic scatter from the sea is well understood and is in good agreement with observations. It is comprehensively described in the literature such as *Beckmann and Spizichino (1963)*. However, scattering in the grazing angle regime has proved to be very difficult. The reasons will be discussed in the following sections.

5.3.1 Geometry of Shipboard Navigation Radar

A quick look at the geometry of a shipboard radar will reveal the difficulty in characterizing returns from a grazing angle incident beam. Consider a radar pulse from a geometrical optics standpoint. A transmitted radar pulse near the surface of the ocean reaches the water surface at a grazing angle. This angle would naturally decrease with range until it reaches zero at the radar's horizon. See figure 5.4. Let R be the effective radius of the earth so as to account for atmospheric refraction; D, be the range to the Horizon; Θ, the angle between the radar and the horizon at the center of the earth; d, the radar range from a point near the radar to D; θ, the angle at the center of the earth between zero and Θ; and δ, the grazing angle.

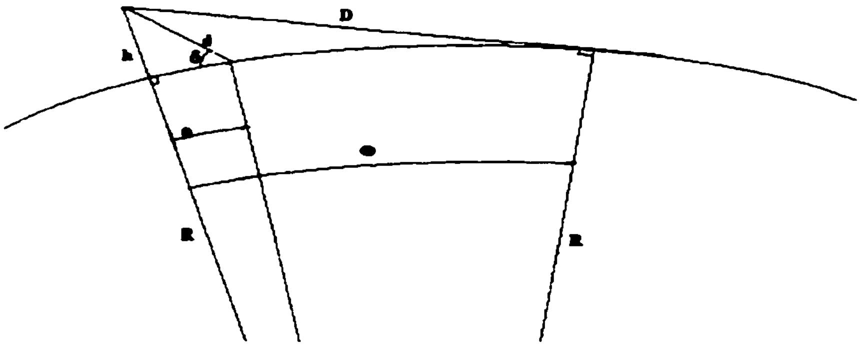

Figure 5.4 Schematic diagram of radar parameters (not to scale). The symbols define: radar height (h), grazing angle (δ) Earth radius (R), direct path from radar to ocean surface (d), range to horizon (D), angle at earth center when beam is at horizon (Θ). For h=30m; R=8488km; $D \simeq 22.57km$, $\Theta \simeq 2.66 * 10^{-3°}$.

The transmitted radar pulses are refracted based on the atmospheric conditions. For example, anomalous propagation can occur if the water vapor content in the air decreases rapidly with elevation. This would cause the radar waves to follow the curvature of the earth over large distances. For a representative condition, this effect can and has been approximated by multiplying the true radius of the earth by 4/3 (see *Long (1983)*).

The distance of the radar to the optical horizon can be calculated using the right triangle formula.

$$(R+h)^2 = R^2 + D^2 \tag{5.15}$$

which yields

$$D = (2R\,h + h^2)^{\frac{1}{2}} \tag{5.16}$$

The angle, Θ, between $R+h$ and R can be used for any given point on the sea between the optical horizon and the radar along with the law of cosines to calculate the range d. The result can in turn be used to calculate the grazing angle δ. Further simplification of the solution is obtained by using the first 3 terms of the Taylor series expansion to cosine.

$$d = \left[R^2 + (R+h)^2 - 2R\,(R+h)\cos(\theta)\right]^{\frac{1}{2}} \tag{5.17}$$

$$d = \left[h^2 + 2R(R+h)\left(\frac{\theta^2}{2} - \frac{\theta^4}{24}\right)\right]^{\frac{1}{2}}$$

The grazing angle, δ, can be approximated by assuming that the segment h is perpendicular to the ocean surface and that the surface is considered as a straight line. Therefore,

$$\delta = \sin^{-1}\left(\frac{h}{d}\right) \tag{5.18}$$

The errors in this assumption would increase with range as the surface becomes more curved. However, it can be neglected because the radars are normally at a very low elevation (20-60 m), and the radius of the earth is extremely large (8,488 km).

Figure 5.5 shows the graph of grazing angle as a function of range. The grazing angle decreases rapidly to below 0.5 degrees at just 5 km. The distribution of the portion of the waves as seen by a shipboard radar at these small angles will be investigated in section 5.3.3. The straight (dotted) line is the angle (*θ*) at the center of the earth divided by 600.

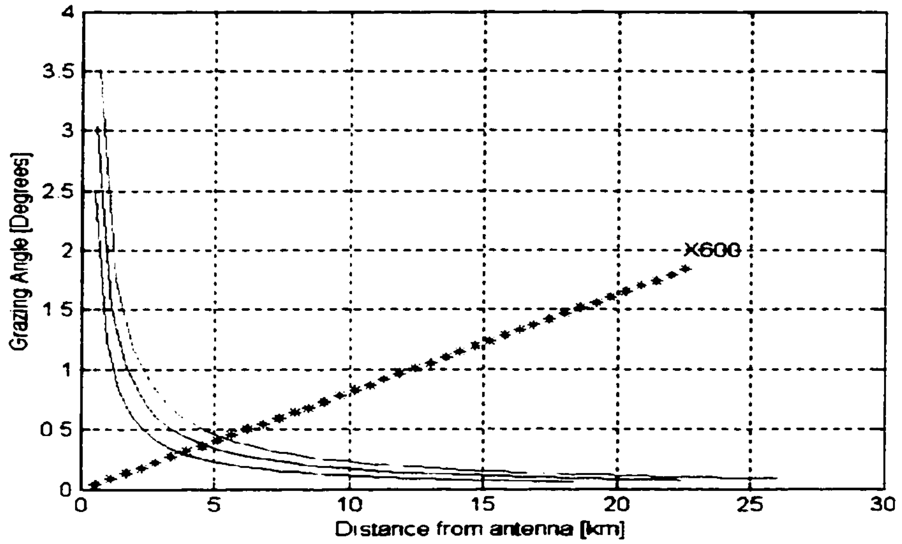

Figure 5.5 Grazing angle δ as a function of range (d) for antenna height (h) of 20, 30, 40 meters from left to right. Typically the grazing angle should be zero at the horizon. The difference in the graph is due to approximation error. The straight (dotted) line is the angle (θ) at the center of the earth divided by 600.

5.3.2 Radar Observations

The properties of figure 5.5 and figure 5.6a, b for the waves for the upwind, downwind direction that show those portions of the wavy surface illuminated by the radar beam make it possible to describe what will be seen on the radar screen when the radar is pointing either towards the oncoming waves or away from them. The shortest wavelength in these wave profiles corresponds to a wave with a period of 2 seconds, which is 6.25 meters in length. The roughness elements with shorter scales are what produce the backscatter from the illuminated portion of the wave profile.

The various measurements of the backscatter at low grazing angles need to be used along with information on the antenna pattern of the radar for both the vertical and horizontal dimensions to calculate the strength of the image on the radar screen. This will, of course, depend on the joint distribution of elevation and slope for those portions of the wavy surface that intercept the radar signal.

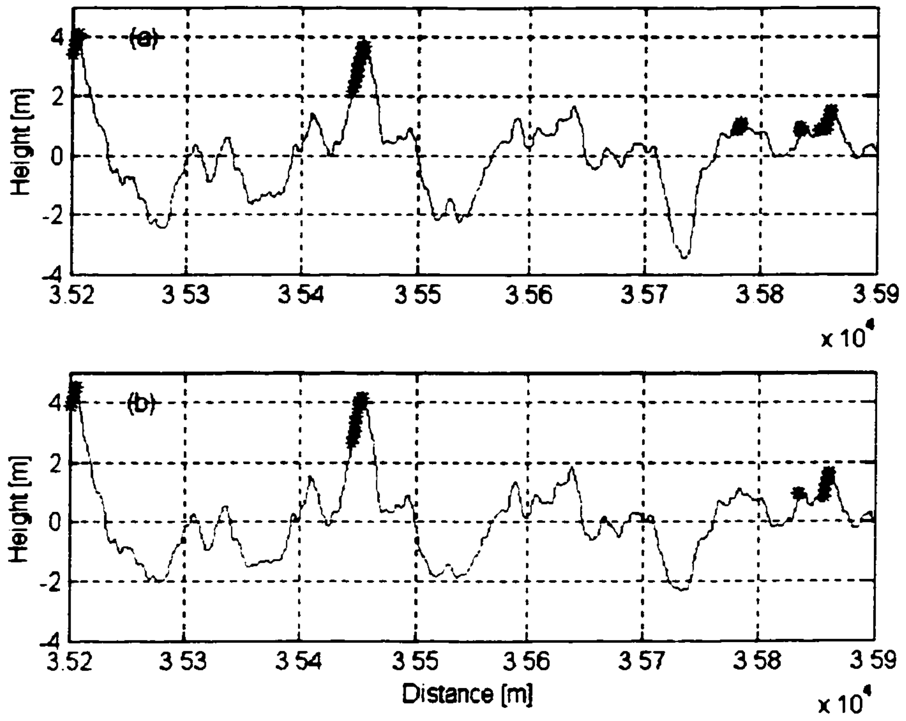

Figure 5.6 Section of a a) linear and b) Nonlinear wave profile. The * points indicates the portion of the wave surface illuminated by a shipboard radar at 0.5 degrees grazing angle.

As shown by figure 5.5 for a radar antenna at 30 meters above the ocean surface, the grazing angles decrease with increasing distance from the ship until the radar transmitted signal becomes parallel to the ocean surface as determined by the atmospheric refraction of the radar signal. Actually the effects of atmospheric refraction will vary from one time and place to another, However for this example the radius of the Earth has been increased by 4/3 to model this effect (*Long (1983)*) . The straight line denoted by the asterisks (*) is the angle θ, multiplied by 600, at the center of the earth as a function of distance. This gives you a relative magnitude of the two angles

δ and θ. There can be no backscatter from the waves at a distance beyond the radar horizon. However, objects such as land that project above the projection of the line, extending from the radar to the horizon will show up on the radar screen and outline the shores of the land.

Figure 5.6 shows an example of the illuminated portion of surface waves at 0.5 degree grazing angle. Out to a distance of about 1 km, the grazing angle is greater than 1 degree and a fairly large portion of the oncoming or outgoing waves will be illuminated by the radar. For the grazing angles less than 1 degree, a single high wave crest will shadow many of the waves behind it so that the radar screen will not show any waves.

This analysis explains the typical appearance of the radar screen for a navigation radar. The so-called sea clutter is concentrated within a relatively short distance from the ship's radar and quickly vanishes for typical wave conditions at longer ranges. Of course, much more still needs to be done to explain these radar observations. Nevertheless, this analysis is a modest but important step for the further analysis of the subject.

5.3.3 Effective Numerical Distributions

Most of the research done on LGA ocean scattering considers angles from 5-30 degrees (see the *"IEEE special issue on low grazing angle backscatter from rough surfaces" (1998)*). It is shown that scattering is much more pronounced at lower grazing angles. The work presented here is for grazing angles much smaller than the ones that have been considered in the past. A shadowing scheme was developed to determine what portion of the waves will be illuminated at a given grazing angle. As shown by figure 5.5, the grazing angle decreases with increasing distance away from the ship. For illustrative purposes, a constant grazing angle is used to define the distribution at any given angle. This is done by choosing the starred (*) points that would be illuminated and creating a two-dimensional probability distribution as in section 5.2.1.

Figure 5.6 shows the portion of the wave that would be illuminated by an 0.5 degree grazing angle for linear and nonlinear waves, respectively. Notice how the crest around $3.578 * 10^4$ m is illuminated in the linear record and not illuminated in the nonlinear record. This is a direct result of the nonlinear transformation with the Pearson distribution. The crest at $3.545 * 10^4$ m for the nonlinear record has been raised higher than the one at $3.578 * 10^4$ m. The effect will be more pronounced at lower grazing angles. This is the portion that is visible to the radar on the left side of the profile. All the starred points of figure 5.6 are selected and the procedure developed for equation (5.12) is used to compute the elevation-slope PDF. The result is the PDF for the illuminated portion of figure 5.6 given by figure 5.7. From the observer's point of view (ship antenna), the visible elevations would be positive as shown by figure 5.7. A majority of the slopes would be positive and zero; with very few negative slope values (± 0.05 radians). Figure 5.7a for the linear record comprises of 8900 points compared to 7450 points for the nonlinear record. That is 8.9% and 7.45% of the original 100,000 points distribution of figure 5.3. Therefore, an additional effect of the nonlinear transformation is that fewer points are visible for any given grazing angle. An incoming target will be able to see the other side of the profile, which may not have the same characteristics. In fact, from the target point of view, a majority of the visible portion will have negative slope.

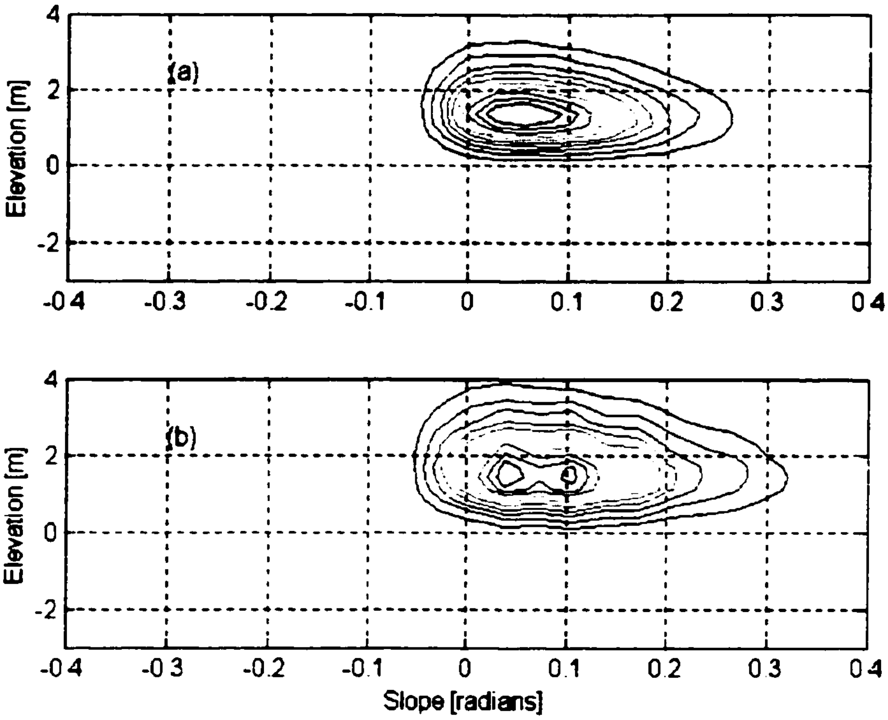

Figure 5.7 Conditional illumination probability at 0.5 degree grazing angle. These are the contours of equal probability for the illuminated surface of figure 5.6. Contours (a) and (b) are for the linear and nonlinear simulation, respectively.

As it will be of interest to know the effective probability of waves involved in the scattering and reflecting of radar radiation, the probability that will be seen by both source and target is computed. Figure 5.8(a-h) shows the elevation slope PDF for the portion of the waves illuminated at 0.05, 0.2, 0.5 and 0.7 degrees for both the linear and nonlinear simulations as seen by both a radar on a ship and an incoming target. This could also be done for different grazing angles from both perspective. However, it was not done here. In any case, the figures show that the higher crests and slopes around zero are responsible for radar wave scattering. For a given grazing angle, the visible heights for the nonlinear record are higher than those for the linear record. For instance, the visible heights for the linear record with 0.5 degree grazing angle range from 0.7 to 3.4 m while the nonlinear record range from 1.0 to 3.9 m. The slope component remains within ±0.05 radians.

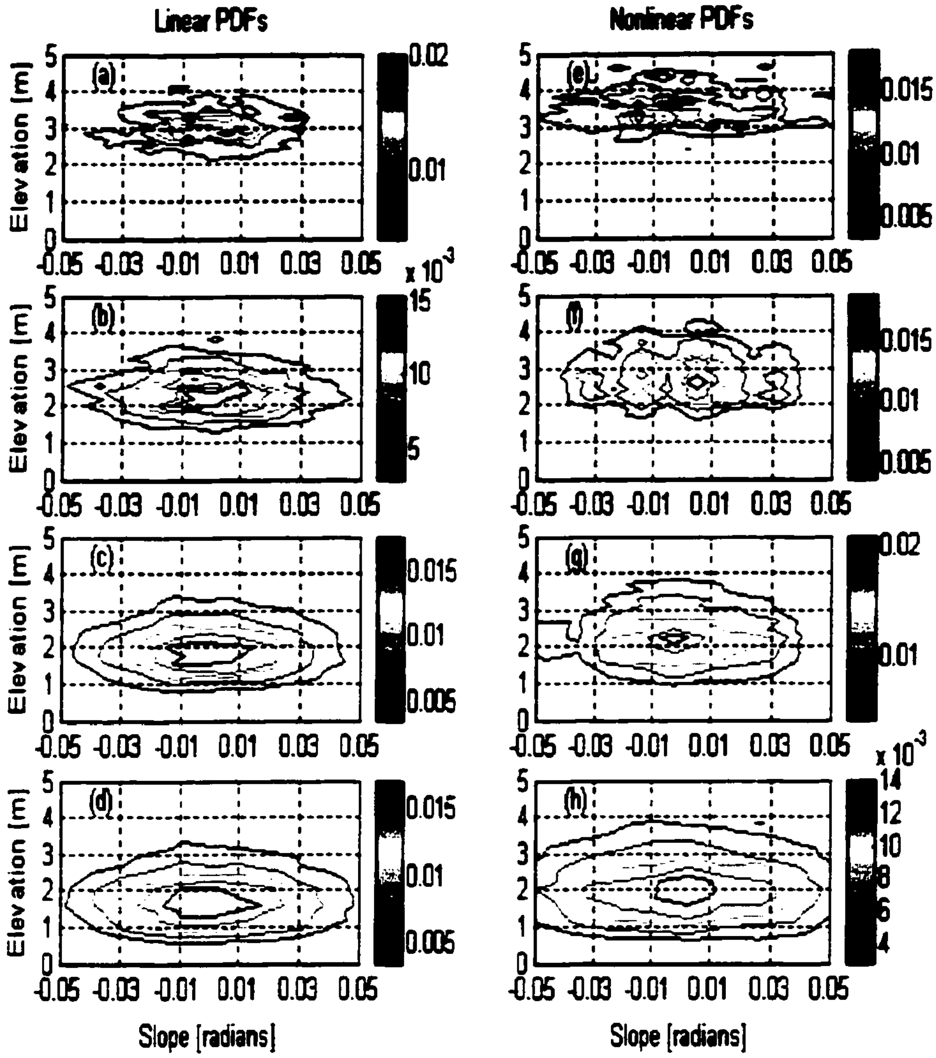

Figure 5.8 Contours of equal probability for the portion of the waves illuminated at 0.05, 0.2. 0.5 and 0.7 degrees for both the linear (a, b, c, d) and nonlinear (e, f, g, h) wave profile. This is the portion that would be visible to both a shipboard radar and an incoming target.

In this section, the ocean probability density function was defined numerically and from that a method to extract the conditional probability of the waves illuminated at any given angle was developed. It will also be useful to be able to define the probabilities analytically. This is the approach taken in the next section.

5.4 Analytical Representation of Sea Surface Wave Statistics

The Fleet Numerical Meteorology and Oceanography Center in Monterey disseminates predictions of sea state over most of the world's oceans at periodic intervals of time. These predictions are in the form of the frequency-direction spectrum of the waves, for discrete bands of frequency and direction. These wave spectra frequently represent a local wind generated sea and components of swell that have propagated into the area. The total spectrum often covers directions for the waves for a full 360°. *Gerling (1991)* has analyzed the various component of the wave spectra obtained during the Labrador Sea Extreme Waves EXperiment (LEWEX) and shown that the individual contributions of four different wave systems that were measured. Problems requiring the joint statistics of sea-surface elevation and slope components cannot be determined directly from these spectra without hydrodynamic theory or other assumptions. Often, the Gaussian assumption is made, under which the joint PDF of elevation and slope components is easily determined. But this assumption violates the known and observed characteristics of the sea surface.

In section 3.2.3, a method for obtaining a better approximation of the elevation statistics was proposed. The plan here is to represent the transformation analytically. Let η be the surface elevation obtained from linear Gaussian theory, and ζ the "non-linearized" surface elevation intended to be a better approximation to the true sea surface. Moreover, assume that the two are related by the transformation functions ψ and ϕ as in equation (5.19)

$$\zeta = \psi(\eta), \quad \text{and} \quad \eta = \phi(\zeta) \tag{5.19}$$

The functions ψ and ϕ are monotonic and are inverses of each other. This follows from the way in which they are determined. The assumption is that η is Gaussian, and ζ is distributed according to a specified PDF, which is taken to be one of the

Pearson functions. Then the functions ψ and ϕ are determined by matching the two cumulative distributions.

Even if this technique is valid for the elevation, there is no assurance that it will work for the multivariate elevation-slope PDF. In fact, it is obvious that it may not. One of the prominent features of nonlinear surface waves is that their phase speed is greater than would be inferred from linear theory. For a periodic nonlinear Stokes wave, *Drennan (1988)* has shown that the highest possible Stokes wave has a phase speed that is about 5 percent greater than that for a linear solution. It might be useful to decrease the wavenumbers in this model by multiplying them by a number between 0.95 and 1.00. Even though this and perhaps other important features are neglected, the present method (section 3.2.3) provides one improvement in the statistics of the sea surface that may have some application.

In the Gaussian assumption a simple way to determine this joint PDF from the frequency-direction spectrum $S(\omega,\theta)$ is to transform it to a wavenumber direction spectrum which is given by equation (5.20)

$$S(k,\theta) = S(k)F(k,\theta) \tag{5.20}$$

$$F(k,\theta) = A[\cos(\frac{\theta}{2})]^{p(k)} \tag{5.21}$$

where $S(k)$ is given by equation (5.1) and $F(k,\theta)$ by (5.21) . It is possible to calculate the variances and covariances by the series of equations of (5.22). When transformed to a wavenumber direction spectrum, the coefficient A is chosen so that the integral over direction of equation (5.21) is equal to one. $p(k)$ is a simple function that makes the peak of the spectrum narrower. When the slopes are evaluated, the integral over direction yields weights for the wavenumber spectrum for the moments. However, the PM spectrum is not correct for high wavenumbers because surface tension and other effects result in a different spectrum for the capillary waves as in *Donelan and Pierson (1987)* . When $S(k)$ is multiplied by k^2, the integral over k has a logarithmic singularity and the numerical value of the integral depends on the choice of a cut-off wavenumber defined by k_c. The value corresponds to a wavelength of 6.25 meters for the simulations given in the previous sections. The elevation and slope statistics are defined by equation (5.22)

$$
\begin{aligned}
\sigma^2 &= \langle \eta^2 \rangle = \frac{1}{2}\int_0^{k_c}\int_{-\pi}^{\pi} S(k,\theta)d\theta dk \\
\sigma_x^2 &= \langle \eta_x^2 \rangle = \int_0^{k_c}\int_{-\pi}^{\pi} k^2 S(k,\theta)\cos^2\theta \, d\theta dk \\
\sigma_{xy} &= \langle \eta_x \eta_y \rangle = \int_0^{k_c}\int_{-\pi}^{\pi} k \; S(k,\theta)\sin\theta \cos\theta d\theta dk \\
\sigma_y^2 &= \langle \eta_y^2 \rangle = \int_0^{k_c}\int_{-\pi}^{\pi} k^2 S(k,\theta)\sin^2\theta \, d\theta dk
\end{aligned}
\tag{5.22}
$$

thereby defining σ, σ_x, σ_y, and σ_{xy}, where the angle brackets indicate expected values. σ is the variance of η; σ_x, σ_y, the variance of the slope of η in the x-direction (η_x) and y-direction (η_y), respectively; σ_{xy}, the covariance of the slopes of η. These can be computed by an average at a single time over a sufficiently large area of the (x, y) plane, or over a sufficiently large period of time at a single point assuming stationarity. In addition, the correlation coefficient ρ is given by equation (5.23).

$$
\rho = \frac{\sigma_{xy}}{\sigma_x \sigma_y} \tag{5.23}
$$

For this example the elevation is independent of the slope components. The Covariance Matrix (Σ), its inverse (Σ^{-1}) and the determinant are given by equations (5.24-26)

$$
\Sigma = \begin{pmatrix} \sigma^2 & 0 & 0 \\ 0 & \sigma_x^2 & \sigma_{xy} \\ 0 & \sigma_{xy} & \sigma_y^2 \end{pmatrix} \tag{5.24}
$$

$$
\Sigma^{-1} = Q^{-1}\begin{pmatrix} Q\sigma^{-2} & 0 & 0 \\ 0 & \sigma_y^2 & -\sigma_{xy} \\ 0 & -\sigma_{xy} & \sigma_x^2 \end{pmatrix} \tag{5.25}
$$

$$
\det(\Sigma) = Q\sigma^2 \tag{5.26}
$$

where Q is defined by $Q = \sigma_x^2\sigma_y^2 - \sigma_{xy}^2$. The joint PDF of elevation and slope components under this Gaussian assumption is given by

$$\begin{aligned} p_{\eta xy}(\eta,\eta_x,\eta_y) &= \frac{1}{\sqrt{(2\pi)^3\det(\Sigma)}}\exp\left(-\tfrac{1}{2}X^T\Sigma^{-1}X\right) \\ &= \frac{1}{\sigma\sigma_x\sigma_y\sqrt{(2\pi)^3(1-\rho^2)}}\exp\left[-\frac{\eta^2}{2\sigma^2}-\frac{1}{2(1-\rho^2)}\left(\frac{\eta_x^2}{\sigma_x^2}-\frac{2\rho\eta_x\eta_y}{\sigma_x\sigma_y}+\frac{\eta_y^2}{\sigma_y^2}\right)\right] \end{aligned} \tag{5.27}$$

where

$$X = \{\eta \quad \eta_x \quad \eta_y\}^T \tag{5.28}$$

Equation (5.27) is a very special result for the multivariate PDF of a linear representation of the sea. Each of the variables has a marginal PDF defined from $-\infty$ to ∞ for a linear model.

The joint PDF of ζ, ζ_x, and ζ_y based on the transformation (5.19) might be transformed by the following steps. If this method can be applied at a single point, to get $\zeta(x)$ in terms of $\eta(x)$, it can be applied at neighboring points to relate the slope components of ζ to those of η. The usual method of transformation of variates is applied. The new distribution is defined in the multidimensional space of interest by equation (5.29)

$$f(\zeta,\zeta_x,\zeta_y) = \sum \frac{f(\eta,\eta_x,\eta_y)}{\|J(\zeta,\zeta_x,\zeta_y)\|} \quad \Big|_{\eta=\phi(\zeta)} \tag{5.29}$$

$\|J(\zeta,\zeta_x,\zeta_y)\|$ is the determinant of the Jacobian matrix. The Jacobian of the transformation is seen to be

$$J(\zeta,\zeta_x,\zeta_y) = \frac{\partial(\zeta,\zeta_x,\zeta_y)}{\partial(\eta,\eta_x,\eta_y)} = \begin{pmatrix} \psi'(\eta) & 0 & 0 \\ \psi''(\eta)\eta_x & \psi'(\eta) & 0 \\ \psi''(\eta)\eta_y & 0 & \psi'(\eta) \end{pmatrix} \tag{5.30}$$

whose determinant is $\psi'(\eta)^3 = \phi'(\zeta)^{-3}$. The proof is given in Appendix A. The PDF of the new variates is then

$$\begin{aligned} p_{\zeta xy}(\zeta,\zeta_x,\zeta_y) &= \frac{\phi'(\zeta)^3}{\sqrt{(2\pi)^3\det(\Sigma)}}\exp\left(-\tfrac{1}{2}Y^T\Sigma^{-1}Y\right) \\ &= \frac{\phi'(\zeta)^3}{\sigma\sigma_x\sigma_y\sqrt{(2\pi)^3(1-\rho^2)}}\exp\left[-\frac{\phi^2(\zeta)}{2\sigma^2}-\frac{\phi'(\zeta)^2}{2(1-\rho^2)}\left(\frac{\zeta_x^2}{\sigma_x^2}-\frac{2\rho\zeta_x\zeta_y}{\sigma_x\sigma_y}+\frac{\zeta_y^2}{\sigma_y^2}\right)\right] \end{aligned} \tag{5.31}$$

where $Y = X$ is expressed in terms of the new variates as in equation (5.32)

$$Y = \{\phi(\zeta) \quad \phi'(\zeta)\zeta_x \quad \phi'(\zeta)\zeta_y\}^T \tag{5.32}$$

A development of these equations are given in Appendix A. Those interested in the theory of transformation of variables are encouraged to review any book in higher level probability theory. The references *Papoulis (1991)* chapter 6 and *Anderson(1971)* are recommended.

For a specified elevation η or ζ the transformation of the slope components is assumed to be linear, as seen by comparing (5.28) with (5.32), and the PDF (5.31) is Gaussian in the new slope components. The means of the nonlinearized slope components $\langle\zeta_x\rangle$ and $\langle\zeta_y\rangle$ are zero, and their covariance matrix is

$$\begin{pmatrix} \langle\zeta_x^2\rangle & \langle\zeta_x\zeta_y\rangle \\ \langle\zeta_x\zeta_y\rangle & \langle\zeta_y^2\rangle \end{pmatrix} = \psi'(\eta)^2 \begin{pmatrix} \sigma_x^2 & \sigma_{xy} \\ \sigma_{xy} & \sigma_y^2 \end{pmatrix} \tag{5.33}$$

To find the univariate PDF of elevation, the marginal version of (5.31) can be found by integrating out the slope components, or more simply by direct transformation of the elevation. The PDF of the two representations of elevation are

$$p_\eta(\eta) = \frac{1}{\sigma\sqrt{2\pi}}\exp\left(-\frac{\eta^2}{2\sigma^2}\right) \tag{5.34}$$

$$p_\zeta(\zeta) = \frac{\phi'(\zeta)}{\sigma\sqrt{2\pi}}\exp\left(-\frac{\phi(\zeta)^2}{2\sigma^2}\right) \tag{5.35}$$

It is evident that the PDF of ζ is not Gaussian in general. Its mean value and higher order moments are given by equations (5.36) and (5.37). The important differences between $p_\eta(\eta)$ and $p_\zeta(\zeta)$ is the function $\phi'(\zeta)$. This function modulates the Gaussian PDF and transforms it to a Pearson PDF by setting the Normal PDF equal to zero outside the range from r_1 to r_2 as defined in section 3.2.2. It also modulates the shape of the Normal curve so as to introduce the skewness and kurtosis and forces the Normal curve to zero at r_1 and r_2.

$$\bar{\zeta} = \frac{1}{\sigma\sqrt{2\pi}}\int_{-\infty}^{\infty}\psi(\eta)\exp\left(-\frac{\eta^2}{2\sigma^2}\right)d\eta \tag{5.36}$$

$$\langle(\zeta-\bar{\zeta})^n\rangle = \frac{1}{\sigma\sqrt{2\pi}}\int_{-\infty}^{\infty}[\psi(\eta)-\bar{\zeta}]^n\exp\left(-\frac{\eta^2}{2\sigma^2}\right)d\eta \tag{5.37}$$

According to section 3.2.3 the transformation (5.19) is determined in order to obtain a desired PDF of the nonlinearized surface elevation ζ. The function ϕ can be determined by integrating equation (5.35),

$$\int_{-\infty}^{\zeta} p_\zeta(\tilde{\zeta})d\tilde{\zeta} = \frac{1}{\sigma\sqrt{2\pi}}\int_{-\infty}^{\phi(\zeta)} \exp\left(-\frac{\tilde{\eta}^2}{2\sigma^2}\right) d\tilde{\eta} \tag{5.38}$$

and substituting $\tilde{\eta}$ for $\phi(\tilde{\zeta})$ in (5.35). Again, realize that $\partial\zeta = \phi'(\zeta)^{(-1)}\partial\eta$ from Appendix A2. Equation (5.38) verified that the analytical method corresponds to the numerical method. Recall that the cumulative distributions were used to transform η to ζ. For any given value $\eta(i)$, $\zeta(i)$ was found by equating their respective cumulative distributions according to the schematic of figure 3.19. In other words,

$$\int_{-\infty}^{\zeta} p_\zeta(\zeta)\ d\zeta = \int_{-\infty}^{\eta} p_\eta(\eta)\ d\eta \tag{5.39}$$

The integral of equation (5.38) can be expressed in terms of the error function giving

$$\phi(\zeta) = \sigma\sqrt{2}\Theta\left(2\int_{-\infty}^{\zeta} p_\zeta(\tilde{\zeta})d\tilde{\zeta} - 1\right) \tag{5.40}$$

where the function Θ is the inverse of the error function. That is, $w = \operatorname{erf}(z) \iff z = \Theta(w)$. The derivation can be found in Appendix A2.IV. If the slope components are not normally distributed, $\phi'(\zeta)$ will need to be $\phi'(\zeta, \zeta_x, \zeta_y)$ and (5.35) becomes a function of all three variables.

Equation (5.1) must be multiplied by an angular spreading function, $F(k, \theta)$. For simplicity this can be an even function of θ. Simply changing θ to $\theta + \varphi$, where φ is any arbitrary angle, changes the result completely. The change represents pointing the radar in a different direction relative to the orientation of the waves. For the previous example, the slopes need to be measured in a coordinate system for which x is the direction corresponding to $\theta = 0$.

For this special case, the correlation between wave elevation, η, and wave slope, η_x is zero. For each value of η, on one side of a wave there will usually be a positive slope and on the other side a negative slope so that over the entire wave surface, $\eta(x, y)$, the opposing slopes cancel. Thus if $F(k,\theta)$ is as defined in (5.21), the correlation coefficient for the wave elevation and wave slope in the x-direction will be zero.

The difficulty, even for a linear model, is that the radar cannot illuminate both the front and the back of the same wave. If $F(k,\theta)$ is as defined above, the slopes in the y-direction could possibly be neglected and equation (5.27), for the linear PDF, would simplify to a bivariate distribution by integrating over η_y. Since the elevation and slope in the x-direction are uncorrelated, equation (5.27) simplifies to the PDF of two independent variables. It is defined by the product of the PDF of elevation and the slope in the form given by equation (5.41).

$$p(\eta,\eta_x) = \frac{1}{2\pi\sigma\sigma_x}\exp\left[-\left(\frac{\eta^2}{2\sigma^2}+\frac{\eta_x^2}{2\sigma_x^2}\right)\right] \tag{5.41}$$

Evidently, the two-dimensional PDF for the nonlinear waves can be computed from equation (5.41) the same way (5.31) was computed from (5.27). The Jacobian matrix here is the top left 2x2 matrix of (5.30). Its determinant is $\|J(\zeta,\zeta_x)\| = \psi'(\eta)^{(2)} = \phi'(\zeta)^{(-2)}$ and $f(\zeta,\zeta_x)$ is given by equation (5.42)

$$p(\zeta,\zeta_x) = \frac{\phi'(\zeta)^{(2)}}{2\pi\sigma\sigma_x}\exp\left[-\left(\frac{\zeta^2}{2\sigma^2}+\frac{\phi'(\zeta)^{(2)}\zeta_x^2}{2\sigma_x^2}\right)\right] \tag{5.42}$$

The contours of equal probability for the linear elevation-slope PDf in (5.41) are ellipses centered at the origin as shown in figure 5.9a. The contours for the nonlinear case, equation (5.42), in figure 5.9b are skewed. When figure 5.3 and figure 5.9 are compared, they seem to have the same characteristics except that the contours of figure 5.9 are much smoother. This is due to the fact that the numerical computation is limited by the step size of the variables. It is computationally intensive. The step size depends on the number of bins used to divide the total range of elevation and slope values. As indicated by equation (5.8), the larger the number of bins (M,N), the smaller is the step size or "binwidth". Twenty bins (M=20) for the elevation component and twenty-two bins (N=22) for slope component were used to compute the contours of figure 5.3. For example, if M=N=30 bins were used, the smoothness of the resulting PDF would more closely match that of figure 5.9. However, it would take longer to complete the computations. All in all, the two figures show that the two methods provide similar results.

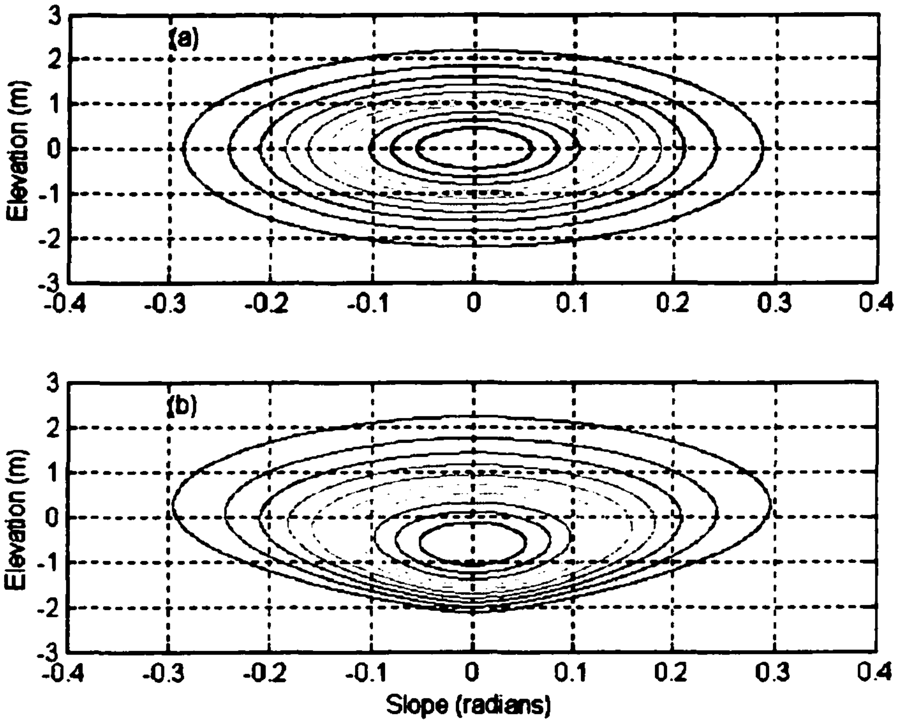

Figure 5.9 Contours of equal probability for the analytical calculation of a) equation (5.41) for a linear and b) equation (5.42) for a nonlinear wave profile.

From equation (5.41) that part of the waves illuminated by the radar can be approximated by requiring that η be greater than η_1 and that the slopes be greater than zero. The probability that this will happen is given approximately by equation (5.43).

$$p(\eta > \eta_1, \eta_x > 0) = \int_{\eta_1}^{\infty} \int_{0}^{\infty} p(\eta, \eta_x) d\eta_x d\eta \qquad (5.43)$$

The probability density function for those parts of the waves greater than η_1 and their associated positive slopes is the conditional PDF

$$p(\eta, \eta_x : \eta > \eta_1, \eta_x > 0) = \begin{cases} p(\eta, \eta_x) & \mathit{for} \ \ \eta > \eta_1, \eta_x > 0 \\ 0 & \mathit{Otherwise} \end{cases} \qquad (5.44)$$

which needs to be divided by the numerical value of equation (5.43) so that the area under the modified PDF is one. Similar considerations can be made to obtain the conditional probabilities of equation (5.42). The most general case for equation (5.27) requires that the values for all the elements in equations (5.24-26)be computed from the spectrum.

When fully evaluated, equation (5.27) can be applied to the problem of describing the radar backscatter measured for much higher grazing angles, or the complement incidence angles measured by spacecraft such as NSCAT. For these angles, the entire sea surface is illuminated by the radar and there is no shadowing effect. The two scale backscatter model used by ***Donelan and Pierson (1987)*** could be improved, even without nonlinear considerations, by the use of this model.

It is desirable to be able to transform the multivariate PDF given by (5.27) and its necessary extensions to a multivariate PDF for a model of nonlinear waves as represented by $\zeta(x,y)$. The resulting PDF for the wavy surface will usually be some form of the Pearson type-I PDF defined by the standard deviation, σ, the skewness, μ_3, and perhaps, the kurtosis μ_4 of the data. The Normal PDF for $\eta(x,y)$ will be the Pearson PDF for $\zeta(x,y)$, and it will have a finite range of values from r_1 to r_2 as defined by (5.3).

Not much is known about the slopes of a nonlinear wave form from observations and even less is known about the correlations between elevation and wave slope. The marginal distribution for ζ_x and ζ_y will be needed as a start. ***Huang (1986)*** has provided data on the wave slope PDF as part of the analysis of the TOWARD program. The waves were quite low. It was found that ζ_x was not normally distributed and had a negative value for the skewness whereas ζ_y was nearly normally distributed. The joint PDF for ζ_x and ζ_y was also shown for measurements such that the dominant wave direction did not correspond to the wind direction.

5.5 Application to Radar Sea Scattering

Microwave scattering from the sea surface is affected by the shape of the surface. The statistics of this scattering are determined by the surface elevation-slope PDF discussed in previous sections. *Zavorotny and Voronovich (1998)* show that in a two component sea surface, the scattering of microwaves is affected by the shape of the smooth component. In the greatly simplified problem of scatter defined by *Groves and Chow (1998)* as being radially symmetric about the specular direction, in which the scattered intensity depends only on the Specular Deviation Angle (SDA), the statistics of the scattered waves are determined by the elevation-slope PDF of the smooth component. In particular, it is the PDF of only that portion of the sea surface that is visible from both the radar antenna and target. Representative distributions are shown in figure 5.8(a-h) for different grazing angles. They are the conditional distribution of equation (5.44) and its corresponding transformation. These distributions can be used to characterize the EM reflection or diffusive properties of ocean surface waves.

The problem of tracking a low-flying target involves small grazing angles. Consequently, the phenomenon of shadowing becomes important. Numerical simulation has shown that the effect of shadowing from a real sea surface differs greatly from that of a linear Gaussian sea surface having the same frequency direction spectrum.

Since there is no known simple way to evaluate the shadowing effect, this always required numerical simulation using a stochastically-generated sea profile. One reason the Gaussian assumption is so popular is that it is straightforward to get the elevation-slope statistics from the frequency-direction ocean wave spectrum. There has not yet been developed a straightforward way to obtain this statistical information for a real sea surface having a given spectrum. One way to accomplish this is to use a simple nonlinearization scheme as defined in section 3.2.3. It would be greatly desirable to check the validity of this procedure by obtaining real sea-surface statistics, or by developing nonlinearization methods of higher fidelity.

5.6 Profile Summary and Discussion

Two different ways to investigate the effects of waves on tracking an Anti-Ship Cruise Missile have been described for greatly oversimplified conditions. One way is to Monte Carlo both a linear and a nonlinear representation of the waves and to evaluate the slopes and elevations of the resulting surfaces for those regions illuminated by the radar at low grazing angles. The other way is to find the multivariate PDF for the elevation and slope of that surface and compute the required statistics for those regions in the three dimensional probability space that is illuminated by the radar. The two methods are complementary and need to be pursued in parallel.

Ultimately, both methods need to be extended to more realistic conditions. The two dimensional surfaces given by $\eta(x,y)$ and its nonlinear representation $\zeta(x,y)$ need to be generated, and the resulting slopes $\eta_x(x,y)$ and $\zeta_x(x,y)$ along with appropriate covariance and correlation coefficients need to be evaluated so as to determine the radar behavior for a range of low grazing angles.

Also when the radar signal reflects off the wavy surface and continues on in the same direction toward a target missile, the bistatic radar measurements where a signal is transmitted by one radar and received by a receiver at some point down range needs to be modeled. The slight difference in travel time between the direct ray and the forward scattered ray when the transmitted radar signal returns to the radar are what undoubtedly confuse the interpretation of the measurements. Something similar to the work of *Broschat (1993)* needs to be done.

The available literature on radar returns for low grazing angles is notably lacking a description of the properties of the ocean waves. With no information on the wave spectrum and other necessary properties of the waves and parameters of the measurements, the return signals can not be characterized adequately. Future experiments will need to be more carefully designed. It is suggested that the method herein is a first step into describing the realistic properties of the waves.

Chapter 6

6.0 Potential Application of the Nonlinear Method for Radar Altimetry

Radar altimetry has been used to measure the range from the ocean surface to a satellite. Advances of accurate Global Positioning Systems (GPS) and measurement of marine geoid has allowed very accurate measurement of the ocean surface. An altimeter is basically a microwave instrument that sends a radar pulse from an orbiting satellite; the pulse scatters and reflects off the earths surface, and returns to the orbiting spacecraft. The travel time of this pulse (the time it takes to get to the surface of the Earth and return to the satellite) is then recorded. Thus the distance is related to the time the pulse has traveled. The altimeter range measurement and corrections are shown schematically in figure 6.1. This diagram is taken from *Zieger et al., 1991*.

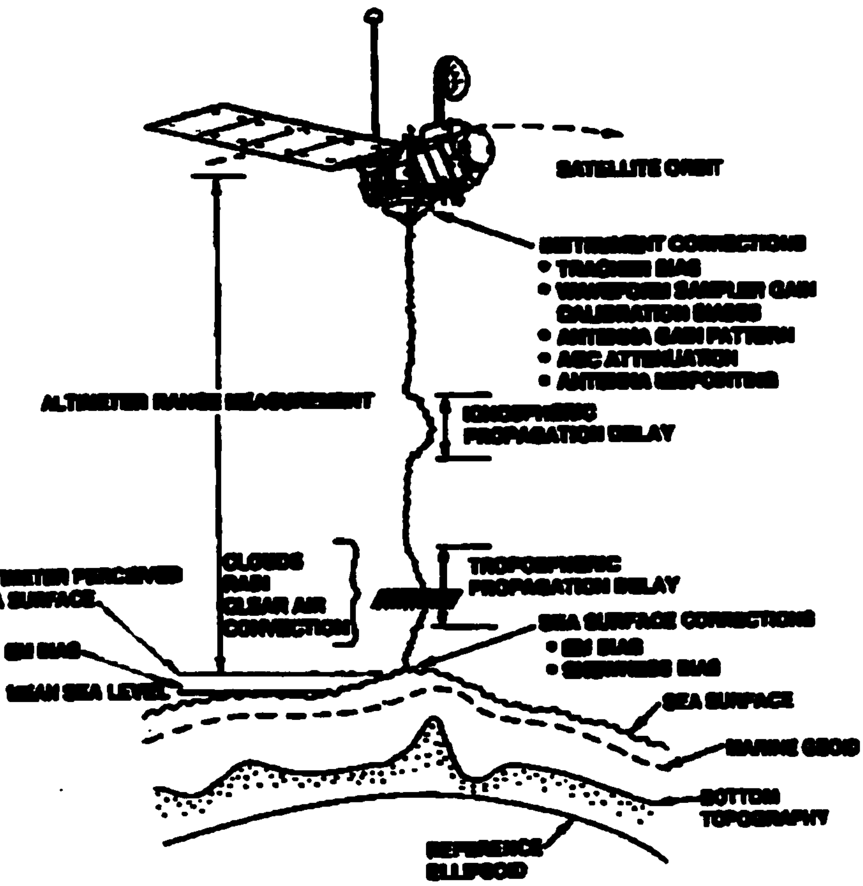

Figure 6.1 The altimeter range measurement and corrections are illustrated schematically to show the geometry of the measurement. (*Zieger et al. (1991)*)

The farther away an object is the longer it takes that pulse to return. Therefore, as the ground or sea surface to spacecraft distance changes so does the travel time. This is the same concept used in certain airplane altimeters and radars. The physics of altimetric measurements is nothing new, but its application to oceanography began a revolution and oceanography has never been the same.

There are many reasons why the height of the ocean is not level. There are seamounts and trenches which change the gravitational pull on the ocean surface and thus the height. There is the moon and sun pulling on the ocean surface that causes the tides. There are tremendous ocean currents, such as the Gulf Stream, which can cause a 1 meter change in the height of the ocean between the US East Coast and Bermuda. There are winds which cause waves and also force ocean currents. There is the sun heating the ocean, which causes it to expand. There are atmospheric storms which change the pressure on the ocean surface. All of these things change the ocean surface by a different amount. By far the gravitational pull is the greatest amount (100 meters). However, the heating of the ocean surface (30-100 centimeters) and how the atmosphere and ocean react to that was for the first time measured by TOPEX/Poseidon. These measurements permitted, for the first time, the observation of El Niño. Although this might seem a small amount, the climatic changes worldwide can be catastrophic.

The first experimental altimeter was flown on Skylab. However, its use for oceanography was very limited because its accuracy was not adequate for ocean wave height measurements. In general, the waves in the ocean are only a few meters high, and the now world famous El Niño changes the level of the ocean by only 30 centimeters. The Skylab altimeter was more a "proof of concept" instrument that lead the way to the more modern radar altimeters.

The first true oceanographic altimetric mission occurred with SEASAT in 1978. The SEASAT radar altimeter was a remarkable instrument in many ways, yielding a variety of informations on geophysical phenomena such as sea surface topography, wave heights, and wind speed. Although the satellite failed in approximately 3 months after its launch in June of 1978, it succeeded in proving that modern microwave sensors deployed from a polar-orbiting satellite can provide very accurate data on sea surface conditions. Its usefulness is seen in application for weather forecasting, ship routing, offshore operations, and in the longer term for air-sea interaction and climate studies.

The success of altimeter measurements from SEASAT opened a new era of ocean topography missions. From SEASAT, to GEOSAT, ERS-1, Topex/Poseidon and beginning in 2001 Jason-1, the range accuracy requirements has increased from 10cm to 1cm (*Zieger et. al (1991)*). With this required accuracy, any small improvement in processing will be noticeable. Jason-1 is a direct descendent of the Topex/Poseidon altimeter. There are many improvements in the system that enabled such a high accuracy. The primary goal of the Topex/Poseidon mission was to increase understanding of the global ocean dynamics. The sensors payload had several improvements over previous missions. The altimeter design was upgraded to a dual frequency instrument (5.3 and 13.6GHz) to provide path delay corrections for ionospheric effects in the radar beam. The altimeter antenna diameter was increased from 1 meter (SEASAT and GEOSAT) to 1.5 meter. This allows a stronger signal-to-Noise ratio at the higher altitude of 1336km compared to 800km (SEASAT and GEOSAT) and 784km (ERS1 and ERS2) (*Quartly et al (2001)*). At the higher altitude, where atmospheric drag is greatly reduced, the precision orbit is more easily maintained. The microwave radiometer has fixed pointing in the nadir direction which provide an increased integration interval in the vertical.

A close look at the altimeter tracking algorithm (*Hayne et al (1994), Rodriguez (1988), Zieger et al. (1991)*) shows that there are adjustments that could be made to meet the 1cm requirement for the Jason-1 mission. The work of *Brown (1977)* and *Rodriguez (1988)* demonstrated that the average power return from a rough surface for near-normal incidences, ($W(t)$), could be expressed as a convolution of: 1) The Flat sea impulse response function, $P_{FS}(t)$, including radar antenna beam width and pointing angle effects. 2) The Radar observed surface elevation probability density function, $q_s(t)$, and 3) the radar altimeter point target response, $p_r(t)$.

$$W(t) = P_{FS}(t) \circledast p_r(t) \circledast q_s(t) \tag{6.1}$$

The flat sea impulse response is a ramp function lasting for the duration of the pulse length. Figure 6.2 represents the return power in the absence of waves. As the waves increase in magnitude (the roughness element), the return signal would smear over a longer duration as the transmitted pulse reflects from different facets of the surface waves. The reference (*Quartly, Srokosz et al., (2001) p.2087*) has a representative figure that shows the wave height and return signal variations. Hence, the slope of the ramp reflects the amplitude of the ocean surface waves.

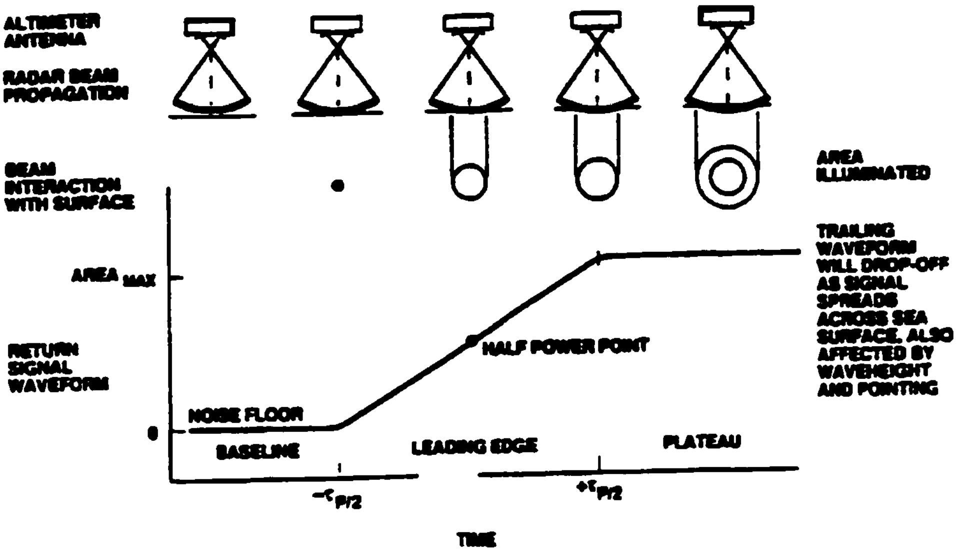

Figure 6.2 Altimeter pulse interaction with the sea surface and the characteristic return waveform generated by the altimeter electronics. (*Zieger et al. (1991)*)

The flat sea impulse response function is given by

$$P_{FS}(t) = A_o \exp(-\delta t) I_0(\beta t^{\frac{1}{2}}) U(t) \tag{6.2}$$

and it contains information about the antenna beamwidth and pointing angle. See *Zieger et al. (1991)* and *Rodriguez (1988)* for more detailed descriptions of these parameters. The altimeter point-target response is the effective transmitted pulse shape as observed by the receiver. It has a theoretical shape of a sinc squared function. When fitting actual radar altimeter data, the sampled data from one of the altimeter's calibration mode is used. The theoretical approximation is given by

$$P_\tau(t) \simeq \frac{sin^2(\frac{at}{2}(T - |t|))}{(\frac{at}{2})^2} \qquad -T \leq t \leq T \tag{6.3}$$

where $2T$ is the radar pulse length (3.125 ns for Topex) and a is a constant which depends on the radar beamwidth (*Rodriguez, (1988)*). The specular point PDF is given by

$$q_s = \frac{1}{\sigma_s\sqrt{2\pi}}\, e^{-\frac{t^2}{2\sigma_s^2}}\{1 + \frac{\lambda_s}{6}[(\frac{t}{\sigma_s})^3 - 3(\frac{t}{\sigma_s})]\} \tag{6.4}$$

where λ_s is the skewness parameter, σ_s is the surface rms elevation in ranging-time unit. This is a form of the Longuet-Higgins equation (*Longuet-Higgins, (1963)*).

To convert from the time to space domain Rodriguez and Chapman (*Rodriguez (1988); Rodriguez and Chapman, (1989)*) use $t = -\frac{2z}{c}$, $\sigma_s = \frac{2\sigma}{c}$ and represent the specular point PDF by

$$f_{sp}(\eta) = \frac{1}{\sigma\sqrt{2\pi}}\, e^{-\frac{\eta^2}{2}}\{1 + \frac{\mu_3}{6}[\eta^3 - 3\eta]\} \tag{6.5}$$

where $\eta = \frac{z - z_T}{\sigma}$. μ_3 is the ocean surface skewness (assumed to be 0.1 - *Zieger et al. (1991), Rodriguez and Chapman (1989), Hayne et al. (1994)*). z is the height above the mean ocean surface and z_T, the tracker bias, represents the shift of the altimeter track point with respect to the mean electromagnetic surface. Remember that the analysis of laboratory and field data presented in this dissertation showed that the skewness values vary from -0.1 to as high as 0.53. This is where the algorithm presented can be used to improve wave height estimates derived from altimeter measurements.

Rodriguez (*Rodriguez et al. (1989)*) showed a deconvolution algorithm to extract wave height information from the returned signal. From equation (6.1), knowing the flat sea impulse response, equation (6.2), and the point target response, equation (6.3), they showed different methods to estimate the parameters of the specular point PDF (equation (6.5)). One of the methods is to think of equation (6.1) as a matrix equation

$$y = Mx \tag{6.6}$$

where y is the return power, M is the convolution $P_{FS}(t) \circledast p_T(t)$, and x is the specular point PDF. As shown in *Rodriguez et al. (1989)*, there are many algorithms that can be used to solve the matrix equation.

Once the wave heights have been determined from the matrix solution, the method presented in chapter 3 can be used to add corrections so that the wave heights fit the Pearson type distribution. Instead of using the normal and the Pearson cumulative distribution function(CDF) as in figure 3.19, one would use a representative Longuet-Higgins (equation (6.5)) and a Pearson CDF. There is a dilemma. The Longuet-Higgins(LH) PDF becomes negative for that negative value of η where the cubic polynomial in the square bracket is zero.

Figure 6.3 shows a set of graphs of equation (6.5) for the skewness values of 0, 0.1, 0.2, 0.4, 0.5, and 0.6. The graph with zero skewness is essentially the normal PDF.

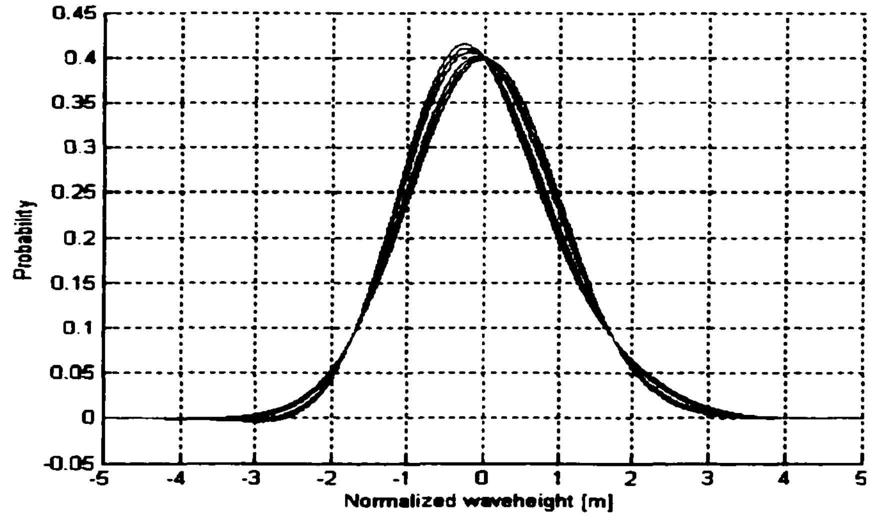

Figure 6.3 The Longuet-Higgins probability density function for skewness values of 0, 0.1, 0.2, 0.4, 0.5 and 0.6. Read from right to legt at the 0.3 probability level.

There are important differences between the LH PDF and the Pearson family of probability density functions. In figure 6.3, all of the curves cross at $\eta = -\sqrt{3}$ and $\eta = +\sqrt{3}$. They become negative at η equals to - 4.170, -3.430, -2.870, -2.722 and -2.614 for μ_3 equal 0.1, 0.2, 0.4, 0.5 and 0.6 respectively. See figure 6.4 and figure

6.5 for greater details. These points are the results, equation (6.8), of the zeroes of the cubic polynomial of equation (6.5) for the corresponding skewness values. The negative values for the PDF below these points are undesired because they do not fit the fundamental properties of a probability density function. Furthermore, if the integral over all possible values ($-\infty < \eta < \infty$) of the LH PDF equals to 1, then the integral over the positive values would be greater than one. Thus, truncating the negative values still does not solve the problem.

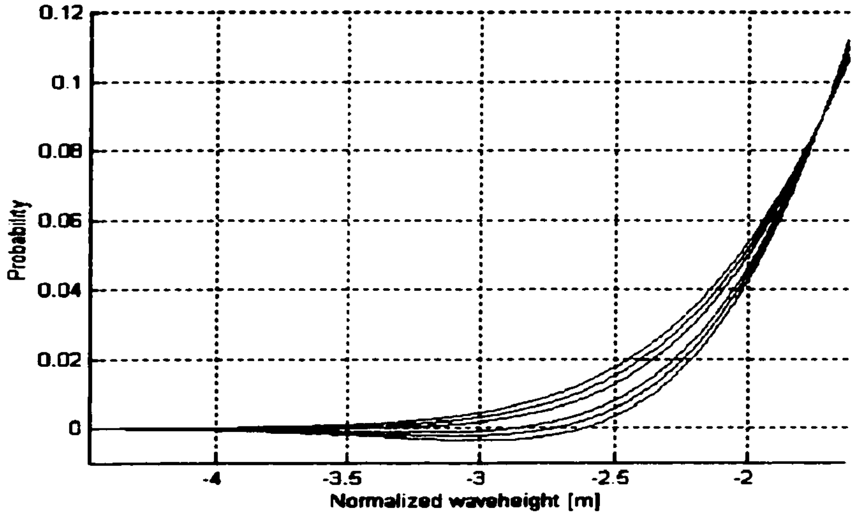

Figure 6.4 The tail of figure 6.3 showing negative values for the PDF .

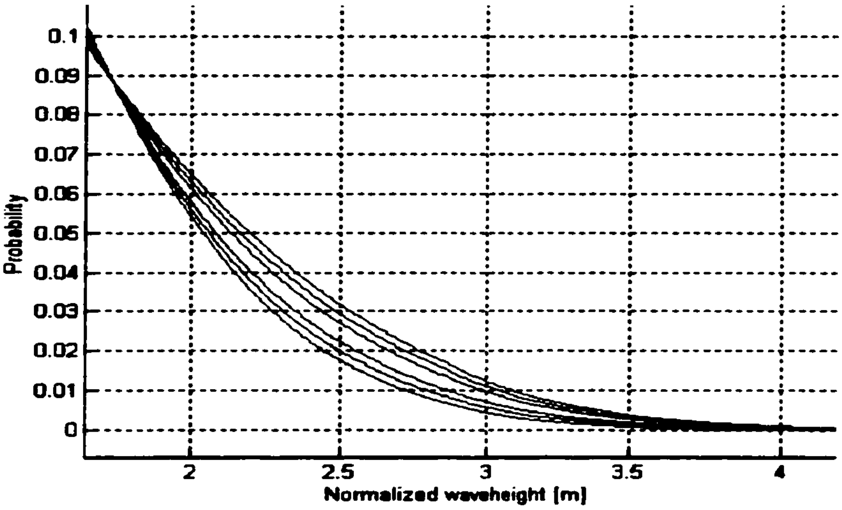

Figure 6.5 The tail of figure 6.3 for higher wave heights.

One way to solve the problem is to find the solution for the zeroes of the cubic polynomial of equation (6.5). The polynomial equation has 2 complex conjugate solutions, equation (6.7) and (6.9), and 1 real solution, equation (6.8)

$$\eta_{o1} = \frac{\alpha}{\mu_3}\left[(1+(\frac{\mu_3}{\alpha})^2)\right] \tag{6.7}$$

$$\eta_o = \eta_{o2} = -\frac{\alpha}{2\mu_3}\left[(1+(\frac{\mu_3}{\alpha})^2) - i\sqrt{3}(1-(\frac{\mu_3}{\alpha})^2)\right] \tag{6.8}$$

$$\eta_{o3} = -\frac{\alpha}{2\mu_3}\left[(1+(\frac{\mu_3}{\alpha})^2) + i\sqrt{3}(1-(\frac{\mu_3}{\alpha})^2)\right] \tag{6.9}$$

$$\alpha = \left[\mu_3^2(\sqrt{9-\mu_3^2}-3)\right]^{1/3} \tag{6.10}$$

Since the integral of equation (6.5) over all possible values $(-\infty < \eta < \infty)$ is equal to 1, the integral over $(\eta_o \leq \eta < \infty)$, when the negative values are omitted, would be greater than 1. Thus

$$\int_{\eta_o}^{\infty} f_{sp}(\eta)\, d\eta = 1 + \varepsilon \tag{6.11}$$

The way to proceed is to find the corresponding ε value and modify the PDF so that the integral over ($\eta_o \leq \eta < \infty$) equals to 1. When equation (6.11) is solved for ε, the functional form is given by equation (6.12). Figure 6.6 shows the plot of ε versus Skewness. Note that ε is a function of μ_3. It increases with increasing skewness. This represents the area enclosed by the negative portion of the PDF that must be corrected. For $\mu_3 = 0.1$, $\varepsilon = 3.024e^{-6}$, however for $\mu_3 = 0.5$, $\varepsilon = 2e^{-3}$.

$$\varepsilon = \frac{1}{2\sigma}[1 - erf(\frac{\sqrt{2}}{2}\eta_o)] + \frac{\mu_3}{6\sigma\sqrt{2\pi}}\, e^{-\frac{\eta_o^2}{2}}\, (\eta_o^2 - 1) - 1 \tag{6.12}$$

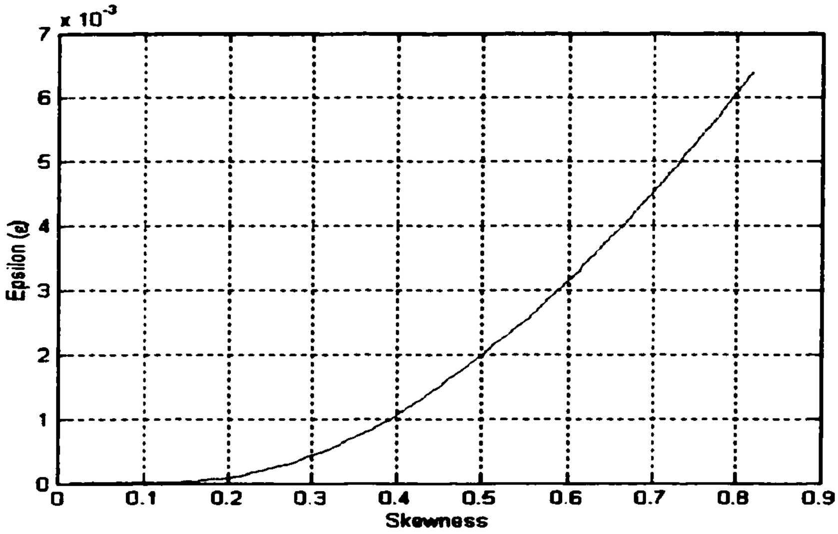

Figure 6.6 The normalising constant for the Longuet-Higgins probability density function as a function of skewness ($\sigma = 1$).

The modified specular point PDF, f_{sp}^{*}, is represented by equation (6.13). The first and second moments were computed over the restricted limits and they are given by equations (6.14) and (6.15). The characteristic values for the moments are shown in figure 6.7.

$$f_{sp}^{*} = \frac{f_{sp}(\eta)}{1+\varepsilon} \qquad \eta_o \leq \eta < \infty \tag{6.13}$$

$$m_1 = \frac{1}{\sigma\sqrt{2\pi}}\, e^{-\frac{\eta_o^2}{2}}\left(1 + \frac{\mu_3 \eta_o^3}{6}\right) \tag{6.14}$$

$$m_2 = \frac{1}{\sigma\sqrt{2\pi}}\, \left[\frac{\sqrt{2\pi}}{2} + \frac{\sqrt{2\pi}}{2}\, erf\left(\frac{\sqrt{2}}{2}\eta_o\right) + e^{-\frac{\eta_o^2}{2}}\left(\frac{\mu_3}{3} + \eta_o + \frac{\mu_3 \eta_o^2}{6} + \frac{\mu_3 \eta_o^4}{6}\right)\right] \tag{6.15}$$

Once modified, the resulting CDF can be used with the Normal CDF to perform the wave height corrections similar to the method presented in chapter 3. This modified PDF is presented as an alternate PDF which can be tested for "goodness of fit" to actual ocean waves. If the first moment was strictly zero, then the variance would equal to the second moment. However, as shown in figure 6.7, the first moment is a function of the skewness values. For very low skewness ($\mu_2 < 0.1$), equation (6.13) is a good representation of a PDF. For higher skewness values, one would need to develop new methods to correct for the skewness variations.

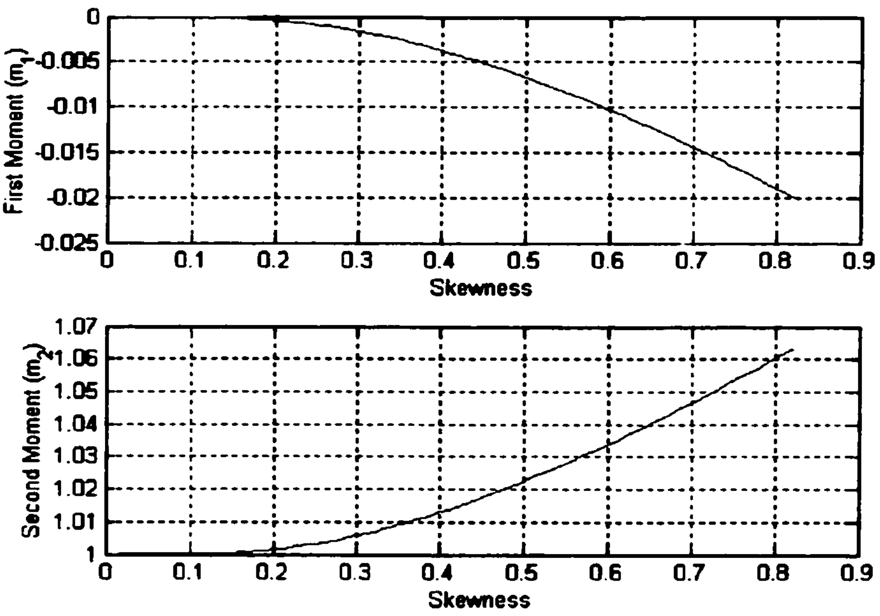

Figure 6.7 Characteristic values for the first(top curve) and the 2nd (bottom curve) moments of the modified LH-PDF as a function of skewness ($\sigma = 1$).

Two major conclusions from this analysis are: 1) that the negative values under the LH PDF for the assumed 0.1 skewness is negligible as $\epsilon(3.024e^{-6})$ is approximately zero and the first and second moments are approximately 0 and 1, respectively, in that region; and 2) that the above method to correct for the negative values will not work for higher skewness values as the first and second moments depend on higher order statistics as shown in figure 6.7.

Hayne, et al. (1994) describe the use of equation (6.5) in the tracking algorithm for TOPEX Poseidon. They argue that only one skewness value, namely 0.1, should be used because "the small wave shape features from the TOPEX altimeter's digital filter bank – jeopardize attempts to make reasonable skewness estimates –" (Page 24, 943). In a personal communication with Dr. Hayne, he stated: " I remember that at the time there was considerable discussion about what skewness value to use, and that finally Bob Stewart, who was the Topex Project Scientist at the time, simply announced that we would assume 0.1 surface skewness everywhere." (*personal communication, George Hayne, August 2002, NASA GSFC/WFF*). The time he is referring to is during the implementation phase of the Topex altimeter design.

Clearly there is room for improvement for altimeter algorithms such as in the proper treatment of skewness. Perhaps, a relationship can be found between wind speed and skewness. Then from the method presented in chapter 3, the right corrections for altimeter measurements can be found. Given an accurate wind speed, the correction is obtained by using the CDF for the assumed skewness, 0.1, and the CDF for the corresponding skewness value for that wind speed. The wind speed and skewness relationship may take years of experiments and research. Therefore, this will be open for further studies.

Chapter 7

7.0 Conclusion and Further Research

A Monte Carlo method for simulating nonlinear ocean surface wave records was described. The method used the Pierson-Moskowitz spectrum to simulate the linear solution of the hydrodynamic equations. The nonlinear effects were introduced using a Type-I Pearson probability distribution function. The derived method can not model breaking waves. The Monte Carlo simulation is nevertheless a way to obtain a more realistic representation of the waves without having to solve the extremely complicated hydrodynamic equations.

In order to show the validity of the method, insitu data from a buoy, a wavestaff and a laser system were analysed. As it is well known in the field of oceanography, buoy data do not contain the nonlinear properties of the waves. The skewness values that were found in wavestaff and laser data were not present in the buoy data. The standard deviations for the laser data were slightly higher than those for the buoy data. The skewness values for the buoy data were near zero and those for the wavestaff and laser system were consistently positive. The spectra of wavestaff data for various skewnesses were studied. It was discovered that the spectra did not tell anything about the nonlinear properties of the waves. Rather, they retained the variance information. Statistical comparisons were made between the simulated nonlinear wave records and actual wave records. The results showed that the simulated nonlinear records had properties that were similar to records that could have been recorded by a wavestaff or a laser system.

One thousand 30-minute nonlinear wave records were simulated for a skewness of 0.55 and a wind speed of 15 m/s. They were analysed for sampling variability. The results were within the limits predicted by *Donelan and Pierson (1983)*.

The importance of an accurate nonlinear model for remote sensing applications was shown. Wave profiles as a function of distance along a line were simulated. A method was developed to define a two-dimensional(2D) PDF of wave elevation and slope numerically. In order to understand the portion of the waves that are involved in radar wave scattering at low grazing angles, the geometry of the system was defined. 2D conditional PDFs were derived to define the effective PDF of elevation and slope for any given grazing angle. These probabilities will eventually be needed to define distributions of the specular deviation angle. An analytical derivation of the method was sought to produce 2D analytical PDFs. Both numerical and analytical methods produced similar results. Ultimately, both methods need to be extended to more realistic conditions. The two dimensional surfaces given by $\eta(x,y)$ and its nonlinear representation $\zeta(x,y)$ need to be generated, and the resulting slopes $\eta_x(x,y)$ and $\zeta_x(x,y)$ along with appropriate covariance and correlation coefficients need to be evaluated so as to determine the radar behavior for a range of low grazing angles. Three-dimensional(3D) PDFs as in $p_{\zeta xy}(\zeta,\zeta_x,\zeta_y)$ will be needed.

Deficiencies in the method to extract wave heights from the Topex/Poseidon altimeter were shown. The assumed 0.1 skewness along with the Longuet-Higgins PDF used in the altimeter algorithm was found to be inadequate to represent the many different skewness values measured in actual data. An attempt to correct for the deficiencies was made but was unsuccessful. However, the analysis provided some very interesting results that could be pursued in further studies. An alternate procedure using the Pearson PDF and the method developed in chapter 3 of this dissertation was suggested.

Srokosz (*Srokosz, (1998)*) suggested that the Pearson Type-I PDF is valid for skewnesses up to the critical value of 0.826490. It would be very interesting to compare the simulated nonlinear records for skewness values over the range from 0 to perhaps 0.8 with data measured from a laser or a wavestaff with similar statistics (ie. STD, skewness, and kurtosis).

To fully describe the properties of waves, η needs to be defined as a function of x, y, t as in equation (7.1).

$$\eta(x,y,t) = \sum_{i=1}^{I}\sum_{j=1}^{J} a_{ij}\cos\left[k_i\left(x\cos\theta_j + y\sin\theta_j\right) - w_i t + \varepsilon_{ij}\right] \tag{7.1}$$

$$S(w,\theta) = S(w)F(w,\theta) \tag{7.2}$$

$$a_{ij} = \sqrt{2S(w_i,\theta_j)\Delta w\Delta\theta} \tag{7.3}$$

Then, a transformation similar to the method in section 3.2 would need to be performed to obtain the nonlinear records ($\zeta(x,y,t)$). The quantities a_{ij}, $\Delta w, \Delta\theta$ are to be determined by quantizing a given directional spectrum $S(w,\theta)$ (7.2) into I and J subinterval. ε_{ij} are randomly distributed phases from 0 to 2π. $S(w)$ is as defined in section (3.1), and $F(w,\theta)$, to be determined, is the directional spreading function. This much more complicated problem will be a topic for further studies.

Appendix A

This section provides some of the missing links in the formulas given in this paper. Since these information are unique to the definition of equation (5.19) and its application, they may not be found in any other book. It is hoped that these derivations make this thesis easier to read.

A1: Converting the Pearson Distribution, f_p, to a More Well Known Beta Distribution

In order to make the Pearson distribution look more familiar and easier to work with, it is required that the function undergoes a series of change of variables. Remember that the Pearson probability function was not used directly. The cumulative distribution was used in all the analyses. From equation (3.21) and (3.22), the Pearson Cumulative distribution can be written as

$$F_B = \frac{1}{B(a,b)} \int_0^y x^{m_1}(1-x)^{m_2}\, dx \tag{A1.1}$$

Where the subscript B signifies the Beta version of the Pearson distribution. $m_1 = a - 1$

and $m_2 = b - 1$. By definition, the Beta function is given by equation (A1.2)

$$B(a,b) = \frac{\Gamma(a)\Gamma(b)}{\Gamma(a+b)} \qquad (A1.2)$$

The Gamma function is defined in equation (3.18). Equation (3.11) can be used to rewrite the equation for the Pearson cumulative distribution in (A1.3)

$$F_p(y) = \int_{-\infty}^{y} f_p(x)\,dx \qquad (A1.3)$$

$$F_p(y) = C_p \int_{r_1}^{y} (x - r_1)^{m_1}(r_2 - x)^{m_2}\,dx \qquad \text{for } r_1 \le y \le r_2$$

let $w = x - r_1$ then $dx = dw$ and the limit changes accordingly

$$= C_p \int_0^{y-r_1} w^{m_1}(r_2 - r_1 - w)^{m_2}\,dw$$

$$= C_p \int_0^{y-r_1} w^{m_1}(r_2 - r_1)^{m_2}(1 - \frac{w}{(r_2 - r_1)})^{m_2}\,dw$$

let $z = \frac{w}{r_2 - r_1}$ then $dw = (r_2 - r_1)dz$

Substitute the values for w and the corresponding limits.

$$= C_p \int_0^{\frac{y-r_1}{r_2-r_1}} [(r_2 - r_1)z]^{m_1}(r_2 - r_1)^{m_2}(1 - z)^{m_2}[(r_2 - r_1)dz]$$

$$= C_p(r_2 - r_1)^{m_2+m_1+1} \int_0^{\frac{y-r_1}{r_2-r_1}} z^{m_1}(1 - z)^{m_2}dz$$

Compare the equation (3.17) for C_p and equation (A1.2) for $B(a,b)$ and make the appropriate substitution in the equation above. The result is

$$F_p(y) = \frac{1}{B(m_1 + 1, m_2 + 1)} \int_0^{\frac{y-r_1}{r_2-r_1}} z^{m_1}(1 - z)^{m_2}dx \qquad (A1.4)$$

Thus equation(A1.4) defines the Pearson cumulative distribution function in terms of the Beta distribution. Note also that the values y varies from r_1 to r_2. Therefore the limit for the integration varies from 0 to 1. This integration again is a special form of the Beta function.

A2: Supporting Formulas for the Analytical Derivation of the Nonlinear Transformation.

In support to the many abridged formulas in Chapter 5, the simplified terms of those equations are provided. In many cases the final results will not be repeated for the reader is referred to specific equation numbers.

A2.I The Jacobian of the Transformation Matrix

Since the distribution for η is known (Gaussian), another to find the distribution of ζ, the Jacobian matrix, $J(\zeta, \zeta_x, \zeta_y)$, of equation (5.19) is needed. The distribution of ζ is defined by equation (5.29) and the result is equation (5.31). From equation (5.30) the Jacobian matrix is

$$J(\zeta, \zeta_x, \zeta_y) = \frac{\partial(\zeta, \zeta_x, \zeta_y)}{\partial(\eta, \eta_x, \eta_y)} = \begin{bmatrix} \frac{\partial\zeta}{\partial\eta} & \frac{\partial\zeta}{\partial\eta_x} & \frac{\partial\zeta}{\partial\eta_y} \\ \frac{\partial\zeta_x}{\partial\eta} & \frac{\partial\zeta_x}{\partial\eta_x} & \frac{\partial\zeta_x}{\partial\eta_y} \\ \frac{\partial\zeta_y}{\partial\eta} & \frac{\partial\zeta_y}{\partial\eta_x} & \frac{\partial\zeta_y}{\partial\eta_y} \end{bmatrix} \qquad (A2.1)$$

Each element of the matrix will be defined separately. The following definitions for ζ_x and ζ_y will be needed.

$$\zeta_x = \frac{\partial\zeta}{\partial x} = \frac{\partial\zeta}{\partial\eta}\,\frac{\partial\eta}{\partial x} = \psi'(\eta)\eta_x \qquad (A2.2)$$

Similarly,

$$\zeta_y = \frac{\partial\zeta}{\partial y} = \frac{\partial\zeta}{\partial\eta}\,\frac{\partial\eta}{\partial y} = \psi'(\eta)\eta_y \qquad (A2.3)$$

$$\begin{array}{ccc} \frac{\partial\zeta}{\partial\eta} = \psi'(\eta) & \frac{\partial\zeta}{\partial\eta_x} = 0 & \frac{\partial\zeta}{\partial\eta_y} = 0 \\ \frac{\partial\zeta_x}{\partial\eta} = \psi''(\eta)\eta_x & \frac{\partial\zeta_x}{\partial\eta_x} = \psi'(\eta) & \frac{\partial\zeta_x}{\partial\eta_y} = 0 \\ \frac{\partial\zeta_y}{\partial\eta} = \psi''(\eta)\eta_y & \frac{\partial\zeta_y}{\partial\eta_x} = 0 & \frac{\partial\zeta_y}{\partial\eta_y} = \psi'(\eta) \end{array} \qquad (A2.4)$$

These partial derivatives are written explicitly to verify the results of equation (5.30). After substituting the values of (A2.4) into (A2.1), the Jacobian matrix, $J(\zeta, \zeta_x, \zeta_y)$, turn out to be a triangular matrix. Its determinant, $\|J(\zeta, \zeta_x, \zeta_y)\|$, is $\psi'(\eta)^{(3)}$.

A2.II Proof: $\psi'(\eta) = \phi'(\zeta)^{(-1)}$

Analytical representation of the nonlinear transformation started with the definition of $\zeta = \psi(\eta)$ and $\eta = \phi(\zeta)$ in equation (5.19). By using the chain rule, the derivatives ζ_x and η_x are given by (A2.5) and (A2.6), respectively.

$$\frac{\partial\zeta}{\partial x} = \frac{\partial\psi}{\partial\eta} * \frac{\partial\eta}{\partial x} \qquad (A2.5)$$

$$\frac{\partial\eta}{\partial x} = \frac{\partial\phi}{\partial\zeta} * \frac{\partial\zeta}{\partial x} \qquad (A2.6)$$

Rewriting equation (A2.5) and substituting the value for (A2.6) results in

$$\frac{\partial\zeta}{\partial x} = \frac{\partial\psi}{\partial\eta} * \frac{\partial\phi}{\partial\zeta} * \frac{\partial\zeta}{\partial x}$$

Therefore

$$\frac{\partial\psi}{\partial\eta} * \frac{\partial\phi}{\partial\zeta} = 1 \qquad (A2.7)$$

Thus $\psi'(\eta) = \phi'(\zeta)^{(-1)}$.

A2.III Details of the Analytical Derivation of the 3-D Pearson Distribution Function

The final result of equation (5.31) can be obtained from equations (5.27) and (5.29) by direct substitution. Recall that $\|J(\zeta, \zeta_x, \zeta_y)\| = \phi'(\zeta)^{(-3)}$. From (5.27)

$$p_{\eta xy}(\eta, \eta_x, \eta_y) = \frac{1}{\sigma\sigma_x\sigma_y\sqrt{(2\pi)^3(1-\rho^2)}}\exp\left[-\frac{\eta^2}{2\sigma^2} - \frac{1}{2(1-\rho^2)}\left(\frac{\eta_x^2}{\sigma_x^2} - \frac{2\rho\eta_x\eta_y}{\sigma_x\sigma_y} + \frac{\eta_y^2}{\sigma_y^2}\right)\right] \qquad (A2.8)$$

The values for $\eta = \phi(\zeta)$, $\eta_x = \phi'(\zeta)\zeta_x$, as obtained from equation (A2.6), and subsequently $\eta_y = \phi'(\zeta)\zeta_y$ needs to be substituted in (A2.8). Therefore,

$$\begin{aligned} p_{\zeta xy}(\zeta, \zeta_x, \zeta_y) &= \frac{f(\eta, \eta_x, \eta_y)}{\|J(\zeta, \zeta_x, \zeta_y)\|} \quad \Big|_{\eta=\phi(\zeta)} \\ &= \frac{\phi'(\zeta)^{(3)}}{\sigma\sigma_x\sigma_y\sqrt{(2\pi)^3(1-\rho^2)}}\exp\left[-\frac{\phi(\zeta)^2}{2\sigma^2} - \frac{\phi'(\zeta)^{(2)}}{2(1-\rho^2)}\left(\frac{\zeta_x^2}{\sigma_x^2} - \frac{2\rho\zeta_x\zeta_y}{\sigma_x\sigma_y} + \frac{\zeta_y^2}{\sigma_y^2}\right)\right] \end{aligned} \qquad (A2.9)$$

The matrix multiplication in the exponent of equation (5.31), $(-\frac{1}{2}Y^T\Sigma^{-1}Y)$, is left for the reader to verify that it results in the same solution as that of the exponent of (A2.9). Also, calculation of the 1D and 2D PDFs are left to the reader. In each case, the Jacobian would be a subset of the 3D Jacobian matrix.

A2.IV Determination of the Function $\phi(\zeta)$

This function is used in all the nonlinear distributions. It is important that $\phi(\zeta)$ be represented by an analytical expression. Again, the fact that these supporting equations are unique to the definitions of η and ζ and will not be found anywhere else in the literature, they are given here in details. From equation (5.38), the Pearson Cumulative Distribution is given by

$$\int_{-\infty}^{\zeta} p_\zeta(\tilde{\zeta})d\tilde{\zeta} = \frac{1}{\sigma\sqrt{2\pi}}\int_{-\infty}^{\phi(\zeta)} \exp\left(-\frac{\tilde{\eta}^2}{2\sigma^2}\right) d\tilde{\eta} \qquad (A2.10)$$

Different authors use different version of the error function. The differences are in the exponential term, amplitude and limit. However, they all have the same property. The version used here is defined by equation (A2.11).

$$E_r(x) = erf(x) = \frac{2}{\sqrt{\pi}}\int_0^x e^{-t^2}dt \qquad (A2.11)$$

From (A2.10), let $t = \left(\frac{\tilde{\eta}}{\sigma\sqrt{2}}\right)$ so that $d\tilde{\eta} = \sigma\sqrt{2}dt$

$$\begin{aligned}\int_{-\infty}^{\zeta} p_\zeta(\tilde{\zeta})d\tilde{\zeta} &= \frac{1}{\sqrt{\pi}}\int_{-\infty}^{\frac{\phi(\zeta)}{\sigma\sqrt{2}}} e^{-t^2}dt \\ &= \frac{1}{\sqrt{\pi}}\left[\int_{-\infty}^{0} e^{-t^2}dt + \int_{0}^{\frac{\phi(\zeta)}{\sigma\sqrt{2}}} e^{-t^2}dt\right]\end{aligned} \qquad (A2.12)$$

Multiply the Right-Hand-Side(rhs) by $(\frac{2}{2})$ and change the limit of integration of the first term using

$$\int_{x_1}^{x_2} f(x)dx = -\int_{x_2}^{x_1} f(x)dx \qquad (A2.13)$$

$$= \frac{1}{2}\left[-\frac{2}{\sqrt{\pi}}\int_0^{-\infty} e^{-t^2}dt + \frac{2}{\sqrt{\pi}}\int_0^{\frac{\phi(\zeta)}{\sigma\sqrt{2}}} e^{-t^2}dt\right] \qquad (A2.12cont)$$

Using $E_r(-x) = -E_r(x)$ and $E_r(\infty) = 1$ equation (A2.12) continues

$$= \frac{1}{2}\left[-E_r(-\infty) + E_r\left(\frac{\phi(\zeta)}{\sigma\sqrt{2}}\right)\right] \qquad (A2.12cont)$$

Finally

$$2\int_{-\infty}^{\zeta} p(\zeta)d\zeta = 1 + E_r\left(\frac{\phi(\zeta)}{\sigma\sqrt{2}}\right) \qquad (A2.14)$$

Therefore

$$E_r^{-1}\left(\left[2\int_{-\infty}^{\zeta} p(\zeta)d\zeta - 1\right]\right) = \frac{\phi(\zeta)}{\sigma\sqrt{2}}$$

And

$$\phi(\zeta) = \sigma\sqrt{2}\,\Theta\left(\left[2\int_{-\infty}^{\zeta} p(\zeta)d\zeta - 1\right]\right) = \sigma\sqrt{2}\,\Theta(2F_\zeta(\zeta) - 1) \qquad (A2.15)$$

Where Θ is the inverse error function, E_r^{-1}, and $F_\zeta(\zeta)$ is the cumulative distribution function of equation (A2.10). Figure A2.1 shows the transformation functions $\zeta = \psi(\eta)$ and $\eta = \phi(\zeta)$ for $\sigma = 1$, $\sigma_x = 0.13$, $\mu_3 = 0.5$, and $\mu_4 = 3$. These functions would vary with changing statistics. Interested readers can contact the author for the matlab codes.

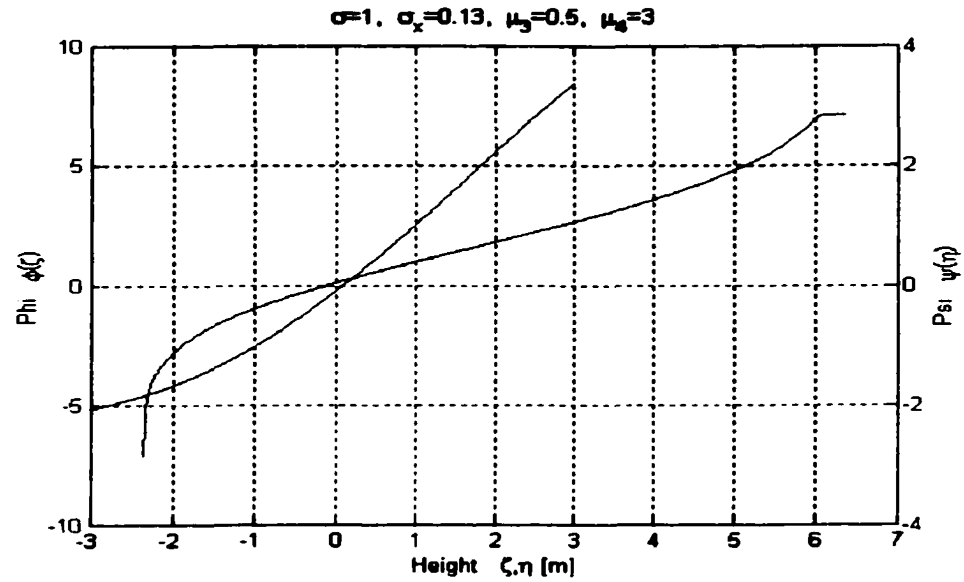

Figure A2.1 The analytical transformtion functions for equations (A2.15) and (5.19), $\sigma = 1$, $\sigma_x = 0.13$, $\mu_3 = 0.5$, and $\mu_4 = 3$.

A3: Attribution

Some of the materials have been taken from other texts to cover developments in the field without quoting. This was done to show a review of previous work and how they correlate with current simulations.

Bibliography

Anctil, F., M. A. Donelan, G. Z. Forristall, K. E. Steele, and Y. Ouellet. (1993), Deep-water field evaluation of the NDBC-SWADE 3-m discus directional buoy. *J. Atmosp. and Oceanic Techn.* 10, 97-112.

Anderson, T.W. (1971), *An Introduction to multivariate statistical analysis*, Second edition, Wiley Series in Probability and Mathematical Statistics, John Wiley and Sons, New York, 1971.

Andrews, C. L. (1998), *Special functions of Mathematics for engineers*, second edition, SPIE Optical Engineering Press., 1998

Aroian, L. L. (1947), Pearson system of probability functions. Van Nostrand's Scientific Encyclopedia. Pg. 1052-1053, D. Van Nostrand Company, Inc. New York.

Bates, C. C. (1949), Utilization of wave forecasting in the invasions of Normandy, Burma, and Japan. *Annals. of the New York Academy of Sciences*, 51, 545-572.

Beckmann, P., A. Spizzichino (1963), *The Scattering of Electromagnetic Waves from Rough Surfaces*, International Series of Monographs on Electromagnetic waves, The MacMillan Company, New York, 1963

Borgman, L. E. (1990), Irregular ocean waves: Kinematics and forces. in *The Sea, 9. Ocean Engineering Science*, Parts A and B; L. LeMehaute and D. M. Hanes, Eds., Wiley, N. Y. 121-168.

Broschat, S. Lynn (1993), "The small slope approximation reflection coefficient for scattering from a 'Pierson-Moskowitz' sea surface", *IEEE Trans. Geos. Remote Sensing*, Vol. 31, No. 5, pp.1112-14, Sept. 93

Buchner, B. (1996), Advances in green water effect prediction for FPSOs. Atlantic Frontier Forum 1996, Aberdeen, Scotland.

Buckley, W. H. (1983), A study of extreme waves and their effects on ship structure. Report SSC-120 DWTNSR and DC, Bethesda, MD. Available from NTIS, 82 pp.

Cardone, V. J., W. J. Pierson, and E. G. Ward (1976), Hindcasting the directional spectra of hurricane-generated waves. *J. Petrol. Techn.* 28, 385-394.

Cooley, J. W. and Tukey, J. W. (1965), An algorithm for the machine computation of the complex Fourier series. *Math. Comp.*, 19, 165-297.

Cooley, J. W. (1987), The re-discovery of the Fast Fourier Transform. *Mikrochimica Acta.* III, 33-45.

Cooley, J. W. (1992), How the FFT gained acceptance. *IEEE Signal Processing Magazine.* 9, 1, 10-13.

Dalzell, J. F. (1974), The "input-output" approach to seakeeping problems- review and prospects. *Seakeeping*, 1953-1973. Technical and Research Symposium S-3. Society of Naval Architects and Marine Engineers. 123- 128.

Dalzell, J. F. (1982), An investigation of the applicability of the third degree functional polynomial model to nonlinear ship motion problems. Davidson Laboratory, SIT DL-82-8-2275.

Dalzell, J. F. (1991), Numerical model of a nonlinear random seaway. Appendix E in *Analysis of Wave Characteristic in Extreme Seas*, SSC 353, Ship Structure Committee, SNAME. (1991).

Donelan, M. A. and W. J. Pierson (1983), The sampling variability of estimates of spectra of wind-generated gravity waves. *J. Geophys. Res.*, 88, C7, 4381-4392.

Donelan, M. A. and W. J. Pierson (1987), Radar-scattering and equilibrium ranges in wind-generated waves - with application to scatterometry. *J. Geophys. Res.*, 92, C5, 4971-5029.

Drennan, W. M. (1988), Accurate calculation on the Stokes water wave. Ph.D. dissertation, University of Waterloo, 169 pp.

Drennan, W. M., Hui, W. H., and Tenti, F. (1992), Accurate calculations of Stokes water waves of large amplitude. *J. Appl. Math. Physics* (ZAMP), 43, 367-384.

Earle, M. D. (1975), Extreme wave conditions during Hurricane Camille. *J. Geophys. Res.* 80. 377-379.

Forristall, G. Z. (1978) On the statistical distribution of wave heights in a storm. *J. Geophys. Res.* 83, C3, 2353-2358.

Gerling, T. W. (1991), "A comparative anatomy of the LEWEX wave system" in *Directional ocean wave spectra*: Johns Hopkins University Press, edited by Robert C. Beal, 1991

Grochowalski, S., C. C. Hsiung, Z. J. Huang and L. Z. Cong (1999), Theoretical modeling of ship motions and capsizing. *Trans. SNAME*, to be published.

Groves, G. W., W. C. Chow (1998), "Glistening-Region model for multipath studies", *Proceedings of SPIE: Targets and Backgrounds*, Vol 3375, pp. 232-243, Aerosense Conf., April 1998.

Hayne, S. G., D. W. Hancock III, and C. L. Purdy (1994), The corrections for significant wave height and attitude effects in the TOPEX radar altimeter.*J. Geophys. Res.* 99, C12. 24941-24955.

Haver, S., O. J. Anderson (2000), Freak Waves: Rare realization of a typical population or typical realizations of a rare population? *ISOPE proceedings*, Tenth conference, May 28-Jun. 2, 123-130

Huang, A. Paul (1996), "Surface slope measurement with a wave follower in TOWARD 84/86", *Office of Naval Research*, Arlington, VA, Report No. ORE 86-3

Hutchison, B. L. (1990), Seakeeping studies: A status report. *Trans. SNAME*, 98, 263-318.

Jean-Pierre, A., W. J. Pierson, G. W. Groves (1999), Stochastic simulation of ocean waves and their effect on microwave scattering. *SPIE proceedings* , Target and Backgrounds: Characterization and Representation V, Vol. 3699, P.138-50, April, 1999

Kinsman, B. (1965), *Wind Waves: Their generation and propagation on the ocean surface.* Printice-Hall, Englewood Cliffs, N. J., 676 pp. (Dover Reprint, 1984).

Kjeldsen, S. P. (1996), "Examples of heavy weather damage caused by giant waves", *Technomarine*, No. 820

Lipa, B. J., D. E. Barrick (1981), Ocean surface height-slope probability density function from SEASAT altimeter echo. *J. Geophys. Res.* 86, C11, 10921-10930

Liu, Y., S. J. Frasier, R. E. McIntosh (1998), "Measurement and classification of low grazing angle radar sea spikes", *IEEE Trans. Antennas Propagat.*, Vol. 46, No. 1 pp. 27-40, Jan. 1998

Long, M. W. (1983), *Radar reflectivity of land and sea*, Artech House Inc., 2nd Ed, 1983

Longuet-Higgins, M. S. (1952) On the statistical distribution of the heights of sea waves. *J. of Marine Research*, 11. 245-266.

Longuet-Higgins, M. S. (1963), The effect of nonlinearities on statistical distributions in the theory of sea waves. *J. Fluid Mech.* 17, 3, 459-480.

Lunde, J. K. (1964), Naval Hydrodynamics (Ship Motions drag reduction), Stanley W. Doroff, pp. 425-435 Sept., 10-12, 1964

Moskowitz, L. (1964), Estimates of the power spectrums for fully developed seas for wind speeds of 20 to 40 knots. *J. Geophys. Res.* 69, 24. 5161-5179.

Neumann, G. and W. J. Pierson (1966), *Principles of Physical Oceanography.* Prentice Hall, Englewood Cliffs, New Jersey.

Ogilvie, T. F. (1964), Recent progress toward understanding and prediction of ship motions. Fifth Symposium on Naval Hydrodynamics, Ship motion and drag reduction. ACR-112 Office of Naval Research, Department of the Navy. Washington, DC. 3-128.

Papoulis, A.(1991), *Probability,Random Variables, and Stochastic Processes*, Third edition, McGraw-Hill series in Electrical Engineering, Communications and signal processing, McGraw-Hill, Inc., New York, 1991.

Pearson, K. (1895) Contributions to the mathematical theory of evolution. II Skew variations in homogeneous material. *Philosophical Transaction of the Royal Society of London, Series A*, 186, 343-414.

Pierson, W. J., L. Moskowitz, (1964), "A proposed spectral form for fully developed wind seas based on the similarity theory of S. A. Kitaigorodskii", *J. Geophys. Res.*, Vol. 69, No. 24, pp. 5181-90, 1964

Pierson, W. J. (1977), Comments on "A parametric wave prediction model". *J. Phys. Oceanogr.* 7, 1. 127-134.

Pierson, W. J. (1993), Oscillatory third-order perturbation solutions for sums of interacting long-crested Stokes waves on deep water. *J. of Ship Research.* 37, 4. 354-383.

Pierson, W. J. (1994), Errata: " Oscillatory third-order perturbation solutions for sums of interacting long-crested Stokes waves on deep water". *J. of Ship Research.* 38, 2. 136.

Pierson, W. J. (1994), Comments on the paper by Teng, et al. (1994). *Trans. SNAME,* 102, 495-497.

Pierson, W. J., Dalzell, J. F., Tick, L. J. and Wallendorf, L. (1998), Wave tank studies of nonlinear gravity waves: Comparisons with a model for sums of interacting long crested Stokes waves on deep water. *Society of Naval Architects and Marine Engineers,* Technical and Research Report R-52.

Pierson, W. J., A. Jean-Pierre (1999), "Monte Carlo simulations of nonlinear ocean wave records with implications for models of breaking waves", *J. Ship Research,* Vol. 43, No. 2, pp. 121-134, June 1999

Plant, W. J. (1990), "Bragg scattering of electromagnetic waves from air/sea interface", in *Surface waves and Fluxes,* G. L. Geernaert and W. J. Plant, Eds. Norwell, MA: Kluwer, Vol II, 1990

Quartly, G. D., M. A. Srokosz (2001), Analysing altimeter artifacts: statistical properties of ocean waveforms. *J. atmos. Ocean. Tech.,* 18, No.12, 2074-2091

Rodriguez, E., (1988), Altimetry for Non-Gaussian Oceans: Height Biases and Estimation of parameters. *J. Geophys. Res.* 93, C11, 14107-14120

Rodriguez, E. and J. M. Martin (1994), Assessment of the TOPEX altimeter performance using waveform retracking. *J. Geophys. Res,* 99, C12. 24957-24969.

Rodriguez, E., B. Chapman (1989), Extracting ocean surface information from altimeter returns: The deconvolution method. *J. Geophys. Res.,* 94, C7, 9761-9778

Sand, S. E., N. E. Ottesen-Hassen,P. Klinting, O. T. Gudmestad and M. J. Sterndorf (1990), *Freak waves,* In *Water wave kinematics* , Ed. A. Torum and O. T. Gudmestad, Kluwer Academic Publishers, Dordrecht, the Netherlands.

Srokosz, M. A. (1998), A new statistical distribution for the surface elevation of weakly nonlinear water waves.*J. of Physical Oceanography.* Notes and Correspondence. 149-155, Jan. 1998

St Denis, M. and W. J. Pierson (1953), On the motions of ships in confused seas. *Trans. SNAME,* 61, 280-357.

Steele, K. E., Teng C. C., and Wang D. W. C. (1992), Wave direction measurements using pitch-roll buoys. *Ocean Eng.* Pergamon Press Ltd. 19, 4, 349-375.

Sverdrup, H. U., M. W. Johnson, and R. C. Fleming (1942), *The Oceans.* Prentice Hall, New York, 1087 pp.

Sverdrup, H. U. (1943), *Oceanography for Meteorologists.* Prentice Hall, Inc. New York, 235 pp.